Università degli studi di Milano-Bicocca

DIPARTIMENTO DI FISICA "G. OCCHIALINI"

CORSO DI DOTTORATO IN FISICA E ASTRONOMIA
CICLO XXVII

Superconducting microwave microresonators for neutrino physics

Settore Scientifico Disciplinare FIS/01

Author:
Marco Faverzani

Supervisor:
Prof. Angelo Nucciotti

Anno Accademico 2014-2015

UNIVERSITÀ DEGLI STUDI DI MILANO-BICOCCA

Abstract

Dipartimento di fisica "G. Occhialini"

Philosophiæ Doctor

Superconducting microwave microresonators for neutrino physics

by Marco Faverzani

The determination of the neutrino mass is still an open issue in particle physics and astrophysics. The neutrino oscillation experiments have shown that at least three massive neutrinos exist, but their absolute mass remains undetermined: through the observation of flavor oscillation it is possible to determine only the difference between the squares of the neutrino mass eigenvalues.

Among the possible experimental approaches that can access the value of the neutrino mass, the only theory-unrelated consists in the kinematic measurement of the products of a single beta decay. To date, the study of the beta decay of ^{3}H using electrostatic spectrometers has been the most sensitive approach. Calorimetry provides an alternative to spectroscopy: in this case the beta emitter is embedded in the detector, avoiding both the issues of an external source and the systematic uncertainties coming from the excited final states. The calorimetric measurement of the energy released in a nuclear beta decay allows to measure the whole energy, except the fraction carried away by the neutrino: due to the energy conservation, a finite neutrino mass m_ν causes the energy spectrum to be truncated at $Q - m_\nu$, where Q is the transition energy of the decay. The Electron Capture (EC) of ^{163}Ho ($Q \sim 2.5$ keV) is an ideal decay, thanks to the high fraction of events close to the end-point (i.e. the maximum energy of the relaxation energy spectrum). In order to achieve enough statistics for a calorimetric experiment to be competitive with spectrometers, a large number of detectors (order of 10^4) is required. Superconducting microwave microresonators are detectors suitable for large-scale multiplexed frequency domain readout, with theoretical energy and time resolution at the keV energy scale of $\sim$ eV and $\sim$ μs, respectively. The detectors based on superconducting microresonators are currently being pursued for bolometric measurements of sub-millimeter/far-infrared and near-infrared/visible wavelengths. The aim of my work is to adapt the existing technology of the superconducting microwave microresonators to develop arrays of single-particle detectors applicable to the calorimetric measurement of the energy spectrum of ^{163}Ho. During my PhD work I took care of the installation

of the first facility in Milano-Bicocca University capable to test this kind of detectors. I have dealt with the first installation and comprehension of the entire microwave setup required to read-out the detectors. In particular I worked to instrument a ^{3}He/^{4}He dilution refrigerator of the cryogenic laboratory of Milano-Bicocca University with the needed RF instrumentation: a cold High Electron Mobility Transistor microwave amplifier was anchored on the 4 K flange, and the semi-rigid coaxial cables were installed, choosing a superconducting Nb coaxial cable for the output line. The setup that I assembled was demonstrated to be able to read two channels in parallel, acquiring signals in coincidence on two different resonators. I also developed a dedicated software package capable to acquire and analyze the output coming from the homodyne setup used for the readout, converting it to the physical quantities of interest. Finally, using these instruments, I characterized different detectors, collecting data useful for selecting the optimal design and material.

The materials considered consisted of titanium nitride (TiN) with different stoichiometric ratios. The nitrides, especially TiN, possess promising qualities that could significantly improve the sensitivity for most applications of microresonator detectors. In order to further improve the signal to noise ratio, superconducting detectors with T_c ranging between $\sim$ 0.5 K and 2 K were produced and tested. The reduced T_c was obtained by superimposing thin layers of stoichiometric TiN to pure Ti layers, and the T_c was tuned by varying the ratio between the thickness of the layers.

After testing a first design with two low energy X-ray sources, it was found that despite the quality factors were high enough to achieve a good expected sensitivity, the energy spectrum did not feature any structure attributable to a monochromatic energy source. The incapability to resolve monochromatic energies was attributed to an exchange of phonons between the superconductor and the substrate it leans on: given the small thickness of the superconductor ($\sim$ 200 nm at most), the majority of events takes place in the substrate, giving rise to a population of high energy phonons that could reach the detector in a quantity that depends on the position of the interaction, causing a position-dependent energy response. In order to overcome this issue new geometries were designed, produced and finally tested. In particular, in order to prevent exchange of phonons between the superconductor and the substrate, the substrate below the sensitive part of the detector was etched away, leaving an empty gap in its place. The measurements still proved that a big fraction of events is affected by a non complete collection of energy.

I fully characterized all the devices in static conditions, measuring the critical temperature, the gap parameter, the quality factors and the fraction of the kinetic inductance for every geometry and material considered. The noise limit was measured as well, individuating the limiting contribution, set by the noise of the cold amplifier. From the tests made with the X-ray source it was also possible to measure another important parameter

that affects the sensitivity of a pair breaking detector: the quasi-particle recombination time.

Contents

Abbreviations

IDC	**I**nter**D**igitated **C**apacitors
CPW	**Co**Planar **W**aveguide
CPS	**Co**Planar **S**tripline
HEMT	**H**igh **E**lectron **M**obility **T**ransistor
LEKID	**L**umped **E**lement **K**inetic **I**nductance **D**etector
SM	**S**tandard **Model**
NH	**N**ormal **H**ierarchy
IH	**I**nverted **H**ierarchy
$0\nu\beta\beta$	Neutrinoless double beta decay
C.L.	**C**onfidence **L**evel
EC	**E**lectron **C**apture
IBEC	**Internal B**remsstrahlung in **E**lectron **C**apture
LTD	**L**ow **T**emperature **D**etector
MKID	**M**icrowave **K**inetic **I**nductance **D**etector
TES	**T**ransition **E**dge **S**ensors
SQUID	**S**uperconducting **Q**uantum **I**Interference **D**evice
MMC	**M**etallic **M**agnetic **C**alorimeters
STJ	**S**uperconducting **T**unnel **J**unction
DC	**D**irect **C**urrent
AC	**A**lternating **C**urrent

Chapter 1

Neutrino physics

The pathway towards a Grand Unified Theory (GUT) registered a great boost through the unification of the electromagnetic and weak forces into a single electro-weak model, formulated for the first time by Glashow [1], Weinberg [2] and Salam [3] in the '60s. Such theory relies on a locally invariant lagrangian under the action of the $SU(2)_L \bigotimes U(1)$ gauge group. Adding the invariance under the action of the SU(3) group, the Standard Model (SM) of elementary particles is then complete. The SM achieved marvelous successes over the last decades, culminating with the observation of the Higgs boson at LHC [4, 5]. Nevertheless, through the years the model was challenged by experimental evidences not foreseen by the model, opening the way to new physics beyond the SM.
One of the still open questions in nowadays particle physics concerns the neutrino, and in particular its mass. Contrarily from how postulated in the SM, in fact, through the flavor oscillation phenomenon, neutrinos have shown to be a massive particle. The experiments aimed to the observation of such effect, though, are not able to measure the absolute value of the neutrino mass, but they can only measure the difference in squared mass Δm^2_{ij} between the different mass eigenstates of this particle. In order to measure the absolute neutrino mass, three main approaches can be adopted: a) high precision measurements of the kinematic of a low energy nuclear decay involving the production of a neutrino, which give the value of the effective electron neutrino mass m_β; b) searches for the neutrinoless double beta decay ($0\nu\beta\beta$), that provide the electron Majorana mass $m_{\beta\beta}$; c) cosmological researches, yielding the sum of the masses $\Sigma_i m_i$.

1.1 The massive neutrino

Among all the particles constituting the elementary particles "zoo" of the SM, neutrino has a uncommon story, it was in fact theoretically postulated before it was discovered. It was Pauli in 1930, with the aim of assuring the conservation of the four-momentum in the beta decay, to introduce a particle that he called "neutron", which was then renamed into *neutrino* few years later by E. Fermi, while formulating his theory of beta decay [6]. It took more than 20 years to experimentally detect neutrinos for the first time: it was in 1956 that F. Reines and C. Cowan [7, 8] observed the inverse beta decay caused by neutrino interactions.

With the final formalization of the SM in the '70s, the neutrino is described as a zero-charge, massless and left-handed weakly-interacting lepton. This unique set of features makes it a very interesting particle: been able to interact only via weak interactions[1], it can pass through the interstellar medium present in the universe preserving information about its original direction and energy. This particle is therefore the ideal career to give us a record of the structure of the cosmos and its evolution. On the other hand, this very same quality makes it one of the hardest particle to detect and measure, for which reason neutrino is a particle that still presents many unknown aspects.

1.1.1 Flavor oscillation

The first evidence that neutrinos are massive particles came from the observation of the flavor oscillation phenomenon. Taking inspiration from the mixing mechanism of quarks, which interact as linear combination of their mass eigenstates weighted by the CKM (Cabibbo-Kobayachi-Maskawa) matrix elements, Pontecorvo introduced the idea of flavor oscillation of neutrinos. In case of non-vanishing mass, in fact, it is possible to think a flavor eigenstate ($|\nu_\alpha\rangle$) as a coherent superimposition of mass eigenstates ($|\nu_i\rangle$) [9]:

$$|\nu_\alpha\rangle = \sum_i U_{\alpha i}|\nu_i\rangle \tag{1.1}$$

Inverting the relation, the expression for the (stationary) mass eigenstate is:

$$|\nu_i\rangle = \sum_\alpha \left(U^\dagger\right)_{i\alpha}|\nu_\alpha\rangle = \sum_\alpha U^*_{\alpha i}|\nu_\alpha\rangle \tag{1.2}$$

[1] and gravitationally

which evolves in time as[2]:

$$|\nu_i\left(x,t\right)\rangle = \mathrm{e}^{-iE_it}|\nu_i\left(x,0\right)\rangle = \mathrm{e}^{-iE_it}\mathrm{e}^{ipx}|\nu_i\rangle \tag{1.3}$$

Under the assumption that neutrinos are emitted at $(x,t) = (0,0)$, and that $p \gg m_i$, one can find the probability of finding the original flavor:

$$P\left(\alpha \to \alpha\right) = 1 - \sum_{\alpha \neq \beta} P\left(\alpha \to \beta\right) \tag{1.4}$$

where:

$$\begin{aligned} P\left(\alpha \to \beta\right) = \delta_{\alpha\beta} & \\ & - 4Re \sum_{i>j=1}^{3} \left(U_{\alpha i}U^*_{\alpha j}U^*_{\beta i}U_{\beta j}\right) sin^2\left(\Delta m^2_{ij}\frac{L}{4E}\right) \\ & + 4Im \sum_{i>j=1}^{3} \left(U_{\alpha i}U^*_{\alpha j}U^*_{\beta i}U_{\beta j}\right) sin^2\left(\Delta m^2_{ij}\frac{L}{4E}\right) \end{aligned} \tag{1.5}$$

and $\Delta m^2_{ij} = m^2_i - m^2_j$.

As it is possible to see from (1.5), the transition among different flavors is allowed only if at least one of the neutrino mass eigenstates has finite mass and if there are non diagonal terms in the matrix U. An experiment aimed at the measurement of the oscillation parameters, though, will only be sensitive to Δm^2_{ij} and not to the absolute neutrino mass value.

Similarly to the U_{CKM} matrix, the U_{PMNS}[3] matrix, in the case of 3 flavor neutrinos, can be parametrized by three angles, Θ_{12}, Θ_{13}, Θ_{23} and by a CP-violation phase, δ. If neutrino is a Majorana particle, two extra phases will be added. Using the Chau and Keung parametrization, the matrix becomes[4] [10]:

$$\begin{pmatrix} \nu_e \\ \nu_\mu \\ \nu_\tau \end{pmatrix} = \begin{pmatrix} c_{12}c_{13} & s_{12}c_{13} & s_{13}\mathrm{e}^{-i\delta} \\ -s_{12}c_{23} - c_{12}s_{23}s_{13}\mathrm{e}^{i\delta} & c_{12}c_{23} - s_{12}s_{23}s_{13}\mathrm{e}^{i\delta} & s_{23}c_{13} \\ s_{12}s_{23} - c_{12}c_{23}s_{13}\mathrm{e}^{i\delta} & -c_{12}s_{23} - s_{12}c_{23}s_{13}\mathrm{e}^{i\delta} & c_{23}c_{13} \end{pmatrix} \begin{pmatrix} \nu_1\mathrm{e}^{i\alpha_1/2} \\ \nu_2\mathrm{e}^{i\alpha_2/2} \\ \nu_3 \end{pmatrix}$$

In order to fully comprehend neutrinos and their interactions, it's necessary to know all their masses and all the parameters of the mixing matrix.

[2] $c = \hbar = 1$

[3] PMNS: Pontecorvo-Maki-Nakagava-Sakata

[4] $c_{ij} \equiv cos(\Theta_{ij})$ e $s_{ij} \equiv sin(\Theta_{ij})$

In the three flavors scenario, only two neutrino mass squared differences are independent: Δm^2_{21} and Δm^2_{31}. For convenience Δm^2_{21} is set to be the smaller of the two and the neutrino will be numbered in such a way that $m_1 < m_2$, so that Δm^2_{21} turns out to be a positive quantity. The angles Θ_{12} and Θ_{23} and the mass squared differences Δm^2_{21} and Δm^2_{32} are determined by the oscillation experiments of solar (ν_e) and atmospheric neutrinos (ν_μ and $\overline{\nu}_\mu$), respectively. The latest data from neutrino experiments (tab. 1.1 [11], fig. 1.1) do not allow to determine the sign of Δm^2_{31}, thus two *hierarchies* are possible (fig. 1.2): *normal hierarchy (NH)* ($m_1 < m_2 \ll m_3$) and *inverted hierarchy (IH)* ($m_3 \ll m_1 < m_2$). The situation where $m_1 \sim m_2 \sim m_3$ is called degenerate pattern.

Parameter	**Central value**	**1σrange**	**2σrange**
$\Delta m^2_{21}/10^{-5}\text{eV}^2$ (NH or IH)	7.54	7.32 – 7.80	7.15 – 8.00
$\Delta m^2/10^{-3}\text{eV}^2$ (NH)	2.43	2.37 – 2.49	2.30 – 2.55
$\Delta m^2/10^{-3}\text{eV}^2$ (IH)	2.38	2.32 – 2.44	2.25 – 2.50
$\sin^2\Theta_{12}/10^{-1}$ (NH or IH)	3.08	2.91 – 3.25	2.75 – 3.42
$\sin^2\Theta_{13}/10^{-2}$ (NH)	2.34	2.15 – 2.54	1.95 – 2.74
$\sin^2\Theta_{13}/10^{-2}$ (IH)	2.40	2.18 – 2.59	1.98 – 2.79
$\sin^2\Theta_{23}/10^{-1}$ (NH)	4.37	4.14 – 4.70	3.93 – 5.52
$\sin^2\Theta_{23}/10^{-1}$ (IH)	4.55	4.24 – 5.94	4.00 – 6.20
δ/π (NH)	1.39	1.12 – 1.77	0.00 – 0.16$\oplus$0.86 – 2.00
δ/π (IH)	1.31	0.98 – 1.60	0.00 – 0.02$\oplus$0.70 – 2.00

TABLE 1.1: Latest oscillation parameters. Δm^2 is defined as $m^2_3 - (m^2_1 + m^2_2)/2$, it assumes positive values for NH and negative for IH.

The absolute scale mass and the two Majorana phases are quantities not accessible in the oscillation experiments. The measurement of such quantities is the main goal of non-oscillation experiments, like neutrinoless double beta decay and single beta decay experiments.

1.1.1.1 Hierarchy experiments

The measurement of the neutrino mixing angle Θ_{13} has allowed to design next generation experiments aimed to the measure of the neutrino mass hierarchy and to the leptonic CP-violating phase. The next generation of oscillation experiments will determine the mass hierarchy of the neutrino masses from the disappearance of reactor electron antineutrinos.

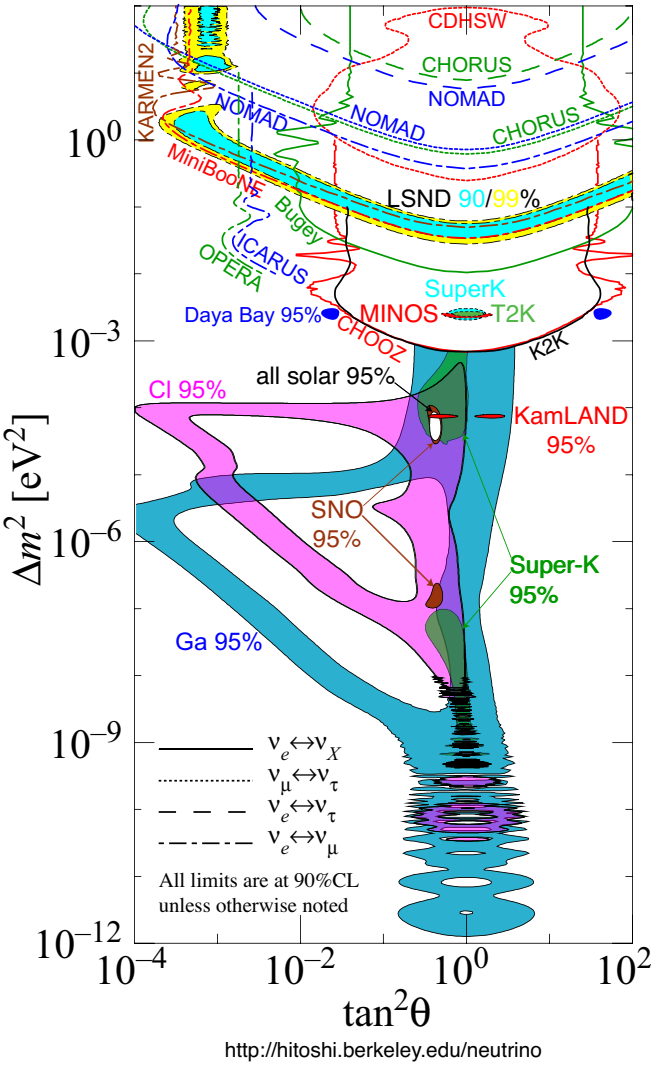

FIGURE 1.1: Most recent neutrino oscillation parameters.

The Jiangmen Underground Neutrino Observatory (JUNO) is a proposed intermediate baseline experiment that aims to determine the mass hierarchy by precisely measuring the energy spectrum of the reactor electron antineutrinos at a distance of ∼53 km from the reactors of ∼36 GW total thermal power with a 20 kton liquid scintillator detector with an energy resolution of $3\%/\sqrt{E(\mathrm{MeV})}$ [12]. JUNO is expected to reach a sensitivity of $\chi^2 > 16$. A similar experiment, RENO-50, was proposed in South Korea. It will employ 18 ktons of ultra-low-radioactivity liquid scintillator with 15 thousand 20" PMTs placed at 50 km away from the Hanbit nuclear power plant [13]. Both of these experiments are expected to start the data taking by the 2020.

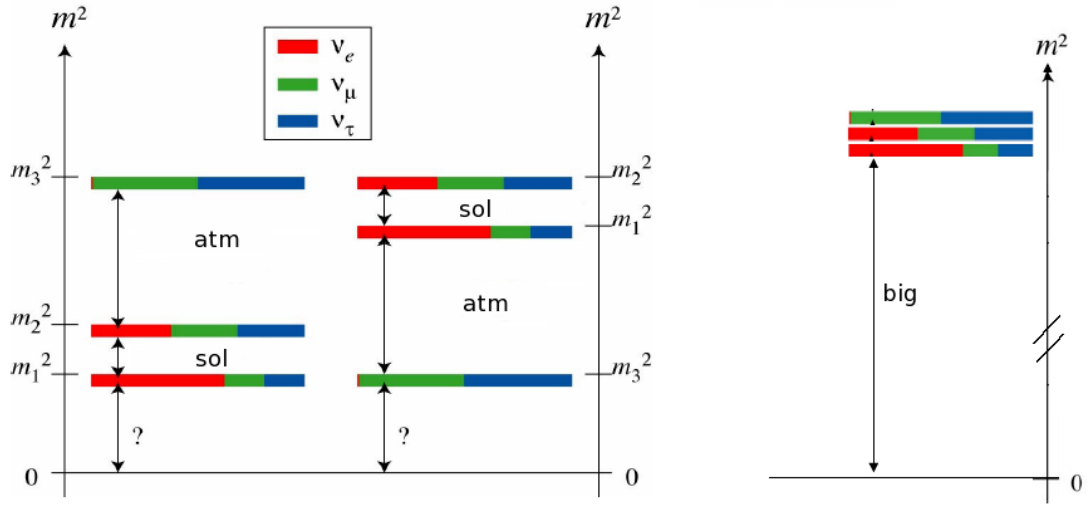

FIGURE 1.2: The neutrino mass hierarchies. Colors indicate flavor abundance in each mass eigenstate.

1.2 Non oscillation experiments

As seen in sec. 1.1, the evidence of oscillation among different flavors gave the proof of a non-vanishing neutrino mass, but the experiments aimed at the observation of such effect are not able to measure the absolute mass of this particle, neither they can establish if the neutrino is a Majorana particle or not. In the following a brief overview of the techniques that can fulfill to this requirements will be presented.

1.2.1 Cosmological observations

Neutrinos, like any other existing particle, give a contribution to the total energy density of the Universe. Light neutrinos remain relativistic through most of the evolution of the Universe and, as consequence, they play a major role in the formation of large scale structures leaving a clear signature in many cosmological observables. The main effect of neutrinos in cosmology is to suppress the growth of fluctuations on scales below the horizon when they become non-relativistic. Because of this suppression it is possible to infer constraints, although indirectly, on the neutrino masses by comparing the most recent cosmological data with the current theoretical predictions. In fact the neutrino energy density ($\Omega_\nu h^2$) is related to the sum of the neutrino masses through the following

expression:

$$\Omega_\nu h^2 = \sum_i m_i / \left(94eV^2\right) \tag{1.6}$$

where h is the normalized Hubble constant. Depending on the set of data considered, the limits on the neutrino masses range from few eV to few hundreds of meV. The final WMAP 9-year dataset obtains an upper bound on the sum of neutrino masses of 1.3 eV at 95% C.L. [14] within the standard cosmological model, ΛCDM. Planck data alone constrain $\sum_i m_i$ to 0.72 eV at 95% C.L. [15]. This result should be considered as the most conservative and reliable cosmological constraint on neutrino masses. A tighter bound on the neutrino masses can be obtained by combining CMB observations with measurements of the Hubble constant H_0 and cosmic distances such as from Type Ia supernovae and Baryon Acoustic Oscillations (BAO). The PlankTT+lensing+polarization+H_0 analysis of [15] reports a constraint of 0.23 eV at 95% C.L.. Current cosmological data probe the region of neutrino masses where the three neutrino states are degenerate. In conclusion, the cosmological observations can lead to results complementary to laboratory experiments, such as single beta decay and neutrinoless double beta decay, but they are heavily affected by uncertainties related to the theory model.

1.2.2 Double beta decay

The two-neutrino double beta decay ($2\nu\beta\beta$) was firstly proposed in 1935 by Maria Goeppert-Mayer [16]. It consists in a second order process of the single beta decay and it is therefore allowed by the SM. The first direct observation dates back to 1987 [17], and it is observed now in more than ten nuclei [18, 19].

The neutrinoless double beta decay, if exists, is an extremely rare process. In such a process a virtual neutrino works as a mediator between the vertices of two beta decays (fig. 1.3). Given the V-A nature of weak interactions, this process would require the coupling of a right-handed anti-neutrino in one vertex and of a left-handed neutrino in the other one. This is possible only if the neutrino chirality is not a good quantum number (i.e. if neutrino is massive) and if neutrino and anti-neutrino are in fact the very same particle; this would mean that neutrino is a Majorana particle. This decay would violate the conservation of the lepton number by two units, so it is not allowed within the SM theory. Besides, given the very small value of the neutrino mass, the phase space related to the process would strongly suppress the probability of the decay, making it

one of the most rare process that could occur in nature. The lifetime of the neutrinoless double beta decay is expected to be longer than 10^{25} years. The current best limit on the half life value is set by the GERDA experiment [20] to $T^{0\nu}_{1/2} > 2.1 \times 10^{25}$ yr (90% C.L.).

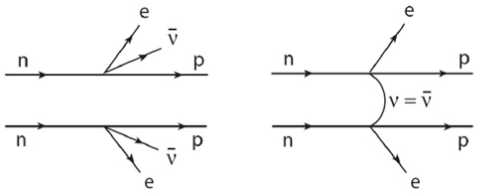

FIGURE 1.3: Feynman diagram of $2\nu\beta\beta$ and $0\nu\beta\beta$. In latter case, a virtual neutrino is exchanged between the vertices of the two beta decays, violating the conservation of the lepton number.

The experiments aimed at the observation of $0\nu\beta\beta$ measure the half life of the isotope under study; this quantity is related to the neutrino mass through the following formula:

$$\left(T^{0\nu}_{1/2}\right)^{-1} = \frac{|m_{\beta\beta}|^2}{m_e^2} G^{0\nu} \left|M^{0\nu}\right|^2 \tag{1.7}$$

where m_e is the electron mass, $G^{0\nu}$ is the phase space factor, $M^{0\nu}$ is the nuclear matrix element and $m_{\beta\beta}$ is the effective Majorana mass, given by a coherent sum over the contributions of the different mass eigenstate to the electron flavor:

$$m_{\beta\beta} = \left|\sum_i U_{ei}^2 m_i\right| = \left|\sum_i |U_{ei}|^2 \, e^{i\alpha_i} m_i\right| \tag{1.8}$$

where U_{ei} are elements of the PMNS matrix corresponding to the electron flavor and α_i are the Majorana phases. Given the results on the matrix elements and the squared mass difference obtained from the oscillation experiments, it is possible to express the $m_{\beta\beta}$ in terms of only three parameters: the mass of the lightest neutrino and the two Majorana phases (fig. 1.4). In order to obtain an accurate value of the $m_{\beta\beta}$, all the parameters present in 1.8 must be well known. While the phase space can be precisely calculated, the nuclear matrix element have uncertainty due to unknown details of the nuclear part of the process, so it results to be strongly dependent on the nuclear model used for its evaluation [21–25].

The most recent limits on $m_{\beta\beta}$ are reported in table 1.2.

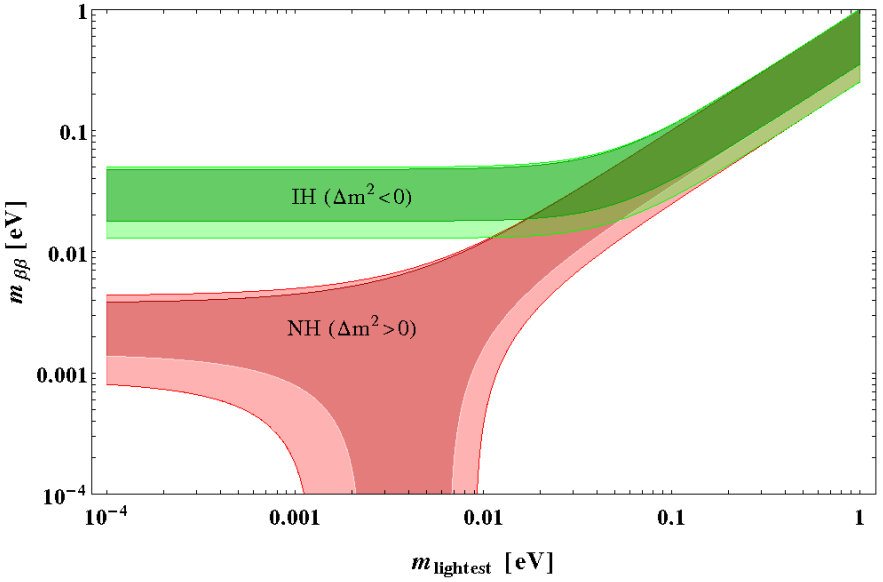

FIGURE 1.4: Predictions on $m_{\beta\beta}$ as a function of the lightest neutrino mass in the cases of NI and IH. The shaded area correspond to the 3σ interval [26].

$m_{\beta\beta}$ (eV)	Isotope	% C.L.	Experiment
<0.42 - 0.66	^{76}Ge	90	Heildeberg-Moscow [27]
<0.33 - 1.35	^{76}Ge	90	IGEX [28]
<0.2 - 0.4	^{76}Ge	90	GERDA [20]
<0.94 - 2.5	^{82}Se	90	NEMO-3 [29]
<0.3 - 0.9	^{100}Mo	90	NEMO-3 [30]
<0.27 - 0.76	^{130}Te	90	CUORE-0 [31]
<0.14 - 0.28	^{136}Xe	90	KamLAND-Zen [32]
<0.19 - 0.45	^{136}Xe	90	EXO [33]
<1.1 - 2.7	^{136}Xe	90	DAMA [34]

TABLE 1.2: Most recent limits on the effective Majorana mass.

1.2.3 Single beta decay

As seem from the previous sections, both the cosmological observations and the $0\nu\beta\beta$ are capable to give information regarding the neutrino mass with high sensitivity, but both are affected by uncertainties due to the theoretical model of the system they are investigating. The most theory-unrelated method of measuring the neutrino mass is based on the kinematic analysis of electrons emitted in single β-decay. According to the energy-momentum conservation, in fact, the single β-decay experiments look for a tiny deformation of the spectrum close to the end-point E_0, which is due to a finite mass of

the neutrino. From such measurements the (anti)neutrino mass is measured:

$$m_{\nu_e} = \sqrt{\sum_{i=1}^{3} |U_{ei}|^2 \, m_i^2} \tag{1.9}$$

The sum is over all the mass eigenstates because it is not possible to resolve them experimentally. Even so, by setting a limit on ν_e, a limit on the lightest mass eigenstate is also given. When the oscillations experiments will provide the values and the signs of all neutrino mass squared differences Δm_{ij}^2 and the mixing parameters $|U_{ei}|^2$ then, once measured the value of m_{ν_e}, the neutrino mass squared (m_j^2) can be determined:

$$m_j^2 = m_{\nu_e}^2 - \sum_i |U_{ei}|^2 \, \Delta m_{ij}^2 \tag{1.10}$$

On the other hand, if only the absolute values of $\left|\Delta m_{ij}^2\right|$ are accessible, a limit on m_{ν_e} from beta decay experiments could be used to give an upper limit on the maximum value m_{max} of m_i:

$$m_{max}^2 \leq m_{\nu_e}^2 + \sum_{i<j} \left|\Delta m_{ij}^2\right| \tag{1.11}$$

In table 1.3 the current limits established by single beta decay experiments are reported, while the figure 1.5 plots the allowed value of m_β versus the lightest neutrino mass.

m_β (eV)	C.L. %	Isotope	Technique	Experiment
<15	90	^{187}Re	Calorimeter	Mibeta [35]
<2.05	95	^{3}H	Spectrometer	Troitsk [36]
<2.3	95	^{3}H	Spectrometer	Mainz [37]

TABLE 1.3: Current limits on the electron neutrino mass.

1.3 Direct mass measurement

As already mentioned, the most theory-unrelated method of accessing the neutrino mass is through the kinematic measurement of the electron emitted in a single beta decay. At the present time the most stringent limits are given by two spectrometric experiments,

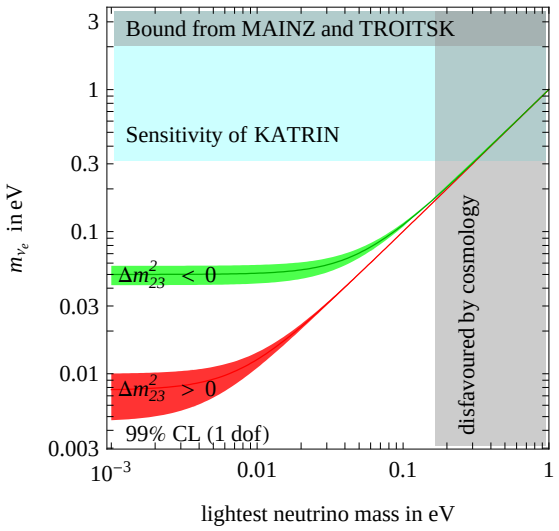

FIGURE 1.5: Allowed values of m_β as a function of the lightest neutrino mass in both NH and IH cases. The gray areas display the current limits given by single beta decay and cosmology experiments [38].

which set the m_ν to be smaller than 2.1 eV (see tab. 1.3).

The β-decay is a nuclear process that involves two isobar nuclides with the emission of an electron and an anti-neutrino:

$$(A, Z-1) \rightarrow (A, Z) + e^- + \overline{\nu}_e \tag{1.12}$$

From this reaction what is actually measured is the anti-neutrino mass, which, in virtue of the CPT theorem, is equal to the neutrino mass. The total energy Q released within such a process is given by:

$$Q = M(A, Z-1)c^2 - M(A, Z)c^2 \tag{1.13}$$

where M indicates the total mass of the atom.

By neglecting the recoil of the nucleus, and calling E_0 the maximum kinetic energy available to the electron, the energy distribution of the electrons emitted is described by:

$$N_\beta = p_\beta \left(E_\beta + m_e c^2\right) \left(E_0 - E_\beta\right) \sqrt{\left(E_0 - E_\beta\right)^2 - m^2_{\nu_e} c^4} F\left(Z, E_\beta\right) S\left(E_\beta\right) \left[1 + \delta_R\left(Z, E_\beta\right)\right] \tag{1.14}$$

where p_β and E_β are the momentum and the energy of the electron, respectively. In the equation (1.14) the following parameters are present:

- $p_\beta \left(E_\beta + m_e c^2\right) (E_0 - E_\beta) \sqrt{(E_0 - E_\beta)^2 - m_{\nu_e}^2 c^4}$ is the phase-space of a three-body decay.

- $F(Z, E_\beta)$ is a Coulomb correction (Fermi function), which takes into account for the effects due to the charge of the nucleus on the wave function of the emitted electron. Considering the relativistic effects and a finite dimension of the nucleus it becomes:

$$F(Z, E_\beta) = 4 \left(\frac{2 p_e R}{\hbar}\right)^{2\gamma - 2} \mathrm{e}^{\pi\eta} \left|\frac{\Gamma(\gamma + i\eta)}{\Gamma(2\gamma + 1)}\right|^2 \approx \frac{2\pi\eta}{\mathrm{e}^{-2\pi\eta}} \tag{1.15}$$

  where $\eta = \alpha Z E_\beta 7 p_e$, $\gamma = \left(1 - (\alpha Z)^2\right)^{1/2}$, R is the nuclear radius ($R = 1.2 A^{1/3} fm$) and α is the fine structure constant. The expression (1.15) is obtained as solution of the Dirac equation with point-like nucleus, computed at a distance R from the nucleus. By considering the shielding effect of the (Z-1) electrons of the parent nucleus, this term gets a further correction term, becoming:

$$F(Z, E_\beta)' = F(Z, E_\beta - \langle V_\beta \rangle) \frac{E_\beta - \langle V_\beta \rangle}{E_\beta} \tag{1.16}$$

  where $\langle V_\beta \rangle$ is the average potential experimented by the electron at the nuclear surface due to the atomic electrons. In the Thomas-Fermi model it is: $\langle V_\beta \rangle = 1.45 m_e \alpha^2 Z^{4/3}$.

- $S(E_\beta)$ is the form factor of the beta spectrum which takes into account the nuclear matrix element $M(E_\beta)$ of the electro-weak interaction. In can be expressed as:

$$S(E_\beta) = G_F^2 \left(\frac{m_e^5 c^4}{2\pi^3 \hbar^7}\right) cos^2 \Theta_C \left|M(E_\beta)\right|^\epsilon \tag{1.17}$$

  where G_F is the Fermi coupling constant and Θ_C is the Cabibbo angle.

- δ_R, finally, is the electromagnetic radiative correction, which can be neglected due to the smallness of this value.

Sometimes it can be convenient to express the beta spectrum in the form of the *Kurie plot*, where the variable $K(E_\beta)$ is plotted as a function of the energy of the electron E_β:

$$K(E_\beta) = \sqrt{\frac{N_\beta(Z, E_\beta, m_{\nu_e})}{p_\beta E_\beta F(Z, E_\beta) S(E_\beta) [1 + \delta_R(Z, E_\beta)]}} = (E_0 - E_\beta) \left(1 - \frac{m_{\nu_e}^2 c^4}{(E_0 - E_\beta)^2}\right)^{1/4} \tag{1.18}$$

In the ideal case of infinite energy resolution, one can observe that the *Kurie plot* is a straight line that, whit $m_\nu = 0$, intersects the energy axis at the total transition energy, while in case of $m_\nu \neq 0$ a distortion from the linearity is observable near the end-point, due to a lack of energy equal to the value of the neutrino mass (fig. 1.6). It is clear

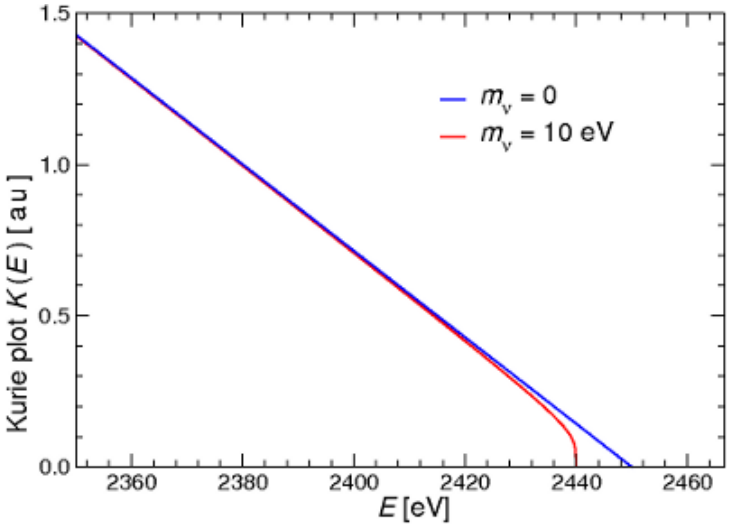

FIGURE 1.6: *Kurie plot* in the case $m_\nu = 0$ (blue line) and $m_\nu = 5$eV (red line).

from this plot that the most interesting part of the spectrum is the one closest to the end-point, where the sensitivity is higher. On the other hand, this is also the region characterized by the lowest counting rate. Considering an energy interval $\Delta E \approx 3 m_{\nu_e}$, the fraction of events that occurs is:

$$F_{\Delta E}(E) = \int_{E_0 - \Delta E}^{E_0} N_\beta(Z, E_\beta, m_{\nu_e} = 0) dE \approx 2 A_\beta \left(\frac{\Delta E}{E_0}\right)^3 \tag{1.19}$$

Besides the low statistics, there are other important factors to consider that contribute to hide the effect of non vanishing mass. For instance, no real detector exploits infinite energy resolution: for this reason the detector response function has to be well known. Furthermore, the daughter atom might be left in an excite state and the exciting energy could be released after the response time of the detector, distorting in this way the shape

of the spectrum. This effect makes the measured spectrum a sum of several spectra with different transition energy:

$$N_\beta(Z, E_\beta, m_{\nu_e}) \approx \sum_i w_i p_\beta E_\beta \left(E_0 - E_\beta - V_i\right)^2 \left(1 - \frac{m_{\nu_e}^2 c^4}{(E_0 - E_\beta - V_i)^2}\right) F\left(Z, E_\beta\right) S\left(E_\beta\right) \tag{1.20}$$

where w_i and V_i are the probabilities and the energies of transition of the i-th final level. This effect is particularly misleading in measuring the neutrino mass: it becomes evident by assuming $m_{\nu_e} = 0$ and summing over all the final states:

$$N_\beta\left(Z, E_\beta, 0\right) \approx p_\beta E_\beta \left(E_0 - E_\beta - \langle V_i \rangle\right)^2 \left(1 + \frac{\langle V_i^2 \rangle - \langle V_i \rangle^2}{\left(E_0 - E_\beta - \langle V_i \rangle\right)^2}\right) F\left(Z, E_\beta\right) S\left(E_\beta\right) \tag{1.21}$$

which would correspond to a beta spectrum with a neutrino squared mass equal to $-\sigma^2 = -\left(\langle V_i^2 \rangle - \langle V_i \rangle^2\right) < 0$!

Another non negligible systematic that concerns the end-point region of the spectrum is due to the presence of a radioactive background, which, due to the very poor statistics available in the region of interest, gives a significant contribution. An uncertainty δB in the radioactive background evaluation results in a distortion of the spectrum:

$$N_\beta = p_\beta E_\beta \left(E_0 - E_\beta\right)^2 \left(1 + \frac{\delta B}{p_\beta E_\beta \left(E_0 - E_\beta\right) F\left(Z, E_\beta\right) S\left(E_\beta\right)}\right) F\left(Z, E_\beta\right) S\left(E_\beta\right) \tag{1.22}$$

Also this deflection simulates a negative neutrino squared mass equal to $-2\delta B / \left[p_\beta E_\beta F S\right]$.

In order to increase the statistics of the events close to the end-point, a low Q-value β-decay is required (eq. 1.19). To date the most important results obtained by direct measurement of the neutrino mass are based on ^{3}H and ^{187}Re β-decays.

Tritium beta decay is a super-allowed transition with a low end-point energy of 18.6 keV. Thanks to its rather short half-life of 12.3 y, it is possible to create sources with high specific activity. This isotope is used in spectrometric experiments.

The beta decay of ^{187}Re is a unique first forbidden transition (tab. 1.4):

$$^{187}Re(5/2^+) \rightarrow ^{187}Os(1/2^-) + e^- + \overline{\nu}_e \tag{1.23}$$

Unlike non unique transitions, it is possible to calculate the nuclear matrix element, even if it is more difficult than in the case of Tritium. Rhenium becomes superconductor below its critical temperature $T_C = 1.4K$, has an elevated isotopic abundance (62.8%),

L=0,1	$\pi_i\pi_f = +1$	Allowed transitions
L=0,1	$\pi_i\pi_f = -1$	Non unique first forbidden transitions
L>0,1		Non unique L-th forbidden transitions
		Unique $(L-1)$-th forbidden transitions

TABLE 1.4: Classification of β-decays. $L = \Delta J = |J_f - J_i|$, where J and π are the spin and parity number, respectively.

a mean half-life of $42.3 \cdot 10^9$ y and a Q-value of 2.47 keV [35]. Since this isotope has the second lowest decaying energy known (the primacy belongs to ^{115}In [39]), it is a good candidate for the calorimetric direct measurement of the neutrino mass: thanks to the low transition energy, the useful fraction of events close to the end-point is ∼350 times higher in rhenium than in tritium.

1.3.1 Spectrometric experiments

The experiments aimed to the measurement of the neutrino mass that use spectrometers are divided into two categories: magnetic and electrostatic with magnetic collimation. The former select the energy of the electrons by means of the bending effect of a proper magnetic field, while in the latter the electrons are collimated by a magnetic field and then selected by a potential barrier. Before the '90s, the magnetic spectrometer were the most sensible instruments in the neutrino mass measurement, achieving a sensitivity of 10-20 eV. The electrostatic spectrometers are characterized by a higher energy resolution (∼ 1 eV for next generation experiments), a stronger rejection of the background and a higher luminosity.

The main advantage that makes spectrometers the most competitive technology in direct mass measurement experiments so far is the possibility of selecting of the electrons: only the useful fraction of electrons with energies very close to the transition energy can be selected. Therefore a very high statistics can be accumulated in the interesting interval.

On the other hand, this kind of approach has fundamental intrinsic limits, mainly due to the fact that the emitting source is external to the detector: this implies that the response function is a convolution of the exact transmission function T of the spectrometer with four correcting functions that take into account the effects of energy loss, source charging, backscattering from the substrate (present when the source is deposited on a

solid substrate) and the energy dependence of detection efficiency [40]. The experience with the Mainz and Troitzk experiments shows that other factors can also have a significant role: in Mainz convincing results were obtained only after including a *rugosity* effect of the tritium source [37], while in Trostzk a step function of unknown origin was introduced in the integral spectrum of the electron in order to get a significant result on the neutrino mass [36]. Last, the energy of possible excited states can not be detected, leading to the measurement of the sum of several energy spectrum, each with its own end-point energy (eq. 1.20).
Concluding, all these considerations suggest that obtaining a precise response function is a very delicate matter, where sources of systematic uncertainties are inevitable.

KATRIN The Karlsruhe Tritium Neutrino (KATRIN) is a new experiment based on a spectrometer that is expected to collect data of the tritium β-decay starting from 2016. In KATRIN the β-electrons will be emitted by a windowless gaseous ^{3}H source and will be guided adiabatically through the 70 meters long setup to the spectrometer, pushing this kind of technology to its very limit. A decay rate of 10^{11} is required from the source, which will be cooled at 27 K; a flux of 10^{19} T_2 molecules/s will be injected at the midpoint of the source. A crypumping section will guarantee a maximum T_2 flux entering in the spectrometer of 10^5 molecules/s, while a pre-spectrometer will select only the uppermost end of the β-spectrum in order to prevent background effects due to ionizing collisions. Background electrons, which are emitted from the spectrometer walls, will be screened off electrostatically by an inner grid system. The international collaboration of KATRIN aims to improve the present sensitivity of one order of magnitude down to 0.2 eV [41].

Project 8 Project 8 is a ambitious project aimed to introduce a new technique of measuring the neutrino mass. The proposed technique makes use of the radiation emitted during the cyclotron motion in order to extract the energy of the electron ejected in tritium beta decay [42]. In a constant magnetic field the electrons follow a cyclotron motion which occurs at a frequency that depends on the kinetic energy of the charged particle. By measuring the cyclotron radiation it is then possible to extract the original energy of the electrons, building in this way the beta spectrum exploiting the high precision which can be achieved in a frequency measurement.
It was recently demonstrated the capability of this technique to reconstruct the energy

of a mono-energetic source of electron with full with half maximum energy resolutions of 130 eV and 140 eV for the 17 keV and 30 keV emission lines of ^{83}Kr [43].

1.3.2 Calorimetric experiments

In an ideal calorimetric experiment the source is embedded inside the detector; in this way all the energy is detected, except for the fraction taken from the neutrino. In fact, provided that the temporal response of the detector is slow enough, the possible energy expended to excitep the atomic or molecular levels will be detected when these de-excite. In general the advantages of a calorimetric measurement are:

- capability to measure the excited levels
- no auto-absorption
- no backscattering
- no source substrate reflection

There is however a limitation related to this approach. The calorimeter experiments, in fact, are built to acquire the entire beta spectrum, this means that the count rate needs to be limited in order to keep the pile-up contribution as small as possible: two events happening in a time interval smaller than the time resolution would be detected as a single event with energy equal to the sum of the two, having as a consequence the distortion of the spectrum. Of course the more the detector response is slower, the more the pile-up is important.
Indicating with τ_R the detector time resolution and considering that the events follow the Poisson distribution, in a first approximation the fraction of events suffering pile-up is:

$$P\left(\Delta t < \tau_R\right) = 1 - \mathrm{e}^{A_\beta \tau_R} \approx A_\beta \tau_R \tag{1.24}$$

where A_β is the activity of the source and Δt is the time between two events. Considering the presence of pile-up, the beta spectrum is:

$$N'_\beta = N_\beta\left(Z, E\right) + \left(1 - \mathrm{e}^{-A_\beta \tau_R}\right) \int_0^{E_0} N_\beta\left(Z, E'\right) N_\beta\left(Z, E - E'\right) dE' \tag{1.25}$$

The number of spurious events affected by pile-up is obtained by integration of the pile-up spectrum in the interval ΔE below the end-point:

$$F^{pp}_{\Delta E} = A_\beta(1 - \mathrm{e}^{A_\beta \tau_R}) \int_{E_0-\Delta E}^{E_0} dE \int_0^{E_0} dE' N_\beta(Z, E') N_\beta(Z, E - E') \tag{1.26}$$

The beta spectrum observed in a calorimetric measurement is the combination of several spectra with the same end-point. In fact the equation (1.20) can be modified by making the following replacements:

$$E_\beta \to E'_\beta = E_\beta - V_i \tag{1.27}$$

$$p_\beta \to p'_\beta = (E'^2_\beta - m_e^2 - c^4)^{1/2} \tag{1.28}$$

that are justified since the detectors measure the electron energy and the atom de-excitations at the same time. Also observing that
$F\left(Z, E_\beta - V_i\right) S\left(E_\beta - V_i\right) \approx F\left(Z, E_\beta\right) S\left(E_\beta\right)$ and expanding in power series of V_i/E_β the resulting detected beta spectrum is:

$$\begin{aligned} N(Z, E_\beta, m_\nu) \approx p_\beta E_\beta (E_0 - E_\beta)^2 \left(1 - \frac{m_\nu^2 c^4}{(E_0 - E_\beta)^2}\right)^{1/2} F(Z, E_\beta) S(E_\beta) \\ \sum_i w_i \left(1 - \frac{V_i}{E_\beta} - \frac{V_i E_\beta}{E_\beta^2 - m_e^2 c^4} + \frac{V_i^2}{2(E_\beta^2 - m_e^2 c^4)}\right) \end{aligned} \tag{1.29}$$

In case of $m_\nu = 0$ the equation describes a linear Kurie plot also for energies close to the end-point[5]

1.3.3 Holmium 163

During the last decades the international community focused with increasing interest on the ^{163}Ho electron capture (EC) as a powerful means for neutrino mass determination. ^{163}Ho decays to ^{163}Dy with a convenient low transition energy that is estimated to be in the range 2.3 to 2.8 keV [44], with a recommended value of 2.555±0.016 keV [45] Since the capture is only allowed from the M shell or higher, the EC may be only detected through the mostly non radiative atom de-excitation of the daughter atom[6] and from

[5] the last term of 1.29 can be neglected ($E_\beta \gg V_i$).
[6] The intensity of the radiative decays respect to the non radiative ones is below one part per thousand.

the Inner Bremsstrahlung (IB) radiation. There are at least three proposed independent methods to estimate the neutrino mass from the ^{163}Ho EC: absolute M capture rates or M/N capture ratios [46], IB end-point [47] and calorimetric de-excitation spectrum end-point measurement [48].

Absolute M capture rates or M/N capture rate ratios The EC decay rate can be expressed as a sum over the possible levels of the captured electron [49]:

$$\lambda_{EC} = \frac{G_\beta^2}{4\pi^2} \sum_i n_i C_i \beta_i^2 B_i \left(E_0 - E_i\right) \left[\left(E_0 - E_i\right)^2 - m_\nu^2\right]^{1/2} \tag{1.30}$$

where $G_\beta = G_F cos\Theta_C$, n_i is the fraction of occupancy of the i-th atomic shell, C_i is the atomic shape factor, β_i is the Coulomb amplitude of the electron radial wave function and B_i is an atomic correction for electron exchange and overlap. It is important to note that every single addend of equation 1.30 has a dependence on m_ν.

Inner Bremsstrahlung end-point From eq. 1.14 it is evident that the measurement of the neutrino mass is possible because of the presence of the phase-space factor $(E_0 - E_\beta)\sqrt{(E_0 - E_\beta)^2 - m_{\nu_e}^2 c^4}$. A similar factor exists also for the emission rate of Internal Bremsstrahlung in Electron Capture (IBEC). To date, only one experiment actually measured the IBEC spectrum from ^{163}Ho decay, but the measurement was compromised by background [50].

Calorimetric absorption spectrum end-point The expression of the de-excitation spectrum has again a dependence on the neutrino mass through the phase-space factor, where the energy of the β-electron is replaced by the total de-excitation energy. The spectrum features Breit-Wigner peaks resonances centered at the ionization energies E_i of the captured electrons. Given the finiteness of the intrinsic width of the lines the total spectrum presents a continuum between adjacent peaks, coming from the overlap of the tails of every resonance. The distribution of the de-excitation energy E_c is [48]:

$$\frac{d\lambda_{EC}}{dE_c} = \frac{G_\beta^2}{4\pi^2} \left(E_0 - E_c\right) \sqrt{\left(E_0 - E_c\right)^2 - m_\nu^2 c^4} \sum_i n_i C_i \beta_i^2 B_i \frac{\Gamma_i}{2\pi} \frac{1}{\left(E_c - E_i\right)^2 + \Gamma_i^2/4} \tag{1.31}$$

As it happens for single beta decay, the spectrum is truncated at $E_0 - m_\nu$ and the sensitivity on m_ν is strictly related to the fraction of events at the end-point. If the end-point happens to be very close to the atomic resonance M1 the fraction of events that are sensitive to a non-zero neutrino mass will be strongly enhanced respect to single beta decay.

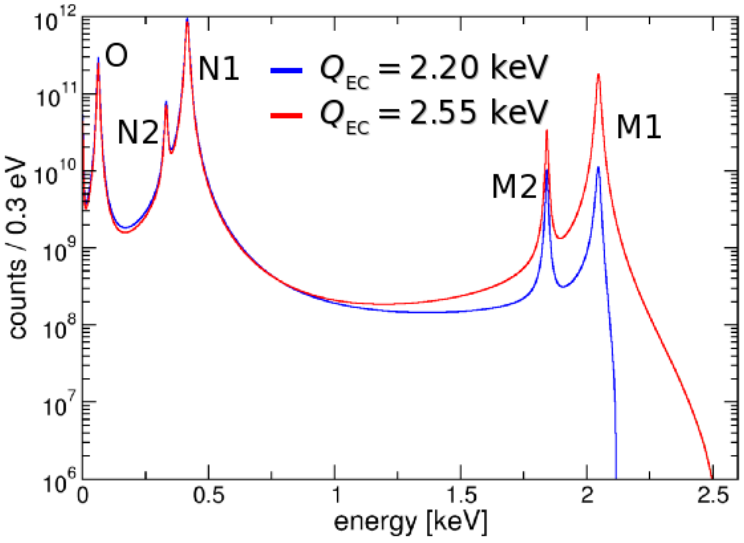

FIGURE 1.7: De-excitation spectrum coming from the EC of ^{163}Ho with two possible Q-values. The two spectra have been calculated considering an energy resolution $\Delta E_{FWHM} = 2$ eV, a fraction of events affected by pile-up $f_{pp} = 10^{-6}$ and a number of events $N_{ev} = 10^{14}$.

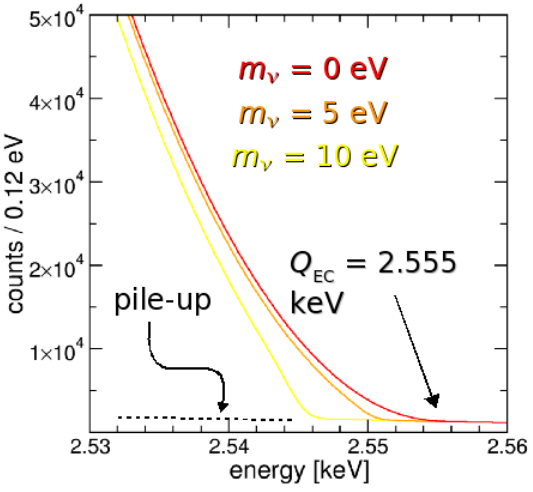

FIGURE 1.8: Effect of different values of m_ν on the shape of the ^{163}Ho spectrum at the end point. A Q=2.555 keV has been considered.

In figure 1.7 two spectra corresponding to two possible transition energies are plotted,

while in figure 1.8 the effects of a finite neutrino mass on the end-point are displayed, considering a Q=2.555 keV.

Statistical sensitivity In order to achieve a given statistical sensitivity on the neutrino mass the experimental setup, and in particular the detectors, must answer to strict requirements. A detailed Monte Carlo analysis about the required performances for a possible ^{163}Ho calorimetric experiment is described in [51]: in fig. 1.9 it is possible to appreciate how the total statistics N_{ev} is a crucial parameter for reaching a sub-eV neutrino mass statistical sensitivity, which scales as $N_{ev}^{-1/4}$. The energy resolution, in the range achievable with the present microcalorimeters technology, does not play a significant role, while the fraction of unresolved pile-up events has a strong effect on the statistical sensitivity (fig. 1.10).

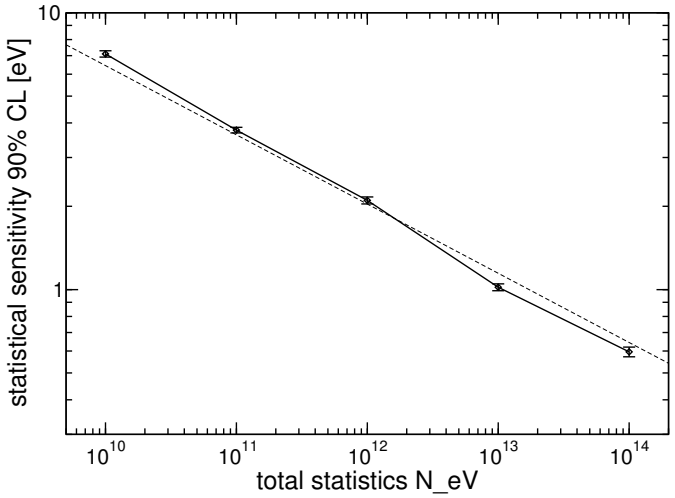

FIGURE 1.9: Statistical sensitivity on the neutrino mass as a function of the total events considering $\Delta E_{FWHM} = 1$ eV, $f_{pp} = 10^{-5}$ and $Q = 2.6$ keV.

The perfect detector candidate must possess a large scalability ($\gtrsim 10^3$) and a fast response ($\sim \mu$s), in order allow the acquisition of the highest possible statistics while keeping the contribution of the pile-up events as small as possible.

1.3.4 Superconducting microresonators and neutrino mass physics

The aim of the project started within this thesis is to adapt the existing technology of microwave superconducting microresonator to be applicable to a possible next generation calorimetric experiment aimed to the neutrino mass measurement with the ^{163}Ho. Such

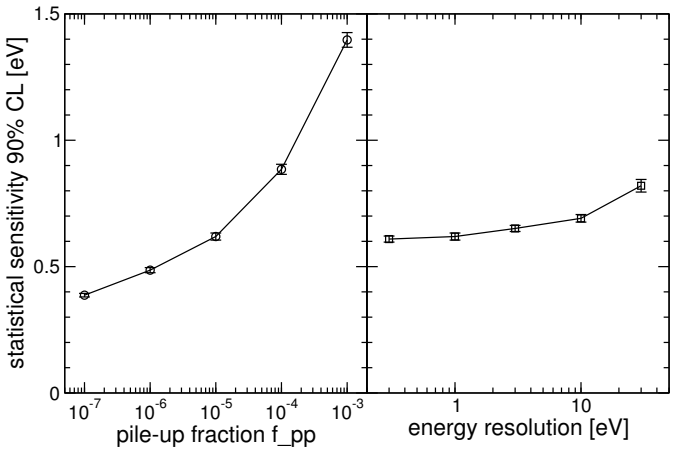

FIGURE 1.10: Statistical sensitivity on the neutrino mass as a function of the pile-up fraction and energy resolution. Left: $N_{ev} = 10^{14}$, $\Delta E_{FWHM} = 1$ eV, $Q = 2.6$ keV. Right: $N_{ev} = 10^{14}$, $f_{pp} = 10^{-5}$, $Q = 2.6$ keV.

technology would exploit the frequency multiplex typical of these detectors together with an excellent theoretical and time resolution. In this way it would be feasible to design calorimetric experiments capable to acquire enough statistics to push the neutrino mass limit down below the eV sensitivity by keeping the pileup contribution as low as possible. The idea would be to embed the isotope directly in the sensitive part of the detector to perform a calorimetric measurement of the decay. Nevertheless a preliminary work aimed to adapt the devices to the detection of single particles is mandatory.

In order to be applicable to such experiments, these detectors must achieve a very fast response, of the order of the μs, and an energy resolution of $\sim$ eV on the energy scale of the keV.

Chapter 2

Superconducting microwave microresonators

The potential of Low Temperature Detectors (LTDs) for applications requiring very high sensitivity was realized more than 50 years ago with the introduction of cryogenic bolometers using semiconducting thermistors [52]. Since then, they become a reliable and mature technology used in a broad variety of application. The use of LTDs as particle detector applied to the neutrino physics was proposed in 1984 [53]. In this chapter a brief overview of the main existing LTDs will be given, focusing then on the object of this work: superconducting microwave microresonators.
The sensors described in the following summary are used as thermal detectors that sense the variation of temperature of an absorber chosen accordingly to the application they are required for.

Semiconducting bolometers These devices measure the temperature rise of the absorber by sensing the variation of the resistance of a semiconducting thermistor, achieving energy resolutions up to few eVs on the keV energy range [54]. In order to obtain a high sensitivity thermistor, the semiconductor is doped in such a way that the derivative of the resistance versus the temperature is maximum at the operating temperature, which has to be around few mKs so that the thermal capacitance of the absorber is as low as possible. This requirement brings to have high impedance thermistors: to contain the signal RC integration due to the stray capacitance, and hence allowing a relatively fast[1]

[1]The time response is ultimately limited by the electron-phonon coupling

response of the detector, a cold JFET stage is mandatory. The JFET amplifiers used with these devices operate around 120 K, much higher than the detector temperature. Running individual wiring between the two temperature stages is impractical for large arrays, effectively limiting the growth of array sizes at few hundred detectors. With MOSFET amplifiers it is possible to break this barrier [55]: this kind of transistor can in fact operate near the temperature of the detectors, enabling in this way a modest increase in the multiplex factor. On the other hand, the MOSFET are considerably noisier then JFETs, degrading in this way the performances achievable with the detectors.

Transition Edge Sensors Transition Edge Sensors (TESs) are used as thermometers that operate on the very sharp transition of a superconducting material. In this way, a small change in temperature of the absorber results in a great change in the resistance, making the TES a very sensitive device. Although the TESs have been used for many years in various applications, stable operation of large array was made possible only after that the voltage-biased electro-thermal feedback (ETF) mode of operation was invented [56]: in opposite to the traditional bolometer current biasing, the TESs are voltage-biased, avoiding the problem of the bolometer heating. This biasing technique is characterized by a negative feedback, preventing the detector to move from the working point. The TESs can be designed with low impedance, making them suitable to match to a Superconducting Quantum Interference Device (SQUID), which, given its low power dissipation, can be placed at the same temperature stage of the detectors: these characteristics make of the TESs a more easily multiplexable technology respect to semiconducting thermistors. To date, the techniques used to multiplex TESs are by time-division multiplexing [57], frequency-domain multiplexing [58] and code-division multiplexing [59]. A very promising approach that consists in reading the SQUIDs by making them part of resonant circuits has been also demonstrated [60, 61], and it is going to be used in the HOLMES neutrino mass experiment [62].

Metallic Magnetic Calorimeters Metallic Magnetic Calorimeters (MMCs) detect the temperature raise of a paramagnetic sensor by measuring the variation of its magnetization. Typically the detector consists of a metallic absorber strongly thermally linked to the sensor. The readout is made by a SQUID amplifier, so the same multiplexing technique as for TESs could be in principle applied.

Superconducting Tunnel Junction In Superconducting Tunnel Junction detectors (STJ), or Quantum Giaever detectors, the energy is absorbed by a superconducting metallic electrode, where an amount of Cooper pairs proportional to the absorbed energy are broken and turned into quasi-particles. The detector is basically a Josephson junction: it is composed by two superconductors separated by a very thin layer of insulating material, so thanks to the *tunnel effect*, a current can pass through the junction. The number of the quasi-particles out of the thermal equilibrium can be determined by monitoring the current pulse caused by the tunneling of the quasi-particles through the tunnel barrier. As concerning the multiplex of these detectors, given their high impedance their read-out is usually made by JFET as in the case of semiconducting thermistors, so the same scenario applies also in this case. Nevertheless, unlike semiconducting thermistors, here the time resolution is limited by the quasi-particle lifetime, which is of the order of μs.

2.1 Superconductivity

All the metals show that their resistivity decreases when the temperature they are at is lowered, but only a special class of metals named *superconductors* have the characteristic to have zero resistance to the flow of a DC current below a *critical temperature* T_c. This phenomenon was first discovered by Heike Kamerlingh Onnes in 1911, within his studies on the electrical resistance of solid mercury at cryogenic temperatures [63]. An important step towards a complete understanding of superconductivity was made in 1933 by Meissner and Ochsenfeld with the discovery of the perfect diamagnetism of superconductors, later on called *Meissner effect* [64]. This implies that a superconductor expels every magnetic field[2] from within its bulk allowing only the penetration of magnetic field within a small distance, called *penetration depth*, which is usually of the order of few tens of μm.

The absence of electrical resistance can be explained in this way: the electrons, given their negative charge, tend to repulse one another, still they are attracted from the positively charged ions of the lattice. When the thermal agitation of the lattice is small enough, this attraction can distort the lattice in such a way that at long distances the repulsion between the electrons is overcame. It happens in this way that two electrons

[2] below a *critical field*, that is characteristic of the material

are bound together to form a *Cooper pair* [65] with a binding energy Δ at 0 K called *gap* that according to the BCS (Bardeen, Cooper and Schrieffer) theory [66] is:

$$2\Delta \approx 3.5 k_B T_c \tag{2.1}$$

where k_B is the Boltzman constant. The peculiar characteristic of the Cooper pair is that since it is a doublet of electrons, it behaves like a boson: in this way it does not have to obey to the Pauli exclusion principle, and can condensate on the ground state into a superfluid that flows without any dissipation. The superconductors can be classified in two types[3]: type I superconductors are mainly pure elements and usually have low critical temperatures while type II superconductors are usually alloys or ceramic materials.

2.1.1 The Drude model for normal state metals

The conduction due to the electrons in normal state metals can be described by the Drude model [68]. In this model, the conductivity is given by a gas of free electrons (*quasi-particles*) that will be accelerated by an external electrical field **E**. Given the average time τ occurring between two scattering events, which is a characteristic parameter of the metal, it is possible to write the equation of motion of the electrons:

$$\frac{\langle d\mathbf{p}_{qp}(t)\rangle}{dt} = e\mathbf{E} - \frac{\langle \mathbf{p}_{qp}(t)\rangle}{\tau} \tag{2.2}$$

where $\langle \mathbf{p}_{qp}\rangle$ is the average momentum of the quasi-particles and e is the charge of the electron. The second term of the equation expresses the resistance to the motion due to the scattering of the quasi-particles. The current density **J** is then given by the Ohm's law:

$$\mathbf{J} = n_{qp} e \langle \mathbf{v}_{qp}(t)\rangle = \frac{n_{qp} e}{m} \langle \mathbf{p}_{qp}(t)\rangle = \sigma \mathbf{E} \tag{2.3}$$

where n_{qp} and $\langle \mathbf{v}_{qp}\rangle$ are the density and average velocity of the quasi-particles, m is the electron mass and σ is the electrical conductivity. Combining the eq. 2.2 with eq. 2.3 for steady currents (i.e. the left side of eq. 2.2 is equal to zero), one obtains the DC

[3] for completeness a third type exists, with combined properties of the other two types: 1.5 Type superconductors [67].

conductivity of a normal metal:

$$\sigma_n^{DC} = \frac{n_{qp} e^2 \tau}{m} \tag{2.4}$$

In the more general case of a harmonic current, the average momentum can be expressed as $\langle \mathbf{p}_{qp} \rangle = \mathbf{p}_0 e^{j\omega t}$. Inserting this expression in eq. 2.2, resolving for $\langle \mathbf{p}_{qp} \rangle$ and substituting in eq. 2.3, one gets the normal AC conductivity:

$$\sigma_n^{AC} = \frac{\sigma_n^{DC}}{1 - j\omega\tau} = \frac{n_{qp} e^2 \tau}{m\,(1 + \omega^2\tau^2)} - j\omega \frac{n_{qp} e^2 \tau^2}{m\,(1 + \omega^2\tau^2)} \equiv \sigma_{1n} - j\sigma_{2n} \tag{2.5}$$

The imaginary term is due to the inertia of the quasi-particles: once they have acquired momentum and the field is reversed, it will take some time for them to reverse their motion. This term for normal metals at microwave frequencies is negligible compared to the first term in eq. 2.5 as long as the scattering time τ is small compared to the period of the field: in this case the impedance will be purely dissipative.

2.1.2 London equations

The two macroscopic characteristics of superconductors - zero DC resistance and perfect diamagnetism - have been well described in 1935 by Fritz and Heinz London [69]. Their two equations can be derived replacing the quasi-particles with the Cooper pairs as charge carriers and using a quantum mechanical approach: in eq. 2.3 the momentum is replaced by minimal coupling of the quantum mechanics

$$\mathbf{p} = m\mathbf{v} - \frac{q}{c}\mathbf{A} \tag{2.6}$$

where c is the speed of light and $\mathbf{A}$ is vector potential of the magnetic field. Arguing that in the absence of an applied field a zero net canonical momentum on the ground state is expected (by virtue of Bloch theorem - see pag. 143 of [70]), the local average velocity becomes:

$$\langle \mathbf{v}_s \rangle = -\frac{e}{mc}\mathbf{A} \tag{2.7}$$

from which[4]:

$$\mathbf{J} = n_s e \langle \mathbf{v}_s \rangle = -\frac{n_s e^2}{mc}\mathbf{A} \tag{2.8}$$

[4]the equation 2.8 is not gauge-invariant, it is then correct only by requiring that $\mathrm{div}\mathbf{A} = 0$, which is known as the London gauge.

Taking the time derivative or taking the curl of eq. 2.8 one gets the two London equation:

$$\frac{\partial \mathbf{J}_s}{\partial t} = \frac{n_s e^2}{m}\mathbf{E} \tag{2.9}$$

$$\nabla \times \mathbf{J}_s = -\frac{n_s e^2}{mc}\mathbf{B} \tag{2.10}$$

The first of the two equations describes the zero resistance of a superconductor since the electric field accelerate the electrons indefinitely; the equation could be also derived with the same approach used in sec. 2.1.1 and setting $\tau \to \infty$, which is the condition of no scattering, i.e. zero resistance.

The equation 2.10 instead expresses the perfect diamagnetism. Combining it with the Maxwell equation $\nabla \times \mathbf{B} = \frac{4\pi}{c}\mathbf{J}$ one gets the following differential equation for $\mathbf{B}$:

$$\nabla^2 \mathbf{B} = \frac{\mathbf{B}}{\lambda_L^2} \tag{2.11}$$

with $\lambda_L = \sqrt{\frac{mc^2}{4\pi n_s e^2}}$. The solution of the equation is therefore a decreasing exponential, meaning that the field is exponentially screened inside a superconductor with a penetration depth λ_L, which is nothing else but the Meissner effect. Also time-varying electric fields are shielded at the same way: making the time derivative of the Maxwell equation $\nabla \times \mathbf{B} = \frac{4\pi}{c}\mathbf{J_s}$, combining it with eq. 2.9 and finally considering the other Maxwell equation $\nabla \times \mathbf{E} = -\frac{1}{c}\frac{\partial \mathbf{B}}{\partial t}$, one gets also for the electric field:

$$-\nabla \times \nabla \times \mathbf{E} = \nabla^2 \mathbf{E} = \frac{\mathbf{E}}{\lambda_L^2} \tag{2.12}$$

Of course, the *London penetration depth* depends on the temperature through the the density of the Cooper pairs n_s, but it has an upper limit at $T = 0$ K set by the maximum number of superconducting carriers which is equal to the density of quasi-particles when the metal is in the normal state n:

$$\lambda_L(0) = \sqrt{\frac{mc^2}{4\pi n e^2}} \tag{2.13}$$

Empirically, the temperature dependence of the London penetration depth is found to be approximated by:

$$\lambda_L(T) \approx \lambda_L(0)\left[1 - (T/T_c)^4\right]^{-1/2} \tag{2.14}$$

As one would expect, the increase of the temperature cause the penetration depth to continuously increase and diverge for $T = T_c$.

2.1.3 The two fluid approximation

When a superconductor is held at a temperature between 0 K and its T_c, not all the electrons are combined into pairs, so there will be two distinct populations (quasi-particles, denoted by their density n_{qp}, and Cooper pairs, n_s) that will contribute to the total conductance. From the first London equation (eq. 2.9), for a harmonic current the conductivity due to the superconducting population is given by:

$$\sigma_s = -j\frac{n_s e^2}{m\omega} \tag{2.15}$$

It is clear that for $\omega = 0$, σ_s diverges as expected: the total conductivity DC currents is strongly dominated by the dissipationless conductivity of the Cooper pairs. On the other hand at high frequencies the superconducting carriers suffer of a finite reactance, which is due to the inertia of the Cooper pairs which, since they do not scatter, can store an energy that can be extracted by reversing the field, process that results in a phase shift of 90° respect to the applied field. This reactance is called *kinetic inductance*. As the frequency increases, the superconducting reactance increases as well, letting the parallel ohmic conduction channel given by the quasi-particles to become more and more important (eq. 2.5), introducing in this way a significant dissipative term into the total conductivity. According to this model, the quasi-particles contribution provides nonzero dissipation in superconductors at all nonzero frequencies[5], explaining in this way the finiteness of the Q factors of superconducting resonators. A similar argument can be done for the temperature: from the expressions of σ_s and σ_n, they both appear to be proportional to the density of their own charge carrier. While the temperature increases, n_s decreases and n_{qp} grows, making the dissipation term of the quasi-particles non negligible.

In this picture, the total conductivity of a superconductor is given by the sum of the contribution of the two population:

$$\sigma = \sigma_1 - j\sigma_2 \tag{2.16}$$

[5] considering $\hbar\omega < 2\Delta$

where: $\sigma_1 = \frac{n_{qp}e^2\tau}{m(1+\omega^2\tau^2)}$ and $\sigma_2 = \frac{n_s e^2}{m\omega} + \omega\frac{n_{qp}e^2\tau^2}{m(1+\omega^2\tau^2)}$.
The approximation just described, called *two fluid model*, was developed in 1934 by Gorter and Casimir [71]. Since then remarkable theoretical progresses have been done in the description of superconductors, still this model remains useful from the qualitatively point of view.

2.1.4 The inductance of superconductors

The working principle of the superconducting microwave microresonators is based on the kinetic inductance of superconductors, that from the circuital point of view behaves just like a normal inductance. It is then important to understand all the contribution to the total inductance. In order to have a simple model, a strip of superconductor with thickness t and width W will be considered, in which two contributions to the total inductance are present: the kinetic inductance L_k, related to the kinetic energy of the Cooper pairs, and the geometric inductance L_g, due to the energy stored in the magnetic field inside the superconductor that in general depends on the geometry of the circuit.
The kinetic energy of the pairs is easily calculated:

$$E_k = \frac{1}{2}n_s m \left|\mathbf{v}_s\right|^2 \tag{2.17}$$

E_k can be expressed as function of the current density:

$$\mathbf{J}_s = n_s e \mathbf{v}_s \tag{2.18}$$

then, recalling the expression of the London penetration depth present in eq. 2.11:

$$E_k = \frac{1}{2}m\frac{\left|\mathbf{J}_s\right|^2}{n_s e^2} = \frac{2\pi}{c^2}\lambda_L^2 \left|\mathbf{J}_s\right|^2 \tag{2.19}$$

It is now possible to define the kinetic inductance with the definition of the total energy per unit length:

$$U_k = \frac{1}{2}L_k I^2 = \frac{2\pi}{c^2}\lambda_L^2 \int_S \left|\mathbf{J}_s\right|^2 \tag{2.20}$$

The integration is performed over the cross-section of the strip S; the current though flows only in a small area of thickness $\sim \lambda_L$ under the surface of the strip. It can be useful to calculate the L_k in some special cases. For the following calculation, the

approximation $t \ll W$ will be always adopted, and three cases will be considered: case 1) $\lambda_L \ll t$, case 2) $\lambda_L \gg t$ and case 1.5) an intermediate situation.

case 1 The current density is now integrated on the effective cross-section given by $2W\lambda$, so the current density is $|\mathbf{J}_s| = I/(2W\lambda_L)$. Inserting it in eq. 2.20 it is possible to evaluate the kinetic inductance:

$$\frac{1}{2}L_k I^2 = \frac{1}{2}\frac{2\pi}{c^2}\frac{\lambda_L}{W}I^2 \Longrightarrow L_k = \frac{2\pi}{c^2}\frac{\lambda_L}{W} \tag{2.21}$$

case 2 In such a situation the current can be considered uniform over the whole cross-section of the strip, which is equal to $|\mathbf{J}_s| = I/Wt$. Following the same calculation as in case 1, the kinetic inductance results to be:

$$L_k = \frac{4\pi}{c^2}\frac{\lambda_L^2}{Wt} \tag{2.22}$$

case 1.5 In real situations this is the most common condition, where one is in the middle of the two previous cases. The calculation of the inductance is rather complex and only the results are here reported[6]:

$$L_k = \frac{\pi\lambda_L}{Wc^2}\left[\coth\left(\frac{t}{2\lambda_L}\right) + \left(\frac{t}{2\lambda_L}\right)\mathrm{cosec}^2\left(\frac{t}{2\lambda_L}\right)\right] \tag{2.23}$$

$$L_g = \frac{\pi\lambda_L}{Wc^2}\left[\coth\left(\frac{t}{2\lambda_L}\right) - \left(\frac{t}{2\lambda_L}\right)\mathrm{cosec}^2\left(\frac{t}{2\lambda_L}\right)\right] \tag{2.24}$$

It is now possible to write the total inductance in H/square as:

$$L_{tot} = L_g + L_k = \frac{2\pi\lambda_L}{c^2}\coth\left(\frac{t}{2\lambda}\right) \tag{2.25}$$

It is clear from eq. 2.25 that the inductance depends on both the thickness of the superconductor and on the temperature through the penetration depth.

[6] For a more detailed discussion, see appendix of [72].

2.1.5 The complex surface impedance

A very complete, even though rather complex, description of superconductors is given in the Mattis-Bardeen theory [73], which provides the complex conductivity of superconductors in a more sophisticated and complete way respect to what described so far. Calling σ_n the normal conductivity of the metal, the real and complex terms of the conductance in this theory are given by[7]:

$$\frac{\sigma_1(\omega)}{\sigma_n} = \frac{2}{\hbar\omega}\int_{\Delta}^{\infty} dE \frac{E^2+\Delta^2+\hbar\omega E}{\sqrt{E^2-\Delta^2}\sqrt{(E+\hbar\omega)^2-\Delta^2}}\left[f(E)-f(E+\hbar\omega)\right] \tag{2.26}$$

$$\frac{\sigma_2(\omega)}{\sigma_n} = \frac{1}{\hbar\omega}\int_{\Delta}^{\Delta+\hbar\omega} dE \frac{E^2+\Delta^2+\hbar\omega E}{\sqrt{E^2-\Delta^2}\sqrt{\Delta^2-(E-\hbar\omega)^2}}\left[1-2f(E)\right] \tag{2.27}$$

At low frequencies and temperature, such as $\hbar\omega \ll \Delta_0$ and $k_B T \ll \Delta_0$, the two previous relations can be simplified into

$$\frac{\sigma_1(\omega)}{\sigma_n} \approx \frac{4\Delta}{\hbar\omega} \mathrm{e}^{-\Delta_0/k_B T} \sinh(\xi) K_0(\xi) \tag{2.28}$$

$$\frac{\sigma_2(\omega)}{\sigma_n} \approx \frac{\pi\Delta}{\hbar\omega}\left[1-2\mathrm{e}^{-\Delta_0/k_B T}\mathrm{e}^{-\xi} I_0(-\xi)\right] \tag{2.29}$$

with I_0 and K_0 modified Bessel functions of first and second kind, respectively, and $\xi = \frac{\hbar\omega}{2k_B T}$.

Nevertheless the complex conductivity is not a quantity directly accessible experimentally, while the *complex surface impedance* can be probed. From the Meissner effect it is known that the fields are expelled from the bulk of a superconductor, while they can penetrate for a depth equal to λ_L below the surface. The result is that for superconductors a complex surface impedance can be defined:

$$Z_s = R_s + j\omega L_s \tag{2.30}$$

The complete calculation of the complex conductivity is rather complicated and usually requires numerical methods, but few limiting cases can be solved analytically. In the following a summary from [74] is reported, where the surface impedance is related to the complex conductivity calculated with the Mattis-Bardeen equations (2.26 and 2.27); the

[7] for simplicity where not indicated otherwise Δ is the gap parameter at the temperature T, while Δ_0 is the gap parameter at $T = 0$ K.

film of thickness t will be considered "thin" or "thick" in the cases where they have $t \ll \lambda$ or $t \gg \lambda$, respectively, while the "local" term will be referred to situations where the superconducting film possesses an electron mean free path shorter than the penetration depth. Opposite to the local limit, there is the "extreme anomalous" regime, where the electron mean free path is long compared to the penetration depth, making the response no longer local.

thick film, local limit

$$Z_s = \sqrt{\frac{j\mu_0\omega}{\sigma(\omega,T)}} = \frac{Z_s(\omega,0)}{\sqrt{1+j\delta\sigma(\omega,T)/\sigma_2(\omega,0)}} \tag{2.31}$$

with $\delta\sigma(\omega,T) = \sigma(\omega,T) - \sigma(\omega,0) = \sigma_1(\omega,T) - j\delta\sigma_2(\omega,T)$. The last equality is the consequence that at $T = 0$ K all the quasi-particles are combined into pairs, resulting in a purely reactive impedance which can be written as function of the penetration depth:

$$Z_s(\omega,0) = j\omega\mu_0\lambda_{loc} \tag{2.32}$$

where the penetration depth in the local limit λ_{loc} is:

$$\lambda_{loc} = \sqrt{\frac{\hbar}{\pi\Delta\mu_0\sigma_n}} \approx 105 \text{ nm } \times \sqrt{\frac{\rho_n}{1\ \mu\Omega \text{ cm}}\frac{1 \text{ K}}{T_c}} \tag{2.33}$$

thick film, extreme anomalous limit

$$Z_s(\omega,T) = j\omega\mu_0\lambda_{e.a.}\left[1+j\delta\sigma(\omega,T)/\sigma_2(\omega,0)\right]^{-1/3} \tag{2.34}$$

where $\delta\sigma$ follows the same convention as before; calling l the electron mean free path, the penetration depth is:

$$\lambda_{e.a.} = \lambda_{loc}\left(\frac{\sqrt{3}l}{2\pi\lambda_{loc}}\right)^{1/3} \tag{2.35}$$

thin films

In the case that the current density can be considered constant in the whole cross-sectional area of the film, the impedance becomes:

$$Z_s(\omega,T) = j\omega\mu_0\lambda_{thin}\left[1+j\delta\sigma(\omega,T)/\sigma_2(\omega,0)\right]^{-1} \tag{2.36}$$

where the penetration depth here has become:

$$\lambda_{thin} = \frac{\lambda_{loc}^2}{t} \tag{2.37}$$

This case is of particular interest for the work described in this thesis since the devices utilized fall into this category. From eq. 2.33 it is possible to see that the local penetration depth is proportional to $\sigma_n^{-1/2} = \rho_n^{1/2} \propto t^{-1/2}$, where ρ_n is the resistivity of the normal state, so:

$$\lambda_{thin} \propto 1/t^2 \tag{2.38}$$

This characteristic, as it will be shown in the next chapter, has to be kept into account while designing the detectors to match the target performances.

All the results listed can be summarized in one single relationship between the complex conductivity and the surface impedance:

$$\frac{\delta Z_s(\omega, T)}{Z_s(\omega, 0)} \approx -\gamma \frac{\delta\sigma(\omega, T)}{\sigma(\omega, 0)} \tag{2.39}$$

with γ is 1, 1/2 or 1/3 for thin, local or extreme anomalous approximations, respectively. The devices considered in this thesis are in the thin limit, so $\gamma = 1$.

2.2 Superconductors as ionizing radiation detectors

Among the ionizing radiation detectors made of superconductors, there are superconducting microwave microresonators, also know as MKIDs (Microwave Kinetic inductance Detectors) [75], the subject of this thesis. They detect any energy E greater than 2Δ that is released inside the superconductor they are made of. By sensing the number of quasi-particles out of the thermal equilibrium, they measure the variation of quasi-particles inside the volume of the detector due to the absorption of energy. The variation in the number of quasi-particles (and hence in the number of Cooper pairs), will change the conductivity of the metal, affecting in this way the complex surface impedance, that can be sensed by making the superconductor part of a resonant circuit. The detection of an energetic event will be done through the observation of the parameters of the resonance.

2.2.1 Quality factors

An important quantity that describes how a resonator is dissipationless is the quality factor Q. If a resonant circuit is excited it will oscillate dissipating energy exponentially with a time constant τ. The quality factor expresses how a resonant system is capable to store energy without dissipation and can be defined as

$$Q = 2\pi \frac{\text{energy stored}}{\text{energy dissipated per cycle}} = 2\pi f_0 \frac{\text{energy stored}}{\text{dissipating power}} \tag{2.40}$$

Calling $\omega_0 = 2\pi f_0$ the resonant angular frequency, the quality factor can be rewritten as $Q = \omega_0 \tau$. Another useful way of expressing the quality factor is $Q = f_0/\Delta f$, where Δf is the bandwidth of the resonator, for the demonstration see appendix C.
In the case of MKIDs the resonators will loose energy both for dissipative losses, related to an internal quality factor Q_i that describes the energy loss due to the quasi-particles, and for the coupling of the resonator to the transmission line used to excite it, described by the coupling quality factor Q_c. The overall resonator quality factor Q is given by

$$(Q)^{-1} = (Q_i)^{-1} + (Q_c)^{-1} \tag{2.41}$$

2.2.2 The scattering matrix

A very useful notation used to describe microwave circuits in terms of the reflected and transmitted waves as a function of the incident one is the scattering matrix, most commonly called S-matrix. For a two ports network (fig. 2.1), as it is the usual setup for MKIDs, this matrix has dimension 2×2. Adopting the convention that V_n^+ express an incident voltage wave at the n-th port and V_n^- is the wave traveling from the n-th port, the matrix is defined in the following way [76]:

$$\begin{pmatrix} V_1^- \\ V_2^- \end{pmatrix} = \begin{pmatrix} S_{11} & S_{12} \\ S_{21} & S_{22} \end{pmatrix} \begin{pmatrix} V_1^+ \\ V_2^2 \end{pmatrix} \tag{2.42}$$

Each S parameter of 2.42 can be computed as:

$$S_{ij} = \frac{V_i^-}{V_j^+} \tag{2.43}$$

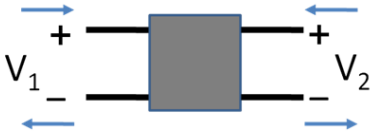

FIGURE 2.1: Two ports network.

$S_{21} = V_2^-/V_1^+$ is the ratio between the voltage wave traveling from the port 2 and the wave incident on the port 1 which is the transmitted signal from the port 1 to the port 2: in the analysis of MKIDs this is the most interesting among the S parameters.
For a capacitively coupled resonator like the one represented in fig. 2.2 the transmission response as a function of frequency is described by

$$S_{21}(\omega) = 1 - \frac{Q}{Q_c}\frac{1}{1 + 2jQx} \tag{2.44}$$

where $x = (f - f_0)/f_0$ is the detuning of the generated signal respect to the resonant frequency.

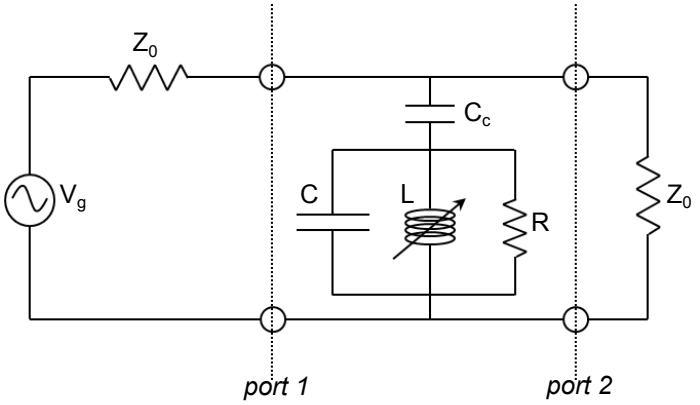

FIGURE 2.2: Electrical scheme of the two ports network with a resonators capacitively coupled through the capacitance C_c to the transmission line. The impedance on the right of the port 2 represents the input impedance of a signal amplifier.

The equation 2.44 maps the real axis of the frequencies into a circle in the complex plane, resulting in a phase shift of the transmitted signal while crossing the resonant frequency of 2π (fig. 2.3). For f far away from f_0 the transmission amplitude is equal to 1, while it reaches its minimum at the resonant frequency f_0: $\min|S_{21}| = 1 - Q/Q_c$ (fig. 2.4).

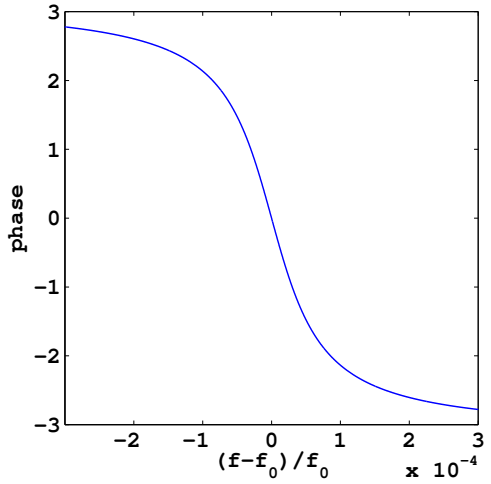

FIGURE 2.3: Phase of the transmitted signal near the resonant frequency for $f_0 = 4$ GHz, $Q_i = 10^5$ and $Q_c = 10^4$.

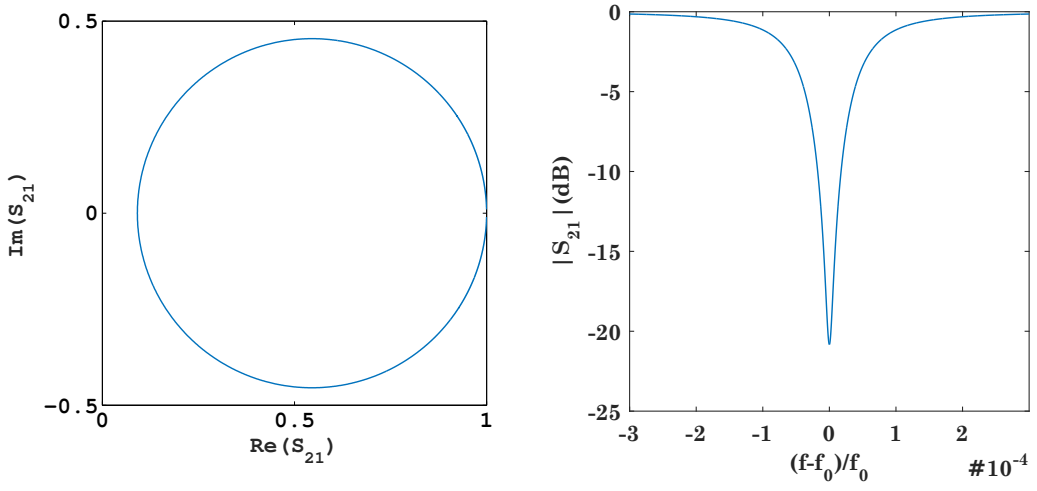

(A) (B)

FIGURE 2.4: Resonance profile obtained with $f_0 = 4$ GHz, $Q_i = 10^5$ and $Q_c = 10^4$. (A) Resonance circle in the complex plane: far away from the resonance the amplitude is equal to the unity; for $f = f_0$ it reaches its minimum value, equal to $1 - Q/Q_c$. (B) Amplitude of the transmitted signal through the transmission line expressed in dB of attenuation.

2.2.3 Resonator response

When an energy E greater than the Cooper pair binding energy ($2\Delta \sim$ meV) is released inside the superconductor, an amount of pairs proportional to E is broken into quasi-particles:

$$\delta N_{qp} = \eta \frac{E}{\Delta} \tag{2.45}$$

here η is an efficiency coefficient that takes into account the fraction of energy that is spent in the breaking of the pairs, which is usually around 0.5. As a consequence on one hand the drop of the pairs leads to an increase of the kinetic inductance, resulting in a lowering of the resonant frequency. On the other hand the growth of the quasi-particles density leads to a rise of the surface resistance, resulting in a reduction of the internal quality factor Q_i. The detection of energetic events in the detector is then made by constantly monitoring the resonant frequency and the internal quality factor of the resonator. These two channels will be referred in the following as the *inductive* (or *frequency*) channel and as *dissipative* (or *amplitude*) channel, respectively.

After the absorption of the energy, the quasi-particles can diffuse over a distance $l \approx D\tau_{qp}$, where D is the material-related diffusion constant. After some time two quasi-particles will eventually meet and, by emitting a phonon, they will recombine. This process follows an exponential law with a time constant called quasi-particle lifetime or recombination time (τ_{qp}), which is characteristic of the material and it is function of temperature.

The read-out of the observable quantities - resonant frequency and amplitude - is realized experimentally by exciting the resonator with a single tone with frequency equal to the resonant frequency: given the characterization of the resonator it will be possible to reconstruct the quantities of interest (fig. 2.5). In a more analytic way, remembering the equation 2.44 it is possible to calculate the frequency shift and the amplitude variation:

$$\delta A = \frac{1}{Q_c} \delta \left[\mathrm{Re} \left(\frac{1}{1 - S_{21}} \right) \right] \tag{2.46}$$

$$\delta f = \frac{f_0}{2Q_c} \delta \left[\mathrm{Im} \left(\frac{1}{1 - S_{21}} \right) \right] \tag{2.47}$$

It is useful to understand the response of the detector to the variation of the quasi-particle density. In order to do so the equivalence between the creation of quasi-particles

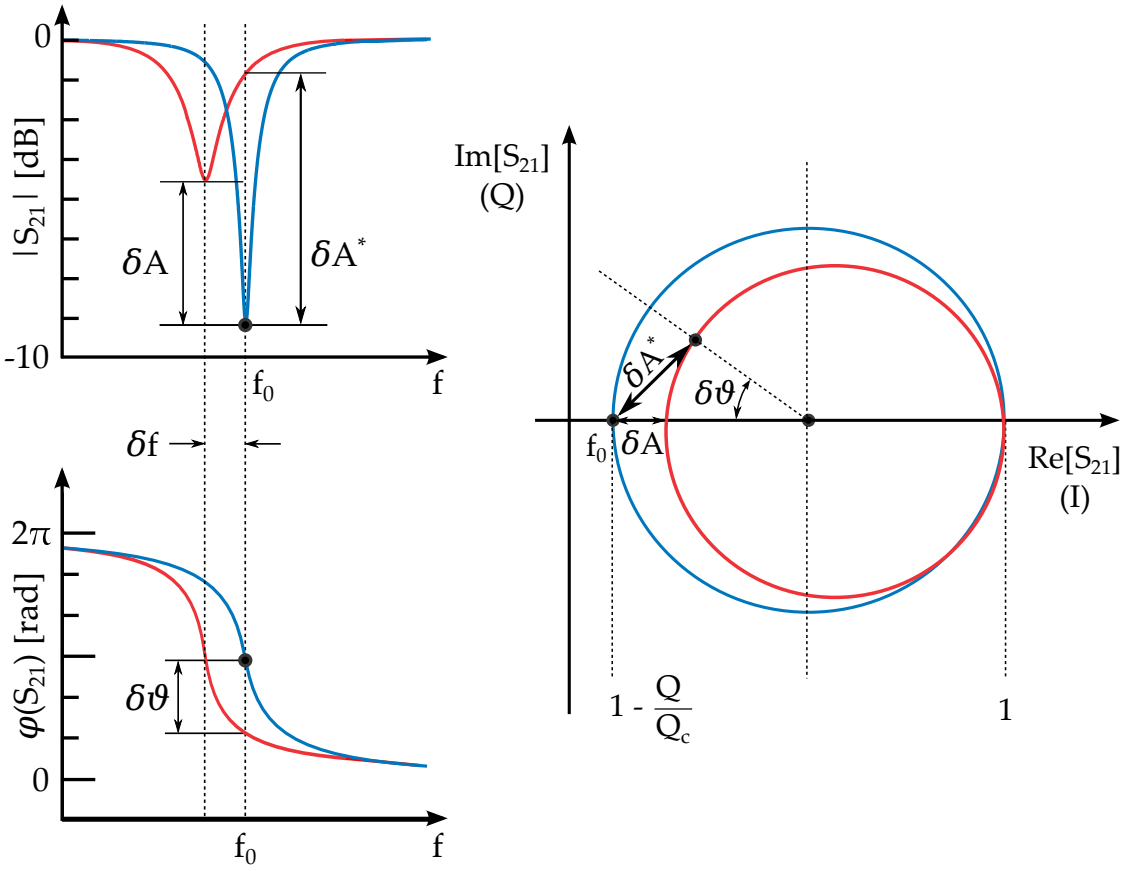

FIGURE 2.5: The unperturbed resonance profile (blue line) and the same resonance after an energy is absorbed (red line). It is possible to see how the resonant frequency has shifted of δf and how the quality factor has been reduced leading to a variation of amplitude δA of the transmitted signal. The probe signal is set to have frequency f_0, the signal δf and δA will be then deduced from the measured quantities $\delta\theta$ and δA^*, respectively.

due to an increase of temperature and to an absorption of energy will be exploited. The resonant frequency of a parallel LC circuit such as the one of fig. 2.2[8] is dependent on the value of the inductance in a way that it is proportional to $(L)^{1/2}$. The detection principle relies on the concept of kinetic inductance L_k, which is by definition dependent on the population of the superconducting carriers. After the absorption of energy, the increase of L_k makes the total inductance to be equal to $L^{'}$, so the fractional frequency shift is given by

$$\frac{\delta f}{f} = \frac{f^{'} - f}{f} = \frac{\sqrt{L^{'}} - \sqrt{L}}{\sqrt{L}} \simeq -\frac{1}{2}\frac{L^{'} - L}{L} \tag{2.48}$$

The last approximation holds as long as the variation in the inductance is small. The only energy-dependent component of the total inductance is the kinetic one, so introducing

[8]The resistive term can be neglected in this calculation given the exiguity of such contribution for $T \ll T_c$

the fraction of kinetic inductance α defined as

$$\alpha = \frac{L_k}{L} \tag{2.49}$$

it is possible to write the fractional frequency shift as:

$$\frac{\delta f}{f} = -\frac{1}{2}\frac{L_k}{L}\frac{\delta L_k}{L_k} = -\frac{\alpha}{2}\frac{\delta L_k}{L_k} \tag{2.50}$$

Recalling the equation 2.39 and considering that at $T = 0$ K the real conductivity and the resistance are zero, the real and the imaginary parts of the equation lead to the expressions for the change of the inductance and resistance due to a change in the complex conductivity consequent to a variation in the temperature:

$$\frac{\delta L_k}{L_k} = -\frac{\delta \sigma_2}{\sigma_2} \tag{2.51}$$

$$\frac{\delta R}{\omega L_k} = \frac{\delta \sigma_1}{\sigma_2} \tag{2.52}$$

Combining the eq. 2.51 with the eq. 2.50 the frequency shift caused by an external pair breaking can be thought as caused by a rise of the temperature to an effective value T_{eff} that would produce the same number of quasi-particles produced by the release of energy:

$$\frac{\delta f}{f} = \frac{\alpha}{2}\frac{\sigma_2(T_{\text{eff}}) - \sigma_2(0)}{\sigma_2(0)} \tag{2.53}$$

The response of the dissipative signal can be evaluated similarly. The inverse of internal quality factor of a resonator is given by:

$$Q_i^{-1} = \frac{R}{\omega L} \tag{2.54}$$

so the variation of such a quantity can be calculated as

$$\delta Q_i^{-1} = \frac{\delta R}{\omega L_k}\frac{L_k}{L} - \frac{R\delta(\omega L)}{\omega^2 L^2} \simeq \alpha\frac{\delta R}{\omega L_k} \tag{2.55}$$

where the second term was neglected since $R/\omega^2 L^2$ is small for $T \ll T_c$. Recalling the eq. 2.52 it is possible to finally write the response in the amplitude signal:

$$\delta Q_i^{-1} = \alpha \frac{\sigma_1(T_{\text{eff}}) - \sigma_1(0)}{\sigma_2(0)} \tag{2.56}$$

It can be shown that the two equations that describe the response of the resonator to a release of energy 2.53 and 2.56 can be expressed as a function of the number of quasi-particles [74][9]:

$$\frac{\delta f}{f} = \alpha\gamma S_2(\omega, T)\frac{\delta N_{qp}}{4VN_0\Delta} \tag{2.57}$$

$$Q_i^{-1} = 2\alpha\gamma S_1(\omega, T)\frac{N_{qp}}{4VN_0\Delta} \tag{2.58}$$

Here the γ is the same parameter introduced in eq. 2.39, V is the volume of the resonator, δN_{qp} is the variation of the total number of quasi-particles and S_1 and S_2 are Mattis-Bardeen parameters defined as

$$S_1(\omega, T) = \frac{2}{\pi}\sqrt{\frac{2\Delta}{\pi k_B T}}\sinh(\xi)K_0(\xi) \tag{2.59}$$

$$S_2(\omega, T) = 1 + \sqrt{\frac{2\Delta}{\pi k_B T}}\mathrm{e}^{-\xi} I_0(\xi) \tag{2.60}$$

where again $\xi = \frac{\hbar\omega}{2k_B T}$ while I_0 and K_0 are modified Bessel functions of first and second type, respectively. The number of quasi-particles N_{qp} is expressed as the product between the volume V and the density of quasi-particles n_{qp}. At a given temperature T the density of the quasi-particles due to the thermal excitations is:

$$n_{qp} = 4N_0 \int_\Delta^\infty dE \frac{E}{\sqrt{E^2 - \Delta^2}} f(E) \tag{2.61}$$

where $f(E) = \left(\mathrm{e}^{E/k_B T} + 1\right)^{-1}$ is the Fermi distribution function for quasi-particles, N_0 is the single-spin density of electron states at the Fermi energy of the material, usually of the order of $\sim 10^{10}$ $\mu\mathrm{m}^{-3}\mathrm{eV}^{-1}$ and Δ is the gap parameter. Under the assumption

[9] For simplicity only the loss due to the quasi-particles is considered here; in a more general case, one should keep into account also the dissipation associated with a possible coupling with the surrounding materials and the dissipation coming from the two-level systems of amorphous dielectric materials present on the surfaces of the superconductor. Both this contributions are not affected by the release of energy in the superconductor.

that $T \ll T_c$, the eq. 2.61 can be simplified:

$$n_{qp} \simeq 2N_0\sqrt{2\pi k_B T \Delta_0}\mathrm{e}^{-\frac{\Delta_0}{k_B T}} \tag{2.62}$$

2.2.4 Quasi-particles lifetime

The quasi-particle lifetime τ_{qp} is an important parameter that affects the expected sensitivity, since the longer the quasi-particles live the more accurate is the determination of their population. τ_{qp} is defined as the average time for a quasi-particle to find a partner to recombine with to form a Cooper pair. One can expect the process to happen on a time scale proportional to the population of the quasi-particles, meaning that τ_{qp} is shorter for high temperatures since the quasi-particle population grows exponentially as the temperature increases (eq. 2.62). If the quasi-particles are injected in a small volume resonator, a lowering of τ_{qp} could be observed due to a local increase of the quasi-particle population [77]. The same effect could be obtained if a high number of quasi-particles are injected in a superconductor with slow diffusivity, creating hot-spots of quasi-particles where the recombination happens to higher rates. The theoretical lifetime as a function of temperature are given by Kaplan [78]:

$$\tau_{qp}^{-1} = \frac{\sqrt{\pi}}{\tau_0}\left(\frac{2\Delta}{k_B T_c}\right)^{5/2}\left(\frac{T}{T_c}\right)^{1/2}\mathrm{e}^{-\Delta/k_B T_c} = \frac{n_{qp}}{\tau_0}\frac{4\Delta^2}{2N_0(k_B T_c)^3} \tag{2.63}$$

where τ_0 is a parameter that accounts for the electron-phonon coupling strength in the material considered.

2.2.5 Resonator bandwidth and down-ring time

It can be useful to relate the bandwidth of a resonator to the resonator parameters. The bandwidth (Δf) sets the ultimate promptness of the resonator to fast variations of its impedance. By reversing the definition of the quality factor, the bandwidth is given by:

$$\Delta f = \frac{f_0}{Q} \tag{2.64}$$

The minimum timescale achievable from the resonator is the down-ring time, which is defined as

$$\tau_{ring} = \frac{1}{2\pi\Delta f} = \frac{Q}{2\pi f_0} \tag{2.65}$$

In the case the measurements are performed with a double balanced mixer, as it is the case of the setup described in the next chapter, the output signal is given by a voltage, which is proportional to the square root of the power, for which reason the down-ring time with such an apparatus will account a factor of two:

$$\tau_{ring} = \frac{Q}{\pi f_0} \tag{2.66}$$

2.2.6 Intrinsic noise

In the following the source of noise that are intrinsic to the physical process of detection are described.

2.2.6.1 Generation-recombination

The noise associated with a pair breaking detector is due to the fluctuation in the quasi-particle population caused by the random process of generation and recombination of thermal quasi-particles in the superconductor. This source of noise, being caused by the fluctuation of quasi-particles, is expected to be small at low temperature, where the quasi-particle population vanishes.
Recalling the equations 2.50 and 2.51 it is possible to evaluate the power spectral density of the fractional frequency shift:

$$S_{\delta f/f} = \frac{\alpha}{2}\frac{\delta\sigma_2}{\sigma_2} = \frac{\alpha}{2}\frac{1}{\sigma_2}\frac{\partial\sigma_2}{\partial n_{qp}}S_n \tag{2.67}$$

where σ_2 can be evaluated from eq. 2.29 and S_n is the power spectral density of the number of quasi-particles, which can be show to be equal to [79]:

$$S_n = \frac{4n_{qp}\tau_{qp}}{1+(\omega\tau_{qp})^2} \tag{2.68}$$

Despite the product $n_{qp}\tau_{qp}$ remains constant over temperature, the integrated power spectral density increases exponentially with the temperature, as expected. This is

because the bandwidth of the fluctuations increases exponentially with the temperature, scaling with $1/\tau_{qp}^2$.

Similarly, recalling the expressions 2.55 and 2.52, the fluctuation of quasi-particles affects the amplitude signal with a power spectral density equal to:

$$S_{1/Q} = \alpha \frac{\partial \sigma_1}{\partial n_{qp}} \frac{1}{\sigma_2} S_n \tag{2.69}$$

2.2.6.2 Two-Level Systems

Superconducting microwave microresonators show to possess an "excess" noise that acts only on the tangential direction of the resonance circle [75, 80–82]. The source of this frequency noise is caused by two-level systems (TLS) associated with amorphous dielectric layers on the surfaces [83]. The fluctuation of these two-level systems introduces a power spectral density that varies with frequency as $f^{-1/2}$, caused by the coupling of the TLS electric dipole moments to the electric field inside the resonator. It was experimentally proved by Noroozian *et al.* that the capacitative section of the resonator is the only responsible for the TLS noise [84]. This implies that the TLS noise could be dramatically reduced by decreasing the surface layer to volume ratio of the capacitors, for instance by using interdigitated capacitors (IDC) with large spacing between their fingers.

Despite a microscopic theory of TLS noise is not yet available, the semi-empirical model by Gao *et al.* [82] describes the contribution of the TLS to the power spectral density of the fractional frequency shift as a function of the driving power P_g and temperature T, which is observed to vary as $P_g^{-1/2}$ and T^β, with β=1.5-2 [74]. It is believed that the dependence of the frequency noise on the readout power is due to the saturation of the two-level systems by the microwave electric field.

2.2.7 Amplifier noise

The signal coming from the resonators is amplified by a microwave amplifier anchored on a cold stage of the refrigerator (in the case of the work described in this thesis it is anchored on the 4 K flange), in order to keep the amplifier noise as low as possible. Despite that, among the sources of noise introduced by the instrumentation, the cold amplifier noise is by far the most important component that affects the sensitivity of

the detectors. This source of noise concerns both the inductive and dissipative signal, resulting to be isotropic in the complex representation of the S_{21}: provided an amplifier with a temperature noise of T_N, it will cause a circle-shaped noise with a radius equal to $\sqrt{k_B T_N}$. The resulting power spectral density on the phase channel will be a white noise with a level dependent on the driving power P_g:

$$\sqrt{S_\phi} = \sqrt{\frac{k_B T_N}{P_g}} \tag{2.70}$$

So the amplifier contribution on the frequency channel will be:

$$\sqrt{S_f} = \frac{\sqrt{S_\phi}}{\mathrm{d}\phi/\mathrm{d}f} = \frac{f_0}{2Q}\sqrt{\frac{k_B T_N}{P_g}} \tag{2.71}$$

In the hypothesis where the signals have a single decay constant determined by the quasi-particle recombination time, the contribution of the amplifier to the energy uncertainty will be:

$$\Delta E^{amp} = \frac{\sqrt{S_f}}{\mathrm{d}f/\mathrm{d}E}\frac{1}{\sqrt{\tau_{qp}}} = \frac{2VN_0\Delta^2}{\eta\alpha\gamma Q S_2(\omega_0, T)}\sqrt{\frac{k_B T_N}{P_g}}\frac{1}{\sqrt{\tau_{qp}}} \tag{2.72}$$

where the frequency response of the detector per unit of energy, $\mathrm{d}f/\mathrm{d}E$, is evaluated from eq. 2.57.

2.2.8 Non linearity response

In the previous sections it was shown how the signal to noise ratio would benefit from a high driving power, both for the TLS and the amplifier contributions. The driving power, however, can not be increased indefinitely without taking into account effects due to the deviation from linearity, which is a known characteristic of superconductors. As the resonator current is increased, the resonance shifts due to the nonlinearity and the behavior becomes hysteretic.

There are three potential sources of nonlinearity in thin-film superconducting resonators: 1) the nonlinearity of the kinetic inductance intrinsic to superconductivity [85, 86], 2) production of quasi-particles due to the photons of the readout [87] and 3) power-dependent current distribution [88].

For a superconductor at a temperature $T \ll T_c$ it is possible to write the kinetic inductance as a power series in terms of the current, where the odd terms are set equal to zero due to symmetry considerations:

$$L_k(I) = L_k(0) \sum_{n=0}^{\infty} \left(\frac{I}{I^*_{2n}} \right)^{2n} \tag{2.73}$$

Here $L_k(0)$ is the kinetic inductance in the low power limit and I^*_{2n} sets the scaling of the effect. Arresting the expansion to the quadratic term, I^*_2 is expected to be of the order of the critical current: this parameter can be seen as the current at which the kinetic energy of the supercurrent equals the superconducting condensation energy. The kinetic energy per unit length is $\mathcal{L}_k I^2$, where $\mathcal{L}_k$ is the kinetic inductance per unit length, while the condensation energy per unit length is $2N_0\Delta\mathcal{S}$, where $\mathcal{S}$ is the cross sectional area of the superconducting traces. Equating the two expressions it is possible to calculate I^*_2:

$$I^* = \Delta \sqrt{\frac{2N_0\mathcal{S}}{\mathcal{L}_k}} \tag{2.74}$$

It can be shown that the maximum driving power before the resonance behaves hysteretically is related to the quality factor through [89]:

$$P^*_g = \frac{1.54\omega_0 L_{res} \left(I^*\right)^2}{\chi_c Q^2} \tag{2.75}$$

where χ_c is an efficiency factor with values between 0 and 1 that accounts for the coupling of the resonator to the feedline:

$$\chi_c = \frac{4Q^2}{Q_i Q_c} \tag{2.76}$$

Considering a nonlinear inductance, the frequency will shift downwards of an amount δf^*, leading to a shifted detuning that can be evaluated at the first order as:

$$x^* = \frac{f - f_0 - \delta f^*}{f_0 + \delta f^*} \approx x - \frac{\delta f^*}{f_0} \equiv x - \delta x^* \tag{2.77}$$

where it can be easily shown how the quadratic term of eq. 2.73 affects the nonlinear detuning:

$$\delta x^* = \frac{\delta f^*}{f_0} = -\frac{\alpha}{2}\frac{\delta L^*_k}{L_k} = -\frac{\alpha}{2}\left(\frac{I}{I^*_2}\right)^2 \tag{2.78}$$

For high enough driving powers, the nonlinearity will eventually bring to the observation of the bifurcation [89]: in the case the generator frequency is increased starting from frequencies below the resonance, the resonator current increases as the frequency approaches the resonance condition, and the nonlinear inductance causes the resonance to shift downward. The results is that the detuning is additionally reduced, eventually resulting in a positive feedback condition, where the resonator "snaps" into the energized state. On the other hand, if the frequency is decreased starting from frequencies above the resonance, a negative feedback condition will establish, where the resonance shifts downwards as the generator tone chases the resonance, until sweeping past the resonance minimum when the resonator suddenly snaps back to its non-energized state. Since the effect of nonlinearity that was just described is only due to the inductance, the resonance depth is expected to remain constant.
In other cases the vortex penetration could make the dissipation another important nonlinearity source, where the effect would increase with the stored energy [90]; in such a case, the resonance depth will decrease for higher powers. Finally, in the cases where superconductors with relatively low quality factors are involved or temperatures where the population of quasi-particles is not negligible are considered, also quasi-particles can provide an important mechanism for nonlinearity [91].

2.2.9 Frequency multiplex

One of the very attractive qualities that can make the microresonators technology a competitive solution in many fields is their capability to be easily multiplexed: provided that the transmission faraway from the resonant frequency is equal to the unity, this technology lends well itself to the frequency domain multiplex. By coupling many resonators with resonant frequencies designed to be slightly different from each other to a feedline (fig. 2.6), it is possible to readout a large number of detectors with a single line, in a number that is limited only by the bandwidth of the commercially available digitizers. The resonances must be well separated in frequency so that the tails of two resonance do not overlap, hence the frequency spacing should be a quantity equal to several times the bandwidth of the resonances. Besides, in order to prevent overlaps, the separation of the resonances should be designed keeping into account the accuracy of fabrication, which translates into uncertainty in the resonance characteristics.

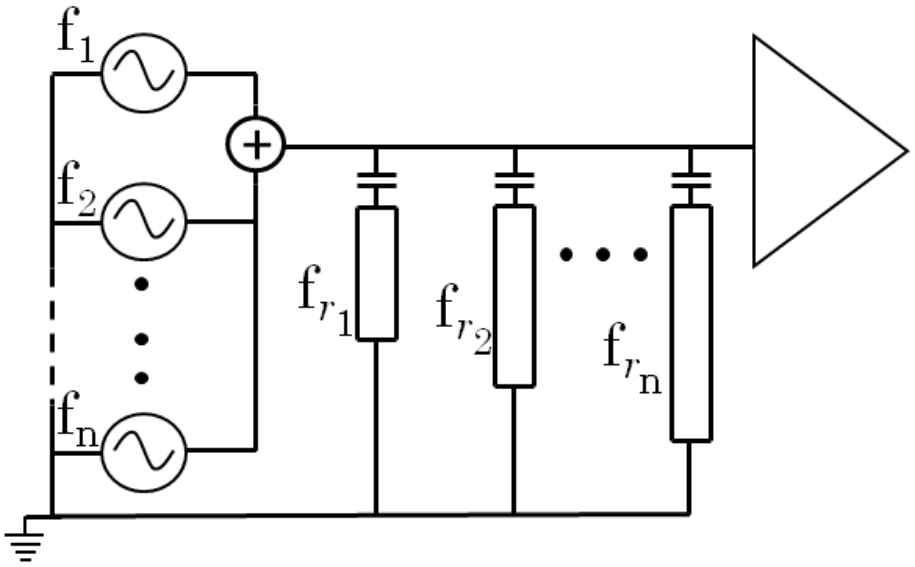

FIGURE 2.6: Multiplex scheme: each resonator is probed by a tone with frequency f_i as close as possible to the steady state resonant frequency f_{r_i} in order to get the highest signal as possible.

Chapter 3

Setup

The MKIDs described in the literature used for bolometric applications can be grouped into three main categories [92]: quarter-wave coplanar waveguide (CPW) resonators, lumped-element resonators (LEKIDs) and inter-digitated capacitor resonators (IDC). All these geometries consist of a thin layer of superconducting ground plane deposited on a substrate, usually made of silicon or sapphire. A feedline, usually a coplanar waveguide, runs across the ground plane and it is coupled to coaxial cables to each end, through which the resonator is probed. The resonators are weakly coupled to the feedline, and they are designed to resonate at an unique characteristic frequency. By coupling many resonators to the same feedline it is possible to perform the readout of multiple detectors using a single readout line. The limitation on the theoretical achievable multiplex factor is only set by the bandwidth of the RF electronics available.

In order to apply the MKIDs technology to the neutrino mass measurement, the detectors must be single particle detectors, with good energy and time resolution and with response not dependent on the position of the interaction. The energy resolution is achieved by maximizing the fraction of kinetic inductance α and the gap parameter Δ. The first of the two parameters can be enhanced by using superconductors with high surface inductivity (i.e. high normal resistivity) combined with a very small thickness, which is preferable to be smaller than the penetration length. On the other hand, the thickness of the film must be enough to contain the electrons coming from the decay of the holmium. In the BCS limit the gap is increased by decreasing the critical temperature. Nevertheless the T_c can not be decreased indefinitely because with extremely low

critical temperatures the photons of the probe signal would give a significant contribution to the breaking of the Cooper pairs.

CPW MKIDs Among the possible designs, coplanar waveguide resonators are the simplest ones (fig. 3.1). A special subset of CPW resonators is composed by quarter-wave resonators which are open-circuited at the coupling end (where a Dirichlet boundary condition is created, i.e. the current is zero) and are short-circuited to the ground plane at the far end (von Neumann boundary condition, i.e. the current is constant), which allows only the odd harmonics of the resonant frequency to couple to the resonator. The resonant frequency is determined by the length of the resonator, the dielectric constant of the substrate and the fraction of kinetic inductance. The coupling to the readout feedline is obtained with an elbow coupler, where the coupling strength is set by the length of the coupling portion and by the distance from the feedline. The sensitivity of the detector is weighted by the current distribution, which is one quarter of a sine wave over the length of the resonator, reaching the maximum value at the shorted end, while the sensitivity is small at the coupling end, where the current is zero.

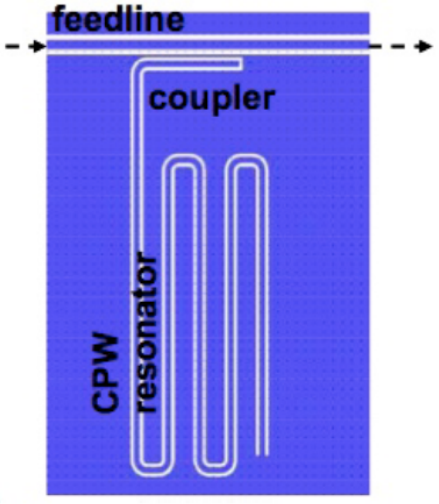

FIGURE 3.1: Example of a CPW resonator.

The main drawback of this design is related to its high frequency noise, caused by the small geometric size of the capacitive portion.

LEKIDs The lumped-element resonators (3.2) are composed by an inductive portion coupled to an inter-digitated capacitor. In this configuration the inductor can be used

as direct absorber for the radiation to be detected.

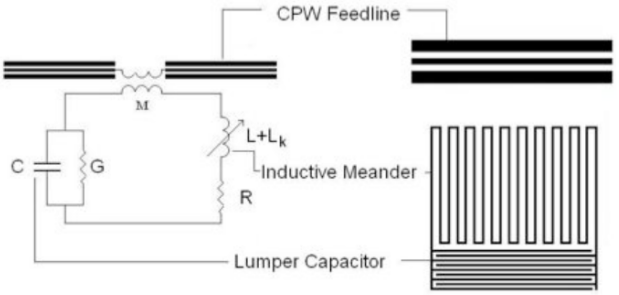

FIGURE 3.2: Example of a LEKID.

A potential disadvantage could be represented by their large size, which could bring to non negligible cross coupling effects when a large number of detectors close to each other are required.

IDC resonators The Inter-Digitated Capacitor (IDC) resonators (fig. 3.3) are hybrids of lumped element and quarter-wave resonators: while the inductive portion is a CPW shorted at one end, as in quarter wave detectors, the capacitor is composed by a large inter-digitated capacitor, like in the lumped-element detectors. Since in this design the capacitance comes from a large fingered structure, the surface to volume ratio results suppressed, reducing in this way the TLS noise. Differently from CPWs, the resonant frequency is not set by the length of the resonator, making less trivial the current distribution and the coupling to the harmonics of the resonant frequency. In this situation the strength of the coupling is determined by the distance of the capacitor from the feedline.
The main advantage of this design is the reduction of the noise compared to a CPW resonator. On the other hand, the principal disadvantage of this detectors consists in the potential inter-resonator coupling, especially in close-packed arrays, due to their large size.

3.1 Design of KIDs for a neutrino mass experiment

The work described in this thesis is performed with different designs and materials that will be described below. The devices will be cataloged accordingly to the number of

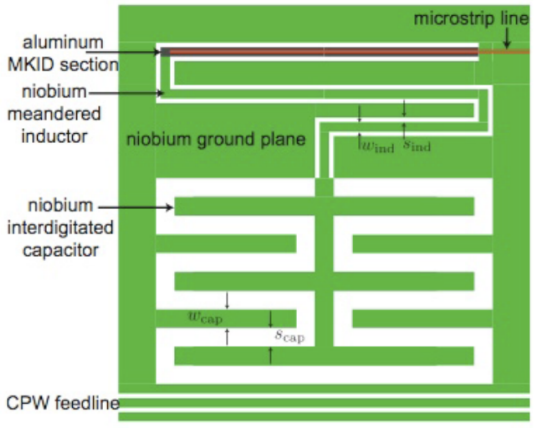

FIGURE 3.3: Example of an IDC resonator.

their production run, made at the Fondazione Bruno Kessler (FBK) in Trento, Italy. The aim is to adapt and optimize the existing technology of the superconducting microwave microresonators to develop arrays of single-particle detectors applicable to the calorimetric measurement of the energy spectrum of ^{163}Ho [93]. The approach consists in embedding the holmium directly into the inductive part of a lumped-element resonator, so as not to rely on diffusion and trapping of quasi-particles or other potentially lossy means of transferring the energy of the decay into the quasi-particle system of the superconducting film used as the sensor. It is possible to adjust the density of the holmium in order to produce a desired counting rate. Given the relatively short half life of holmium, only 3×10^{12} ^{163}Ho nuclei are needed for a counting rate of 10 Hz. Considering an hypothetical implanted area of 3 μm $\times$ 500 μm, only 2×10^{17} atoms/cm^2 are needed. This configuration requires the resonator current to be very uniform over the length of the inductor along which the holmium is embedded to ensure that the position dependent response of the detector does not degrade the energy resolution. For this reason the length of the inductor will be designed to be very much shorter than the wavelength corresponding to the resonant frequency. Prior to the ^{163}Ho implantation, a full characterization using low energy X-ray sources to irradiate the sensitive area is mandatory.

The materials considered consisted of titanium nitride (TiN) with different stoichiometric ratios for each run. The nitrides, especially TiN, possess promising qualities that could potentially improve the sensitivity for most applications where microresonator detectors are employed: the quality factors achievable with TiN resonators can be made as high as 3×10^7 [94], about 10 times higher than other metals that have been investigated

by the community. It can be shown [94] that a figure of merit for microresonator detectors is given by $F = \alpha\tau_{\max}Q_{i,\max}/N_0V$, where α is the fraction of kinetic inductance, $\tau_{\max}$ is the quasi-particle lifetime under low drive power, $Q_{i,\max}$ is the corresponding internal Q, N_0 is the density of states at the Fermi level and V is the volume of the detector. The energy sensitivity limit set by the amplifier δE_{amp} is then proportional to $F^{-1/2}$, meaning that TiN should improve of an order of magnitude δE_{amp} respect the other materials that have been used so far. Another advantage in using TiN relies in its large normal state resistance, typically in the range of 40-100 $\mu\Omega$·cm. From the Mattis-Bardeen theory the relationship between the normal state resistance and the surface inductance is known [95] to be $L_s = \hbar R_s/\pi\Delta$, so the higher the sheet resistance the larger is the surface inductance, allowing to project structures characterized by high ratio of kinetic inductance to total inductance, α. Another advantage of the nitrides is the possibility to tune the critical temperature, and hence the gap energy and recombination time, by varying the stoichiometric ratio between nitrogen and titanium in the films to get the wanted characteristics for a particular application.
As mentioned previously, the fundamental noise of a pair-breaking detector for phonon counting applications is set by the statistics of the energy cascade process that produces quasi-particles and low energy phonons. For example, assuming a typical conversion efficiency of 0.5 and a T_c of the sensor material to be 1 K, a 2 keV decay event produces a number of quasi-particles of about $N_{qp} = 6 \times 10^6$, implying an energy resolution of $\Delta E \sim 2\ \text{keV}/N_{qp}^{1/2} \sim 0.8$ eV. The theoretical energy resolution should actually be slightly better than this value because of the Fano factor since $f < 1$.

3.1.1 Materials

Different films of titanium nitride were produced and tested, with two different approaches: the substoichiometric and the multilayer technique. A stoichiometric film of TiN was also tested as reference.

3.1.1.1 Sub-stoichiometric films

In order to optimize the signal to noise ratio, different films of titanium nitride have been considered. In particular, by decreasing the concentration of the nitrogen constituting the film, it is possible to reduce the critical temperature, assuring a larger number of

quasi-particles created per eV. Besides, by decreasing the critical temperature, it is possible to increase the quasi-particle lifetime, affecting positively the contribution to the energy uncertainty given by the amplifier (see eq. 2.72)

The first attempt was to produce sub-stoichiometric TiN_x films with the MRC Eclipse reactive sputtering system present in the clean room at FBK in order to investigate the dependence of the superconducting transition temperature on the x parameter [94]. The films were produced in the fabrication facilities of Fondazione Bruno Kessler (FBK). They were deposited in a mixture of Ar-N_2 gas from a pure Ti target. It was observed that for the concentrations of nitrogen explored (N_2 flow rate between 45 sccm and 5 sccm[1]), the critical temperatures T_c of the films were either close to 4.5 K or not observed at all. Auger Electron Spectroscopy (AES) was performed in FBK, providing detailed information on the elemental composition of the materials and on the chemical states of the surface atoms. The measurements have shown a nearly stoichiometric composition of the TiN_x in the range $(30 \div 45)$ sccm (figure 3.4). In the case of the three samples with

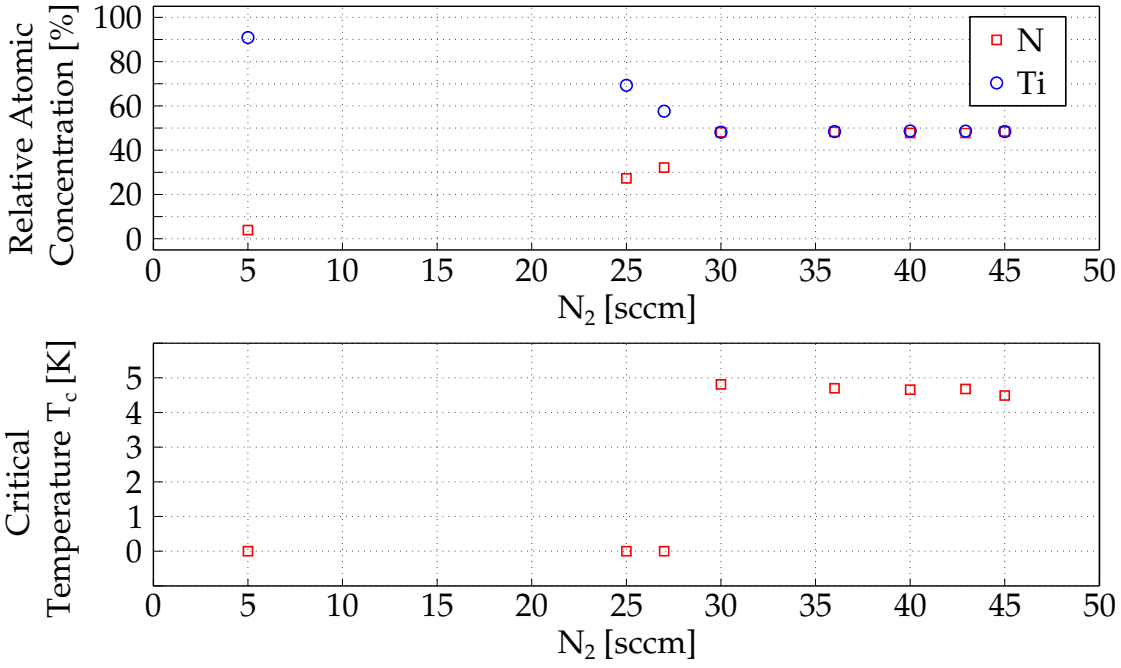

FIGURE 3.4: Top: Titanium and Nitrogen relative atomic concentration of the TiN_x samples as a function of the N_2 flow rate. The atomic concentration ratios are very close to the stoichiometric value, except for N_2 flow rates of 5, 25 and 27 sccm, where values of respectively 0.56, 0.39 and 0.04 are achieved. Bottom: the critical temperatures of the TiN_x samples as a function of the N_2 flow rate. The values are close to 4.5 K for films produced with a N_2 flow rate between 30 and 45 sccm, while no transitions were observed below 30 sccm.

flow rates of 5, 25 and 27 sccm the concentration ratios differed from the stoichiometric

[1]Standard Cubic Centimeters per Minute.

value, but the transition was not observed at all. Indeed the chemical compositions of the 25 and 27 sccm samples were in fact very similar to that of Ti_2N, which is not a superconductor; the sample obtained with 5 sccm has a composition very close to the pure Ti. This results are mainly due to the impossibility to control the concentration of nitrogen by controlling the N_2 flow rate with enough accuracy in order to be able to be sensible in the very narrow range over which the critical temperature is tuned.
Nevertheless, devices with substoichiometric film with the same geometry of the ones produced by FBK were provided by JPL as courtesy of Henry Leduc, with a thickness of 160 nm.

3.1.2 Proximity effect and the multilayer technique

In the previous section the technical challenges to tune the critical temperature of a TiN film were described. In addition to those, the substoichiometric films show large non-uniformity across the wafer [96, 97]. As a solution, the multilayer technique was adopted instead. It consists in exploiting the proximity effect [98] of two superconductors with different critical temperatures that will behave like a "mixture" of the two, making possible to tune the wanted T_c by adjusting the thickness of the two metals [99]. The non-locality of superconductivity makes the T_c of multi-layer thin films dependent not only on the properties of the superconductors that constitute the film, but also on the interaction between the layers. Cooper provided an early description [100] of the proximity effect for a bilayer composed by a normal metal and a superconductor where the thicknesses of the two layers were less than any relevant length scale. In the case of multilayers the T_c is determined by the thicknesses of the composing materials [99, 101, 102].
The multilayer devices were produced at FBK by superposing a number (maximum 8) of Ti/TiN bilayers choosing the Ti to be the first material to be deposited on the substrate and TiN always on the top. The films have been sputtered on high resistivity Silicon wafers previously cleaned and etched with hydrofluoric acid (HF) in order to remove the native oxide. The films were deposited at the temperature of 400°C and the thicknesses of the layers were obtained by changing the the deposition time and rate [103].
In order to measure the critical temperature, the electrical resistances of the films were measured with the 4-wires technique at the Cryogenics Laboratory of the University of

Trento, with a dilution refrigerator (Janis JDry-100-ASTRA) capable of a base temperature of 17 mK. In the figure 3.5 the critical temperature as a function of the layer

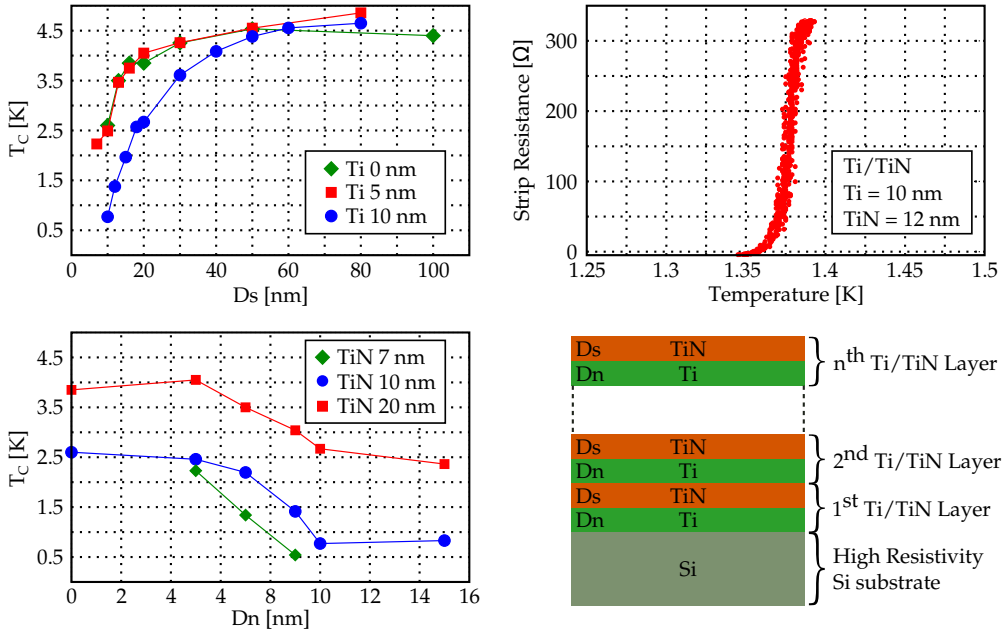

FIGURE 3.5: The left plots show the measured T_c of the Ti/TiN multilayers as function of TiN (top-left) and Ti (bottom-left) thicknesses. In the bottom-right the schematic of the multilayers is reported. The transitions are sharp, with a width of $\simeq$30 mK, as shown in the top-right figure, where data from multilayer Ti/TiN (10nm/12nm) are illustrated.

thicknesses is reported. This results show that it is possible to tune the superconductive transition to be in the (0.5 ÷ 4.6) K temperature range by properly choosing the Ti thickness in the (0 ÷ 15) nm range, and the TiN thickness in the (7 ÷ 100) nm range. It was observed that by reducing the TiN thickness and keeping the Ti one fixed it is possible to lower the T_c. Alternatively it is also possible to fix the thickness of TiN layers and to increase the thickness of Ti. In order to check the uniformity, the T_c was measured across the wafer on different slices cut from the edge and from the center and it was found that the critical temperature varied by no more than 1%. In the case of TiN_x the same check provided evidences of variations up to 20% [103]. These evidences are compatible with the measurements by Vissers *et al* [99].

3.1.3 Production run 1

The first production run was made with stoichiometric TiN, and the geometry is shown in fig. 3.6. It consists of two inter-digitated capacitors connected by a coplanar strips (CPS)

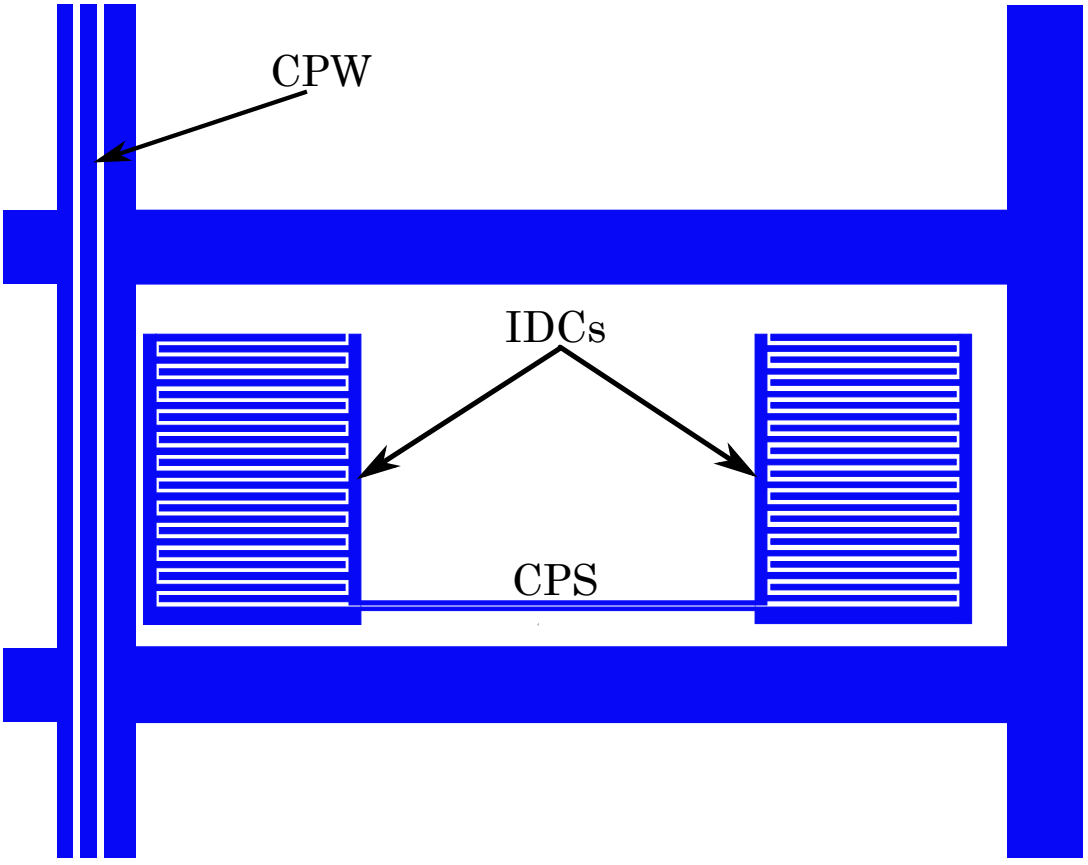

FIGURE 3.6: Geometry of one resonator produced in the production run 1. The resonator is composed of an inductor made by a coplanar strip (CPS), which connects two interdigitated capacitors (IDCs), one of which is capacitively coupled to the CPW feedline. The strength of the coupling is set by the gap between the capacitor and the feedline.

transmission line which works as inductor of the circuit. The resonator is capacitively coupled on one side to a coplanar waveguide (CPW) line that is used for the readout. The strength of the coupling, which sets the coupling quality factor Q_c, is determined by the width of the gap between the CPW line and the resonator. The spacing and width of the conductors of the IDCs is between 10 and 30 μm: this large spacing is intended to reduce the two-level systems (TLS) noise by decreasing the surface to volume ratio of the capacitors [84]. The sections of ground plane above and below the resonator are intended to reduce coupling to the neighboring resonators. Maintaining the general design, four different geometries were designed with two IDCs dimensions (10 μm and

30 μm) and two CPS separation widths (5 μm and 10 μm).

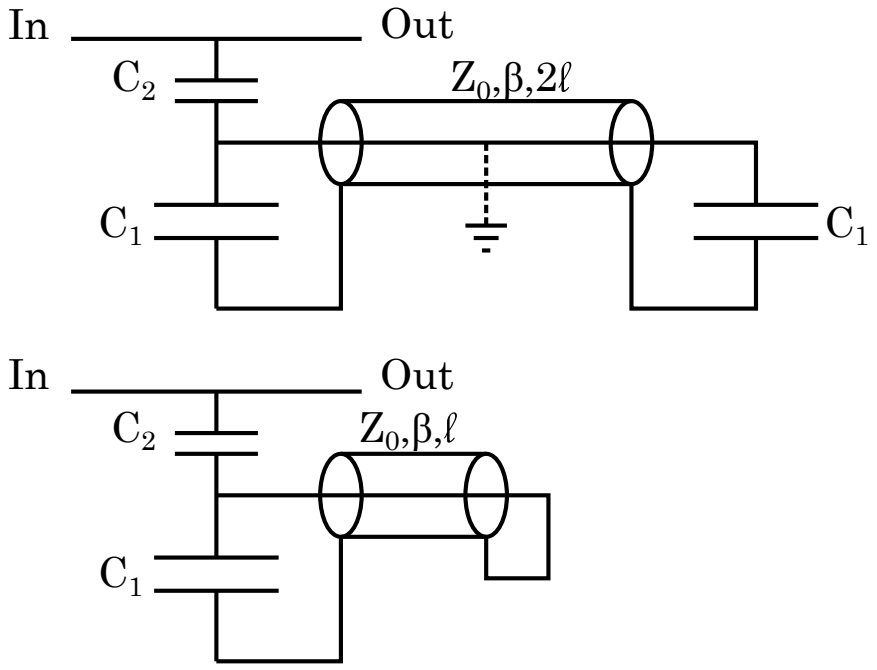

FIGURE 3.7: Circuit model of the resonator (*top*) with the simplified circuit considering a virtual ground in the middle of the inductor (*bottom*).

The circuit model of the resonator (fig. 3.7) features two capacitors (each with the same capacitance C_1) across either end of a transmission line of characteristic impedance Z_0, length 2ℓ, and propagation constant $\beta = \omega/v_{ph}$, where v_{ph} is the propagation velocity. The resonator made by these three elements is coupled on one end to the readout line through the capacitance $C_2 \ll C_1$. In the situation where C_2 is negligible, by symmetry there is a virtual ground at the center of the transmission line, so it is possible to consider a simplified circuit consisting of a capacitor in parallel with a shorted line of length ℓ. Resonance occurs when the impedance $Z_C = 1/i\omega C_1$ equals the negative of the input impedance of the shorted transmission line section $Z_{in} = jZ_0\tan\beta$. At this frequency, the parallel combination of these impedances becomes large enough to tune out the large impedance of the small coupling capacitor, producing a short across the readout line, resulting in a dip in its transmission.

For each geometry two films with thickness of 120 nm and 250 nm were produced. Every chip features 16 resonators disposed in two rows (fig. 3.8).

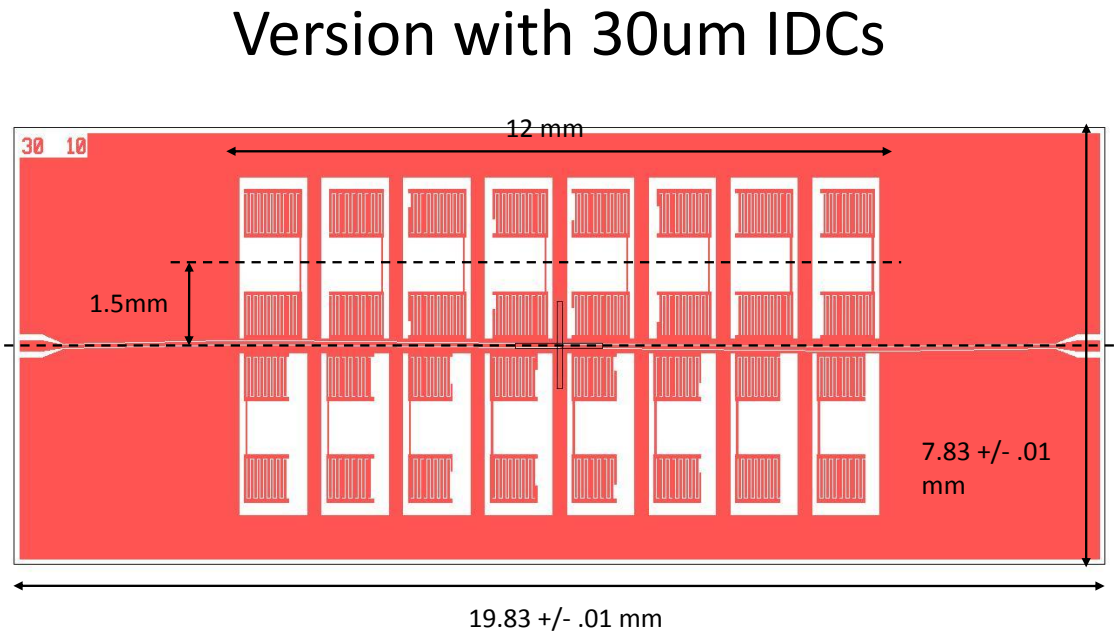

FIGURE 3.8: One chip produced in the run 1: 16 resonators are present disposed on two rows.

3.1.4 Production run 1.5

In this run the geometry was kept the same as in the first run, choosing as superconducting material two multilayer films with different critical temperatures: the first one using a Ti thickness of 10 nm and a TiN thickness of 12 nm (total thickness 176 nm) and a second film with thicknesses of 10 nm and 15 nm (total thickness 200 nm).
In addition a substoichiometric film was provided by JPL for comparison.

3.1.5 Production run 2

Within the second production run two main different geometries were designed and produced: devices with a revisited geometry respect to the first run (in the following referred as "geometry A") and devices to be coupled to an absorber ("geometry B").

3.1.5.1 Geometry A

The detector array chips are designed with individual microresonator frequencies distributed in the $(4 \div 6)$ GHz range. The resonator geometry is in the lumped element form, and it was produced with two configurations: the standard one and a modified version where the substrate below the inductor was etched away (figure 3.9). The

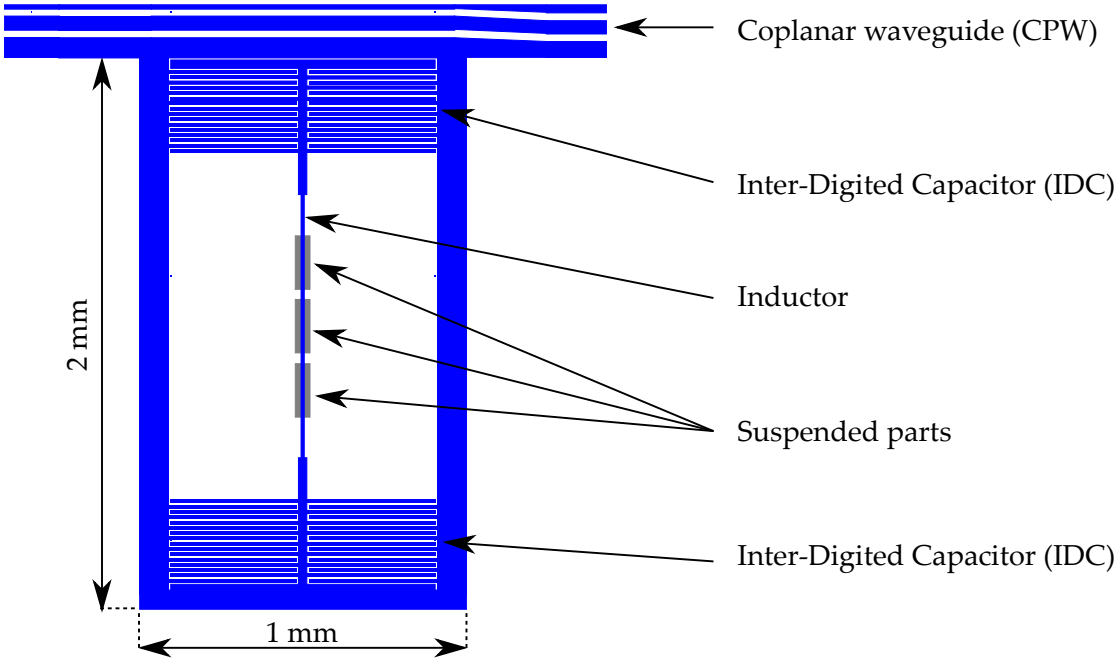

FIGURE 3.9: Design of a single resonator produced in the second run of production. It was not possible to remove the substrate under the full length of the inductor, so a discrete solution was adopted instead.

resonator consists of two interdigitated capacitors (IDC) connected with a CPW that works as inductor. As in the geometry of run 1, the resonator is capacitively coupled to a coplanar waveguide (CPW) used as feedline and for the readout. The spacing and width of the conductors of the IDCs and the width of the inductor are 10 μm, in order to be optimized to minimize the TLS noise. In the version of the resonator with the inductors suspended from the substrate, the design features three openings under the central conductor creating a suspended inductor in order to prevent the exchange of phonons between the film and the Si-substrate. The solution with the three openings was adopted instead of a single gap running for the entire length of the inductor for reasons related to the elongation of the inductor: this, without supports, would have bend to lay on the bottom of the gaps.

[2]Image from a paper in preparation. Courtesy of A. Giachero.

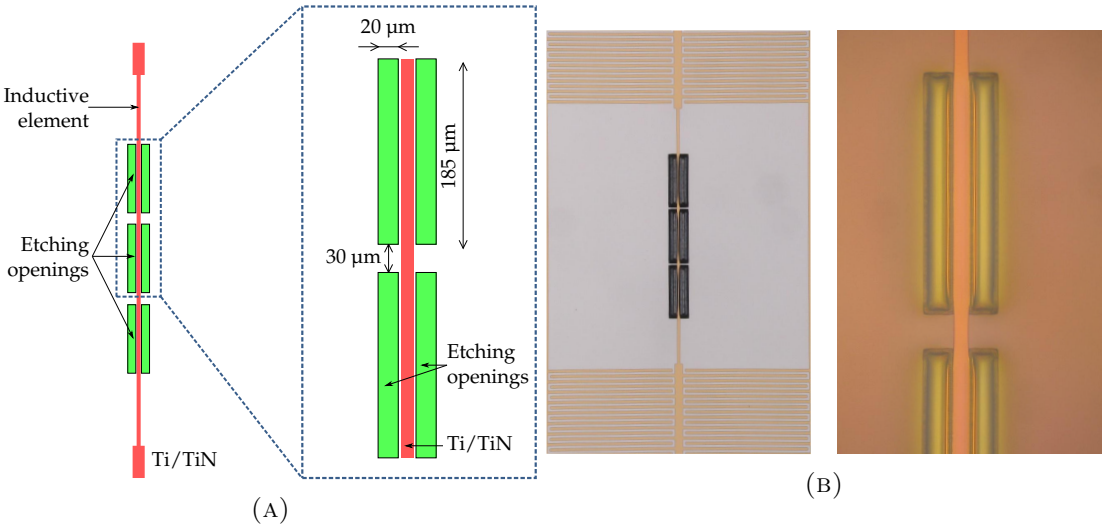

FIGURE 3.10: (A) Sketch [2]and (B) pictures of the openings.

The film chosen for this geometry is composed of 9 bilayers of Ti/TiN using a Ti thickness of 10 nm and a TiN thickness of 12 nm, for a total thickness of 198 nm. Multilayers have been deposited at a temperature of 400°C by MRC Eclipse reactive sputtering system on high resistivity Silicon <100> wafers. Wafers have the native oxide removed immediately before the film deposition by dipping them for 7 seconds in a hydrofluoric acid solution (HF8%). A metalization composed of 500 nm of Aluminum (Al 1% Si) was deposited on the back side of the wafers to create the ground plane and to properly decouple the resonator from the copper older used in the experimental setup. To suspend the inductive lines from the substrate, they were etched from the top side with a Deep Reactive-Ion Etching (DRIE) using an isotropic recipe creating the three openings in the silicon (figures 3.10a and 3.10b), protecting the metal layer with a 3000 μm of photoresist. This protection layer was next patterned with a light mask to obtain openings near right-hand side and left-hand side of inductive line. Finally, the protection layer was removed by plasma etching. Some resonators were kept with the inductor in full contact with the substrate, in order to be able to make a comparison between the two situations.

3.1.5.2 Geometry B

The "B" geometry consists of a device with geometry similar to the "A" geometry, except that an absorber is deposited above the middle part of the inductor.

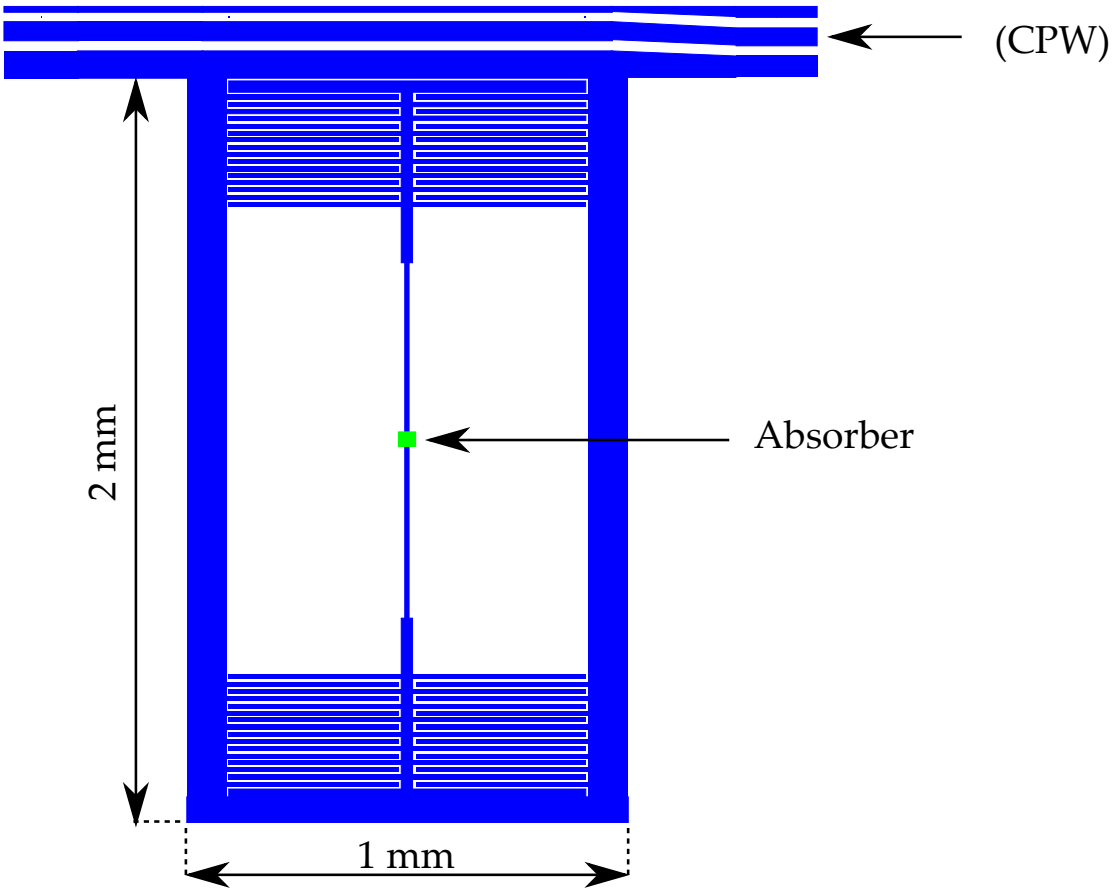

FIGURE 3.11: Design of a single resonator of the geometry "B". The green square represents the absorber deposited onto the inductor.

It is required that the absorber is a superconductor with a gap greater that the gap of the material constituting the resonator in order to exploit the quasi-particle trapping effect [104]: in this way the interaction will take place inside the relatively large volume of the absorber creating quasi-particles that will diffuse and then will be "trapped" in the lower gap superconductor giving rise to a response proportional to the energy released. The solution with an absorber was designed for two main reasons: on one hand implanting the isotope in an absorber will avoid potential problems regarding the effects on the resonance due to the implantation of the holmium in the inductor[3], while on the other hand by choosing a superconductor with faster diffusion then TiN the energy response of the detector will not be affected by local saturation of quasi-particles due to the low diffusivity characteristic of TiN.

The deposition of an absorber made of tantalum encountered technical challenges; the

[3]Having a thick absorber will also increase the efficiency of detection of the X-rays during the test stage.

test performed at FBK provided absorbers with poor residual resistivity ratios or reduced critical temperature. This was probably due to the formation of silicide during the deposition process. These devices are being produced with the deposition of tantalum 200 and 500 nm thick by STAR cryoelectronics on TiN resonators deposited by FBK and will be tested in the near future as soon as the fabrication process will be complete.

3.2 Experimental setup

The RF characterization was performed by mounting the arrays in a copper holder (fig. 3.12) anchored on the mixing chamber of a liquid helium dilution fridge (Oxford MX 40, fig. 3.13, testbed at the Cryogenics Laboratory of the University of Milano-Bicocca) which provides a cooling power of 40 μW at 100 mK and a base temperature of 25 mK. A schematic of the cryogenic system is shown in figure 3.15.

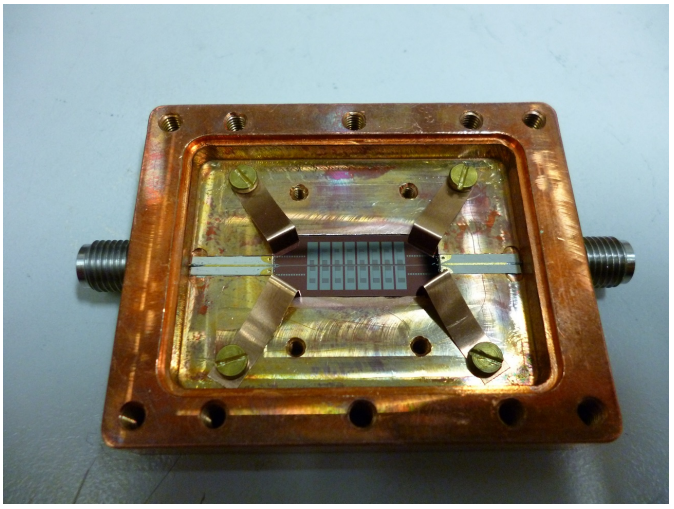

FIGURE 3.12: The copper holder with a chip mounted and kept in position by four Cu-Be springs. The RF signal is brought to the CPW of the chip through K connectors soldered to a waveguide lying on a Duroid board.

The RF signal is transmitted from the room temperature to 4 K by Cu-Be coaxial cables, ensuring a low thermal load on the liquid bath. On the input line between the 4 K stage and the mixing chamber stainless steel coaxial cables are employed to ensure a thermal load on the mixing chamber as low as possible. In order to preserve the signal coming from the detectors avoiding dissipations, the output line from the detectors to the HEMT (High Electron Mobility Transistor) amplifier placed at 4 K (fig. 3.14) is composed by superconducting niobium coaxial cables. On the 4 K stage and on the mixing chamber

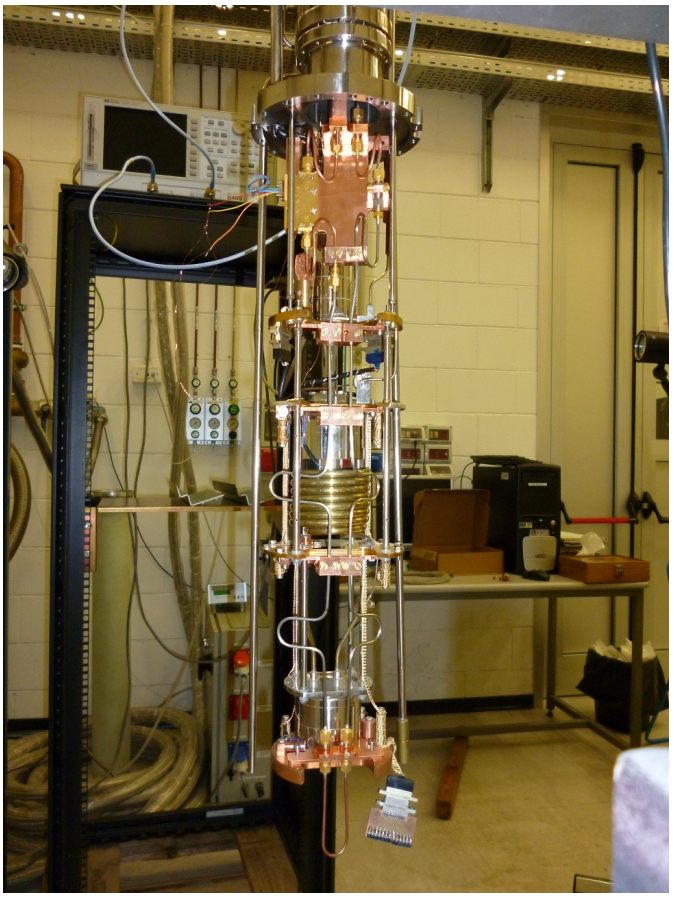

FIGURE 3.13: The MX 40 by Oxford dilution unit used for the measurements.

two discrete attenuator of -20 dB were installed with the aim to attenuate the thermal noise coming from the 300 K to match the temperature at which the detectors are. In addition, at 300 K on the input and output lines two DC blocks are used to filter low frequency noise.

The setup used to readout the detectors is depicted in the figure 3.15, while the specific RF circuit installed to readout two resonators at the same time is reported in figure 3.16 and in the picture 3.18. The technique used to readout two microresonator at the same time exploits the homodyne detection method (B), as reported in [75]. The microwave signals used to probe the resonators are generated by two synthesizers with a power of +15 dBm. Each signal is split by means of a directional coupler: one copy is used as local oscillator (LO) of the IQ mixer used for the demodulation, while the other copy is attenuated of -20 dB and combined with the signal coming from the second synthesizer by a Wilkinson power divider. The so obtained signal is transmitted inside the cryostat to the microresonator chip. The transmitted signal is then amplified of a factor $\sim +36$ dB by the HEMT amplifier and sent out of the cryostat. Here the signal is further

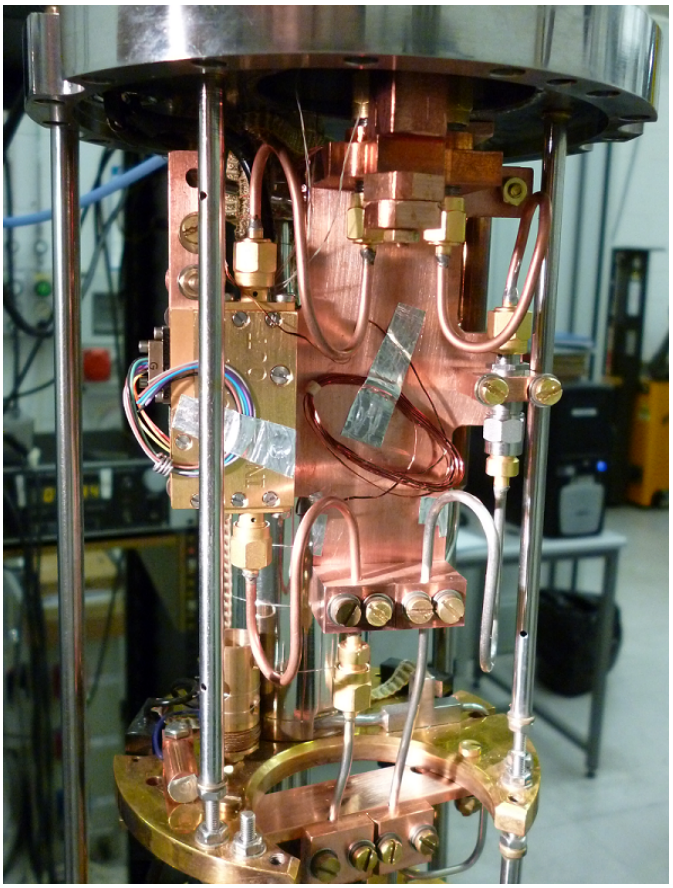

FIGURE 3.14: The HEMT amplifier anchored on the 4 K stage (left). On the right it is possible to see one discrete attenuator mounted on the input line.

amplified by a room temperature amplifier (gain $\sim$ +26 dB), split in two by another power divider and sent to the RF ports of the IQ mixers. The mixers outputs I and Q are acquired and digitalized using a commercial NI-PXIe 8375 board with a 2.5 MHz sampling rate.

In order to test the detectors response to the release of energy, the devices were illuminated with two low energy X-ray sources placed on the top of the detectors (fig. 3.17): ^{55}Fe ($\sim$ 6 keV) and fluorescence of Al (k_α fluorescence line at 1.5 keV) obtained by illuminating an aluminum foil placed on top of the detectors with a primary source of ^{241}Am ($E_\alpha \sim 5.5$ MeV). The X-rays have been collimated by an aluminum collimator, in order to avoid interactions in the IDCs, where the current is not exactly zero, and to focus the events on a small area to ensure uniformity of response. By acquiring the I and Q coming from the two mixers it was possible to determine the energy estimator

[4]Image from a paper in preparation. Courtesy of A. Giachero.

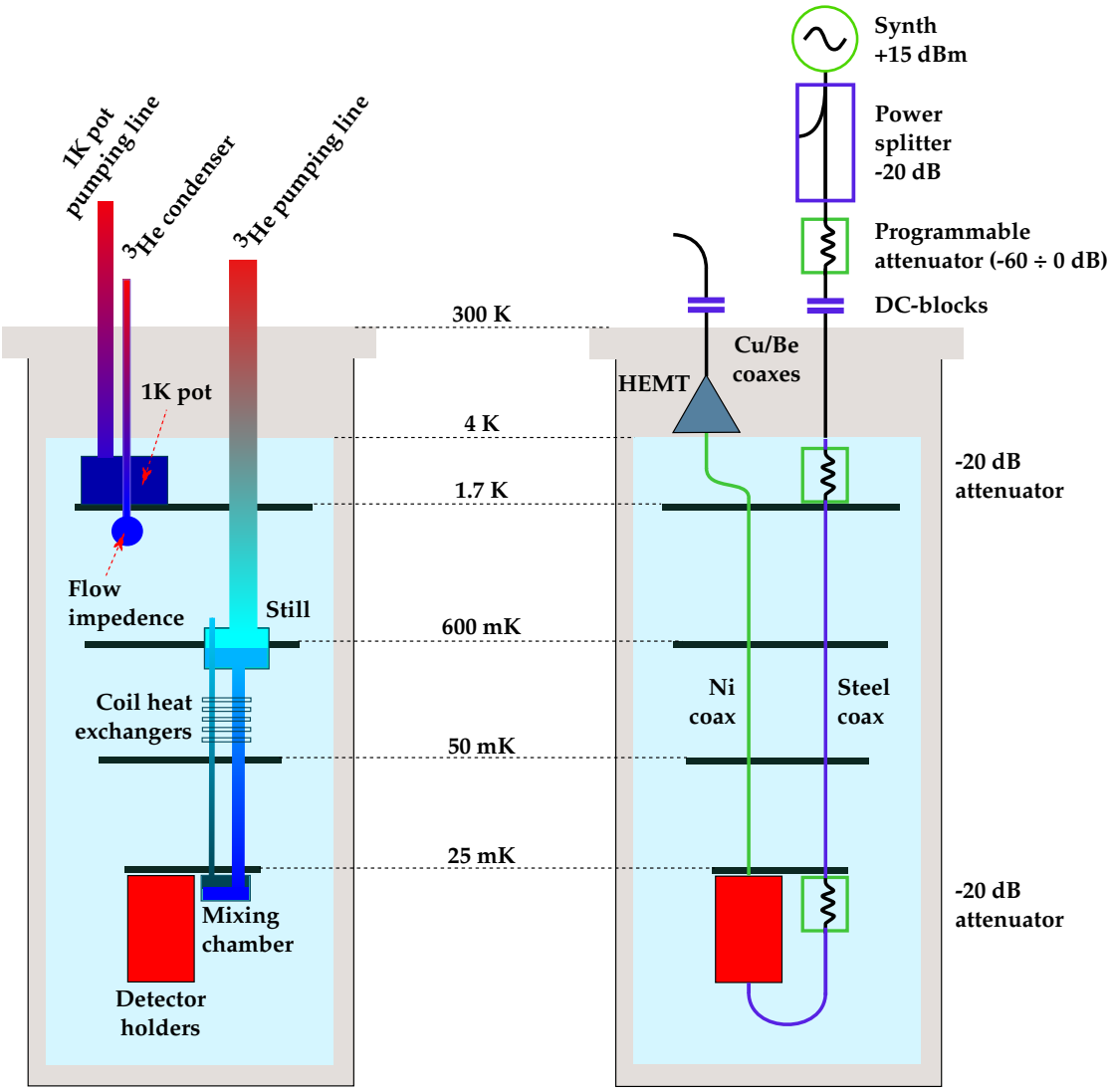

FIGURE 3.15: (Left) Sketch of the cryogenics system[4]. The mixing chamber temperature can be tuned within the (20 ÷ 1000) mK. (Right) Schematic of the RF internal coaxials and experimental system.

of these detectors, i.e. the frequency shift due to the interaction of the X-rays with the resonators.

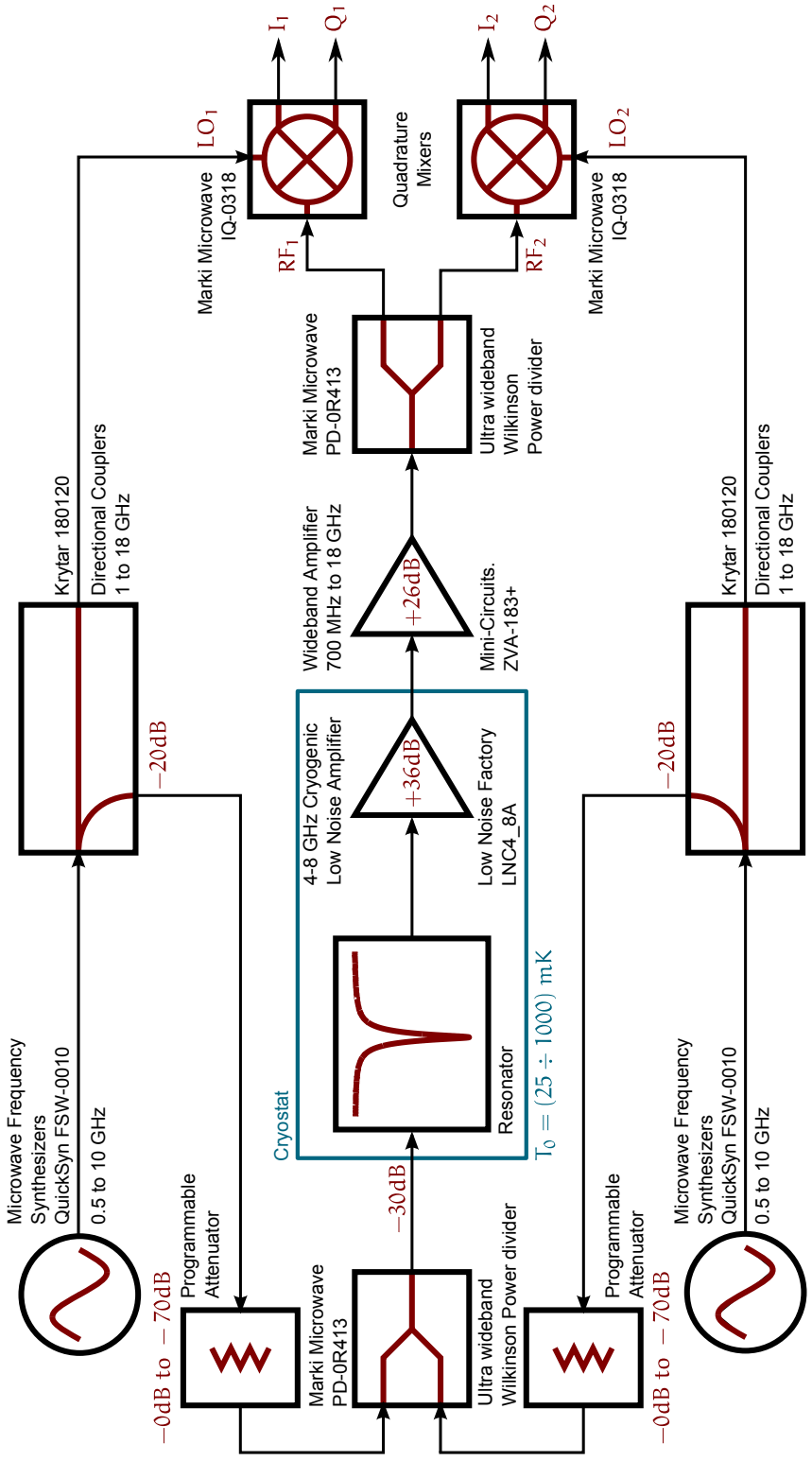

FIGURE 3.16: The 2-channel homodyne detection scheme employed for the readout. Two low-phase noise microwave synthesizers generates the fixed-frequency signals used to excite two different microresonators. A Wilkinson power divider used in the opposite direction combines the generated signals in the same feedline the resulting signals is sent into the cryostat at the microresonator array. After transmission through the device, the signal is amplified by a low noise cryogenic HEMT amplifier and a room-temperature amplifier. Two IQ (inphase-quadrature) mixers are used to measure the dissipation and frequency shifts of the transmitted signal as a function of time.

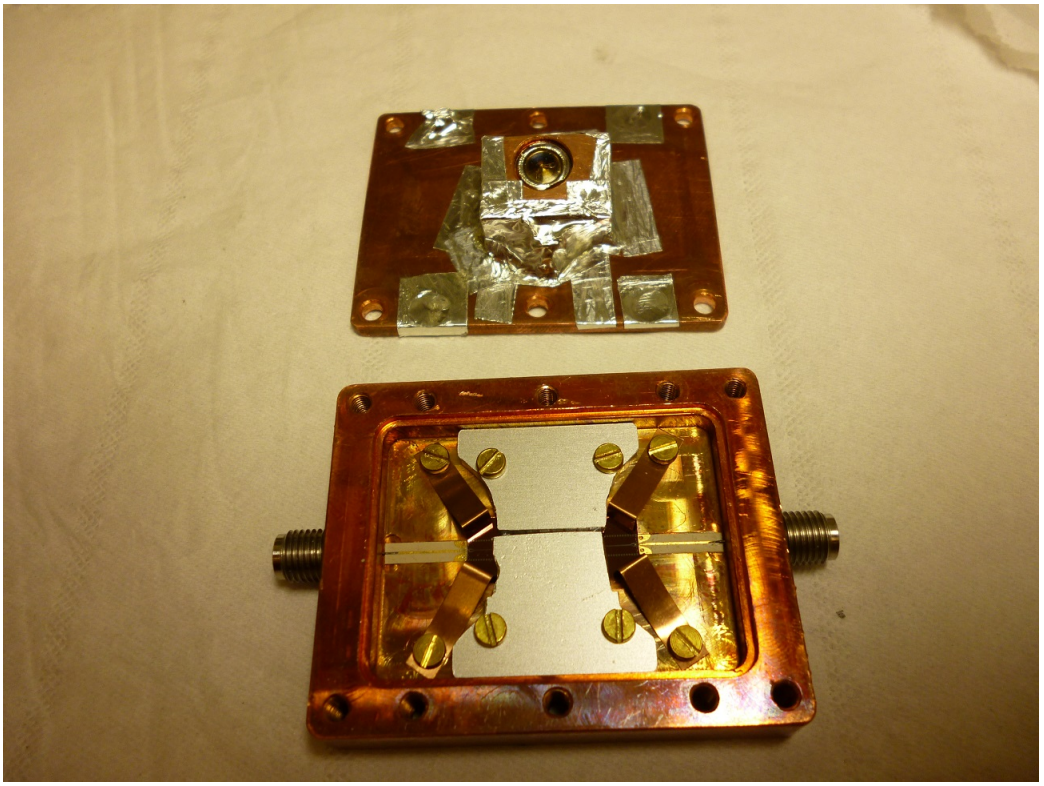

FIGURE 3.17: The detectors holder with an aluminum collimator mounted above the detectors in order to focus the X-rays on the central part of the inductor on an area $\sim$ 1 mm wide to ensure uniformity of response and to avoid interactions in the IDCs. On the top it is visible the lid of the holder with the ^{55}Fe source mounted.

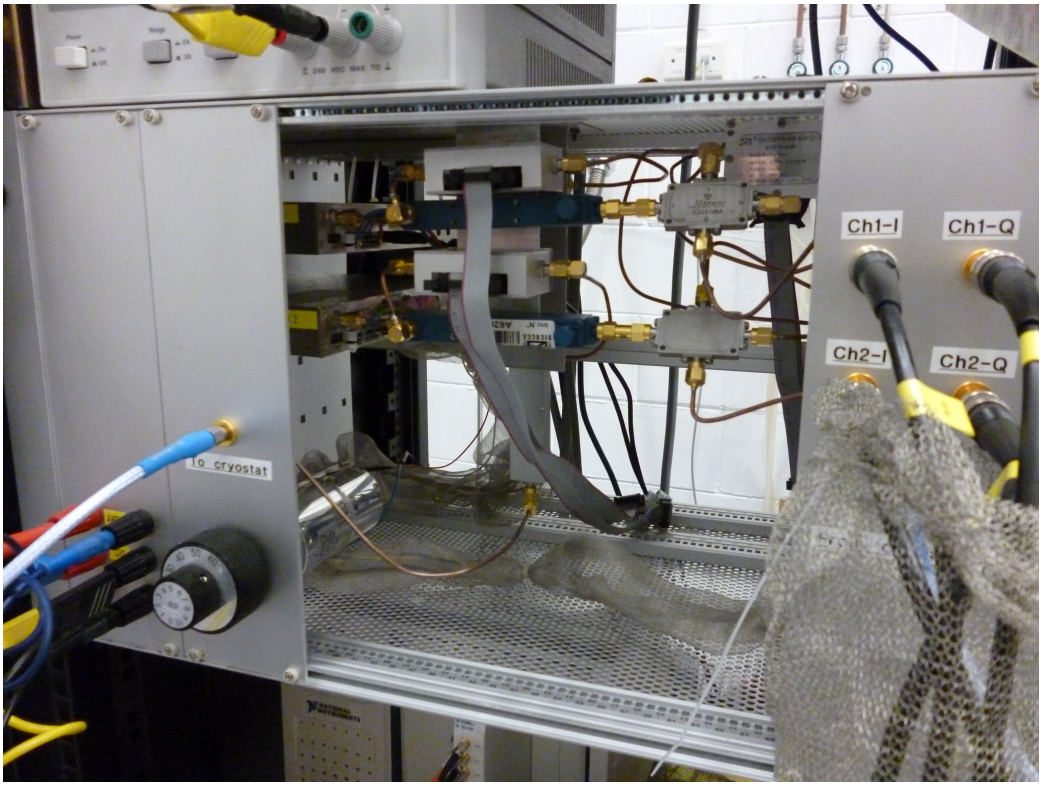

FIGURE 3.18: The room-temperature electronics used to readout two resonators at the same time.

Chapter 4

Data analysis

The devices described in the chapter 3 have been characterized both from the static point of view and with low energy X-ray sources to test the response of the detector to release of energy. In this chapter the methods used to obtain the most interesting parameters will be discussed, and the results will be reported.

4.1 Obtaining the resonator parameters

In order to measure the steady-state parameter of the resonators, the array was mounted on a dilution fridge capable of 40 μW of cooling power at 100 mK (Oxford MX-40, testbed at the Cryogenics Laboratory of the University of Milano-Bicocca) and cooled down to temperatures in the (25 mK $\div$ 1000) mK range, depending on the critical temperature of the films. Each resonator was characterized by measuring the resonant frequency and the quality factors with a Vector Network Analyzer (HP 8753E, 30 kHz $\div$ 6 GHz). In figure 4.1 an example of a single resonance with its fit are reported, while in figure 4.2 a typical transmission spectrum of an array device is shown.

4.1.1 Critical temperature

The critical temperature of the films was evaluated by measuring the average transmitted signal S_{21}^{ave} through the CPW line on a frequency range containing the resonant frequencies versus the temperature of the chip. While the temperature decreases, eventually the

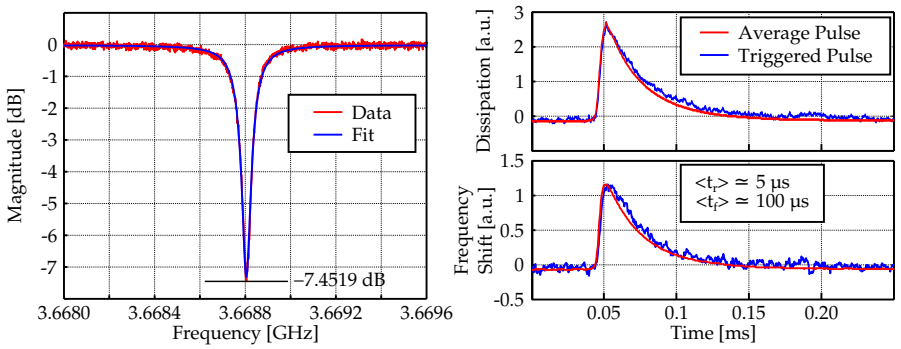

FIGURE 4.1: An example of resonant frequency measurement, acquired by a Vector Network Analyzer. In this example the resonant frequency, corresponding to the minimum transmitted signal, is $f_0 = 3.6688$ GHz.

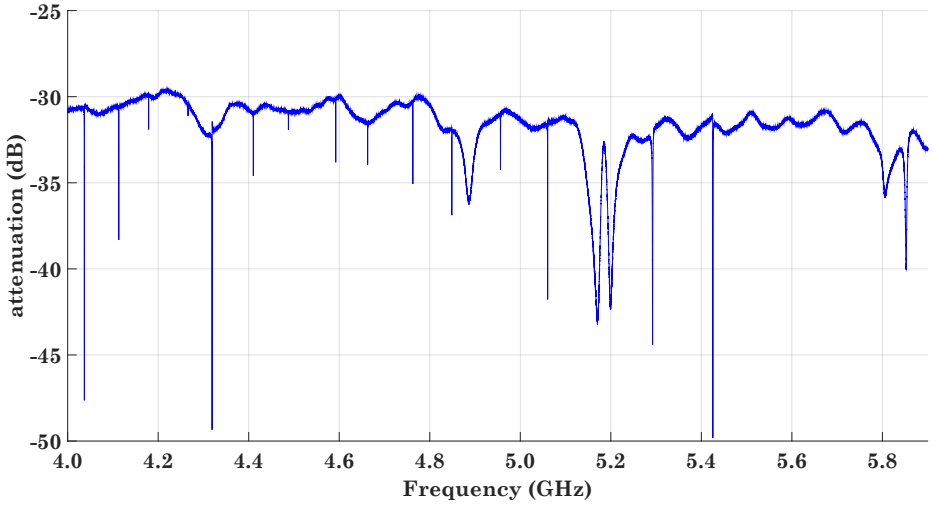

FIGURE 4.2: Transmission through the resonator array chip. Vertical lines in the spectrum are the resonances from individual detectors of the array.

S_{21}^{ave} will increase, indicating a drop in the resistance of the film due to the transition of the metal into the superconducting condition (fig. 4.3). The curve so obtained has the shape of the sigmoid, and the temperature at which the average transmitted signal is at the level of 20% of the jump is identified as the critical temperature of the film.

4.1.2 Quality factors and resonant frequencies

The equation 2.44 shows the dependence of the transmitted signal S_{21} on the quality factors of the resonance: the coupling and total quality factor. In order to convert the I and Q raw data into resonant frequency shift and dissipation shift, the determination of the quality factors and resonant frequencies must be done in a very accurate way. Petersan *et al.* [105] provide a quantitative comparison of the different possible methods

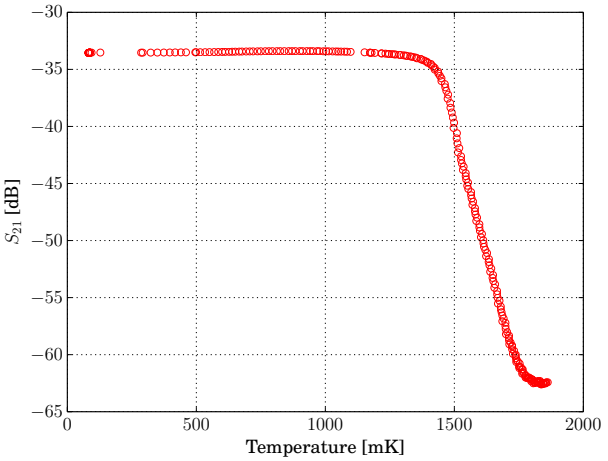

FIGURE 4.3: Measurement of the T_c of a Ti/TiN multilayer film with $T_c = 1.6$ K.

and, among them, the fit procedure proposed in [106] was chosen. The total forward transmission S_{21} through the microresonator, amplifiers and cables measured performing a frequency scan, can be written as:

$$S_{21}(f) = I + jQ = C(f)\left(1 - \frac{Q}{Q_c}\frac{e^{j\phi_0}}{1 - 2j\frac{f-f_0}{f_0} + jL}\right) \tag{4.1}$$

here f_0 is the resonance frequency. Respect to the eq. 2.44, the extra terms are necessary to keep into account the effects due to the non ideality of the system: ϕ_0 is a real parameter that takes care of the rotation of the resonance loop due to impedance mismatches, L is a parameter that accounts for the perturbation of both the electric and magnetic fields around the feedline due to the presence of the resonator itself [107] and $C(f)$ is a complex function which accounts for the background transmission of the readout line.

4.1.3 Fraction of kinetic inductance

A very important parameter which affects the sensitivity of the superconducting microwave microresonator is the fraction of the kinetic inductance α. It is defined as the ratio between the kinetic inductance L_k caused by the inertia of the superconducting pairs and the total inductance L, which contains also the geometrical term L_g. This parameter sets the frequency shift of the resonance per quasi-particle produced by an interaction.

The method used to determine the α parameter consists in simulating the resonator with an *em* simulator (Sonnet; an example of one resonator simulated is reported in fig. 4.4) and setting the metal used to simulate the resonator to be lossless and with zero surface inductance. In this way the simulated resonant frequency obtained is only set by the geometrical properties of the design. The kinetic inductance is then derived from the difference between the measured and simulate resonance frequencies [108]: remembering that $f_{meas} \propto (L^{-1/2})$ and $f_{sim} \propto (L_g)^{-1/2}$, the alpha is given by:

$$\alpha = 1 - \left(\frac{f_{meas}}{f_{sim}}\right)^2 \tag{4.2}$$

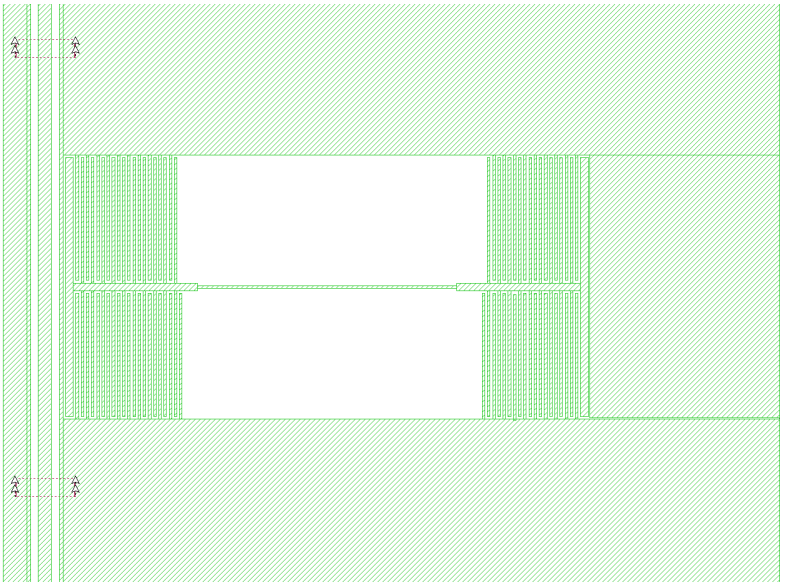

FIGURE 4.4: One chip of the second production run reconstructed with the Sonnet software.

4.1.4 Gap parameter

Another fundamental parameter that affects the theoretical energy sensitivity achievable with a pair-breaking detector is the gap parameter, which sets the number of quasi-particles produced per unit of energy. Despite within the BCS theory the ratio between this value and the critical temperature is set by the relation [109]

$$2\Delta \simeq 3.52 k_B T_c \tag{4.3}$$

in some materials it could deviate from the BCS value. This behavior could be consistent with a hypothesized positional variability of the gap in very resistive superconducting films (i.e. with high surface inductance, like in the case of TiN).
Remembering the equations 2.28 and 2.29, it is possible to relate the temperature dependence of the internal quality factor to the gap parameter, providing in this way a tool to access this quantity:

$$\frac{1}{Q_i(T)} = \frac{1}{Q(0)} + \frac{\alpha\sigma_1(T,\Delta)}{2\sigma_2(T,\Delta)} \tag{4.4}$$

The previous equation provides degenerate solutions in α and Δ, so only one of the two parameters can be obtained from the temperature sweep. Once the fraction of kinetic inductance is determined with the Sonnet simulation, it is possible to evaluate the gap parameter avoiding the degeneracy. The internal quality factor was measured in the range of temperatures from 0.025 to 1 K (figure 4.5), depending on the critical temperature of the film.

The static measurements of the critical temperature, the fraction of kinetic inductance, the gap parameter and the maximum internal quality factor achievable with the available films are summarized in the table 4.1.

4.2 X-rays detection

The technology of the superconducting microwave microresonator needs to be optimized to measure the energy released within the electron capture of ^{163}Ho, which decays on ^{163}Dy leaving it on an excite state. The dysprosium de-excite mostly in non radiative way consisting in electrons with maximum energies of $\sim$ 2.5 keV. In order to test the detectors X-ray sources with energies close to the one from the EC of Ho were chosen, namely a ^{55}Fe source ($E_{k_\alpha}^{Mn} \simeq 5.9$ keV) and an aluminum fluorescence source ($E_{k_\alpha}^{Al} \simeq 1.5$ keV) excited by a primary alpha source made of ^{241}Am. The X-rays were collimated by means of an aluminum collimator on an area $\sim$ 1 mm wide around the central part of the inductor.
In this case the IQ data are acquired with the homodyne setup, so in addition to the corrections present in the eq. 4.1, another correction must be introduced, accounting for the non-ideality of the mixers: the ideal response of the mixing of two RF signals

Film	$\mathbf{T_c}$ **(K)**	$\mathbf{\Delta_{BCS}}$ **(meV)**	$\mathbf{\Delta}$ **(meV)**	$\boldsymbol{\alpha}$	$\boldsymbol{L_s}$ **(pH/sq)**	**Thickness (nm)**	$\mathbf{Q_i}$	$\mathbf{Q_{tot}}$
Stoichiometric TiN	4.6	0.69	0.60 ± 0.02	0.074 ± 0.008	2.5	250	$<6 \cdot 10^5$	$<10^5$
Substoichiometric TiN	2.5	0.38	0.374 ± 0.006	0.54 ± 0.01	12.6	160	$<10^6$	$<9 \cdot 10^4$
Ti(10 nm)/TiN(15 nm)×8	1.6	0.24	0.250 ± 0.002	0.52 ± 0.02	10.9	200	$<1.5 \cdot 10^5$	10^5
Ti(10 nm)/TiN(12 nm)×8	1.2	0.18	0.172 ± 0.002	0.71 ± 0.03		176	$<10^5$	$<2 \cdot 10^4$
Ti(10 nm)/TiN(12 nm)×9	1.2	0.18	0.200 ± 0.004	0.26 ± 0.01	13.1	198	$<10^5$	10^4

TABLE 4.1: Results of the static characterization of the superconducting films. The alpha measured for the second devices is about one half of the value measured in the "old" geometries: this is due to the difference in the design of the inductor, going from being a CPS to a CPW with the ground planes far away from the central inductor. The sheet inductance L_s was determined from the sheet resistance of the films in their normal state. By multiplying the sheet inductance by the thickness it is possible to compare the film through their inductivity: in this case the substoichiometric film is quite similar to the multilayer one, with values of inductivity of 2020 and 2180 pH·nm, respectively. All the films show to posses gap parameters close to the expected value from the BCS theory.

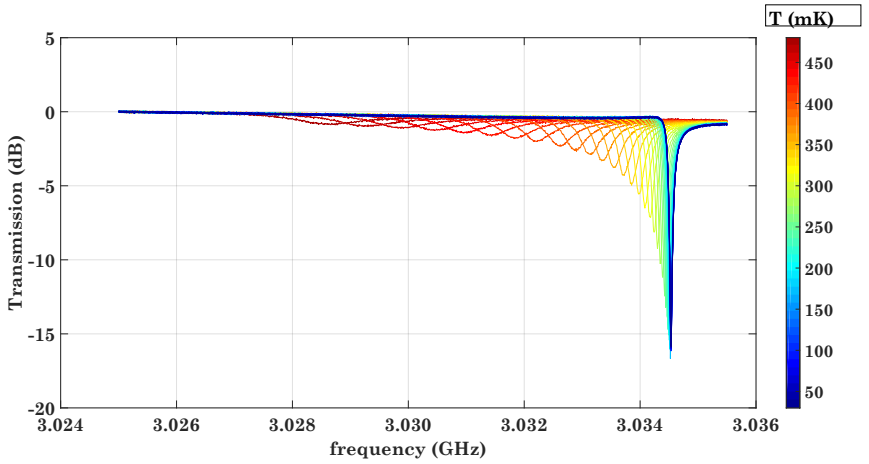

(A)

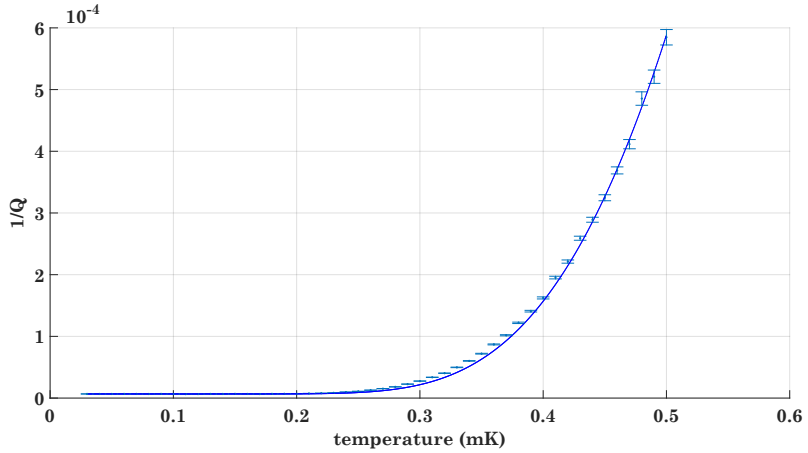

(B)

FIGURE 4.5: Measurement of the gap parameter:(A) Resonance profile of a Ti/TiN multilayer 10/15 nm resonator as a function of the temperature. (B) The inverse of the internal quality factor of the same resonator as a function of the temperature.

very close in frequency is expected to be a circle, while the non-ideality condition of the real instrument deforms the circle into an ellipse, i.e. the I and Q axis deviate from being perfectly perpendicular of a small angle that must kept into account. The overall contribution of the instrumentation makes the measured resonance loop to deviate from being a perfect circle. An example of a measured IQ loop is reported in figure 4.6, blue line. The corrections described in the eq. 4.1 and the correction of the mixer are used to correct the acquired data. The procedure used to extract the proper frequency and amplitude signal from the I-Q data obtained from the homodyne apparatus (fig. 3.16), is composed of several steps:

- **Line correction**: the synthesizers and mixers suffer of a frequency dependent

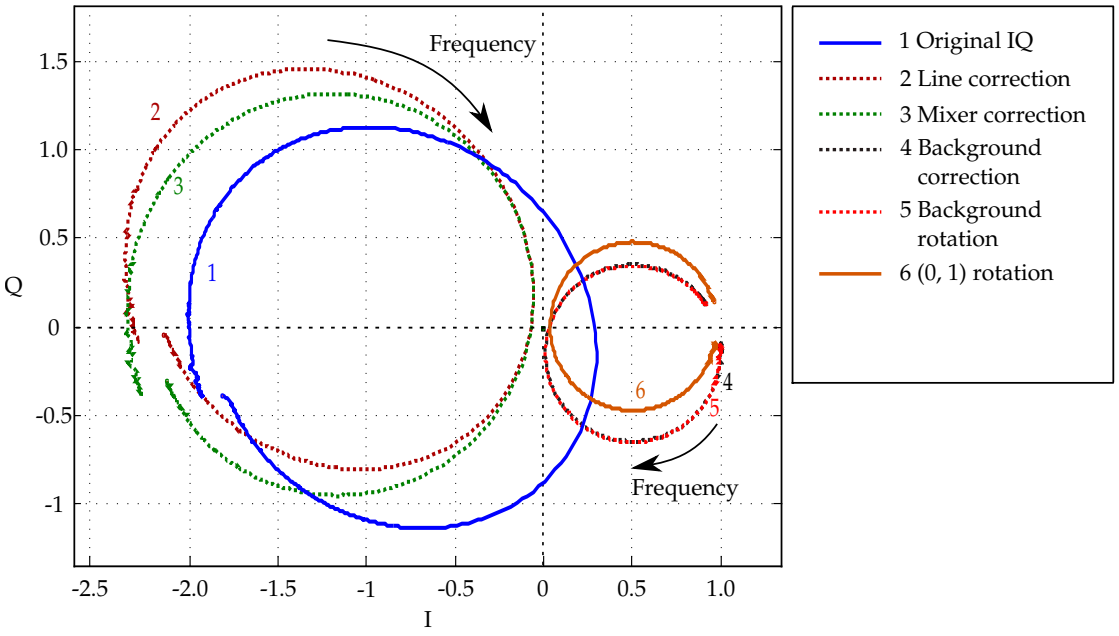

FIGURE 4.6: Correction applied to the acquired IQ loop to restore the original shape of the resonance.

offset in the IQ plane. For this reason the I-Q output with the RF port disconnected is subtracted from the original resonance profile (figure 4.6, line 2);

- **Mixer correction**: as mentioned, the mixer's I-Q axis are not perfectly perpendicular. Assuming that the LO port is fed with a microwave signal $\sin(\omega t)$ and the RF port is fed with $A\sin(\omega t + \theta)$, the I and Q are expected to be

$$I = I_0 + A_I \cos(\theta) \tag{4.5}$$

$$Q = Q_0 + A_Q \cos(\theta + \Delta\theta) \tag{4.6}$$

In the case the mixer response is ideal $\Delta\theta = \pi/2$, $I_0 = Q_0 = 0$ and $A_I = A_Q$ then the curve in the I-Q plane for different values of θ is a circle. Real mixers display an ellipse rotated and shifted that necessarily needs to be translated into the ideal circle. By fitting the ellipse with the equations 4.5 and 4.6 it is possible to find the transformation that maps the ellipse into the circle. This correction is applied to the resonance profile (figure 4.6, line 3);

- **Background correction**: since the path between the synthesizer and the LO port necessarily contains a number of wavelength of the probe signal different from the number of wavelength contained in the path between the synthesizer and the RF port, the response of the mixer shows a frequency-dependent output. The response

of the line at different frequencies changes both with the amplitude ($\Lambda_{ampli}(\omega)$) and with the phase ($\Lambda_{phase}(\omega)$), figure 4.7. Their behavior is fitted with a polynomial

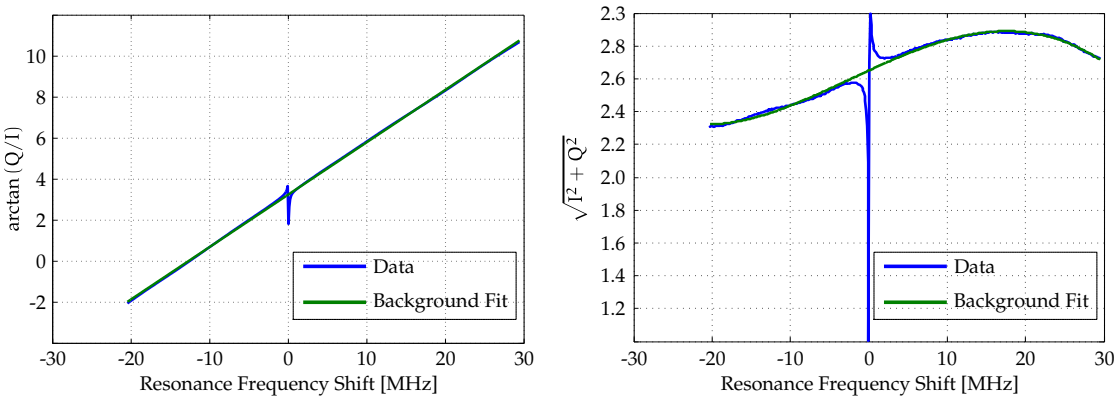

FIGURE 4.7: Background correction: the response of the line at different frequencies changes in phase (left) and amplitude (right). These variations are fitted by using a polynomial function.

function and then the resulting correction is applied to S_{21} (figure 4.6, line 4):

$$S_{21} \rightarrow S_{21} \frac{e^{-j\Lambda_{ampli}(\omega)}}{\Lambda_{phase}(\omega)} \tag{4.7}$$

- **Background rotation**: at this point the resonance is a circle in the IQ plane that could possibly be rotated respect to the origin. To correct this effect, a counter-rotation of an angle ψ with respect to the center is applied (figure 4.6, line 5).

$$S_{21} \rightarrow S_{21} e^{j\psi} \tag{4.8}$$

- **Asymmetry rotation**: non-ideal experimental setups can also lead to an asymmetry in the resonance shape which corresponds to a rotation of the resonance circle [110]. To correct this effect a rotation of an angle θ and a contraction mapping of $\cos(\theta)$ with fixed-point (0,1) is added (figure 4.6, line 6):

$$S_{21} \rightarrow 1 - \cos(\theta) e^{j\theta} (1 - S_{21}) \tag{4.9}$$

The so obtained S_{21} profile is close to be a perfect circle in the canonical position as shown in figure 2.4a. This reconstruction procedure in the I-Q plane permits to obtain a proper calibration of the resonance measured with the same setup that is used to acquire the signals coming from energetic events. However the pulses in the I-Q plane do not express quantities directly related to the energy detected. For this reason the Möbius

transformation

$$S_{21}^{*} = \frac{1}{1 - S_{21}} = \frac{Q_c}{Q} + 2jQ_c\frac{f - f_0}{f_0} \tag{4.10}$$

is applied, bringing to the quantities that correctly estimates the energy measured by the detector, namely the amplitude (eq. 2.46) and frequency (eq. 2.47) signals. From a geometrical point of view the transformation 4.10 maps the I-Q circle into a straight vertical line in the frequency-amplitude plane. Thus moving vertically means shifting the resonance frequency, while moving orthogonally to it means changing the total quality factor, i.e. a variation in the amplitude.

In order to minimize the amplitude-dependent time walk, the signals were triggered off-line by using a Constant-Fraction Discriminator with fixed pre-trigger and fixed event length. In this way it is possible to produce energy spectra of the X-rays sources used for the tests. Finally, by evaluating the exponential decay time of the signals, it was possible to extract the quasi-particles recombination time[1].

4.2.1 Run 1 and 1.5

With the first geometry it was possible to appreciate the increase of sensitivity while tuning the critical temperature (i.e. the gap) of the superconductor below the value of the stoichiometric TiN (fig. 4.8).

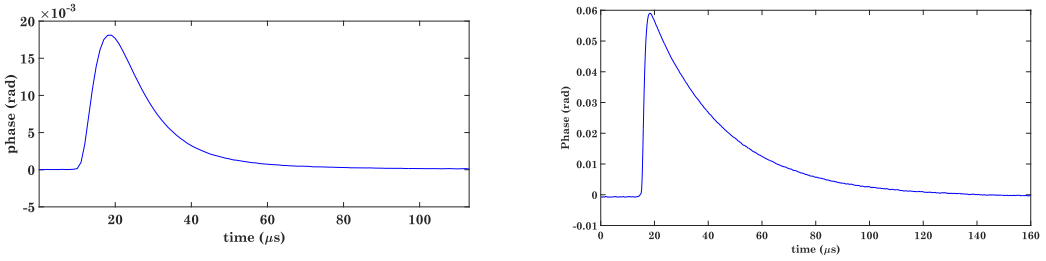

(A) (B)

FIGURE 4.8: Comparison of the average pulse obtained with stoichiometric TiN ((A)) and Ti/TiN multilayer with critical temperature of 1.6 K ((B)): it is possible to see how the signal to noise ratio is improved by decreasing the critical temperature. To be noted the lengthening in the decay time, caused by a decrease in the recombination rate of the quasi-particles.

[1]The approximation where the decay time is identified as the recombination time is valid as long as the signals decay with a single decay constant which is required to be long compared to the down-ring time (eq. 2.65). A more detailed discussion of the decay times will be given in the following.

In all four the cases and with both the X-ray sources available the energy spectrum did not feature any family attributable to a monochromatic energy peak, but a continuum was observed instead (fig. 4.10).

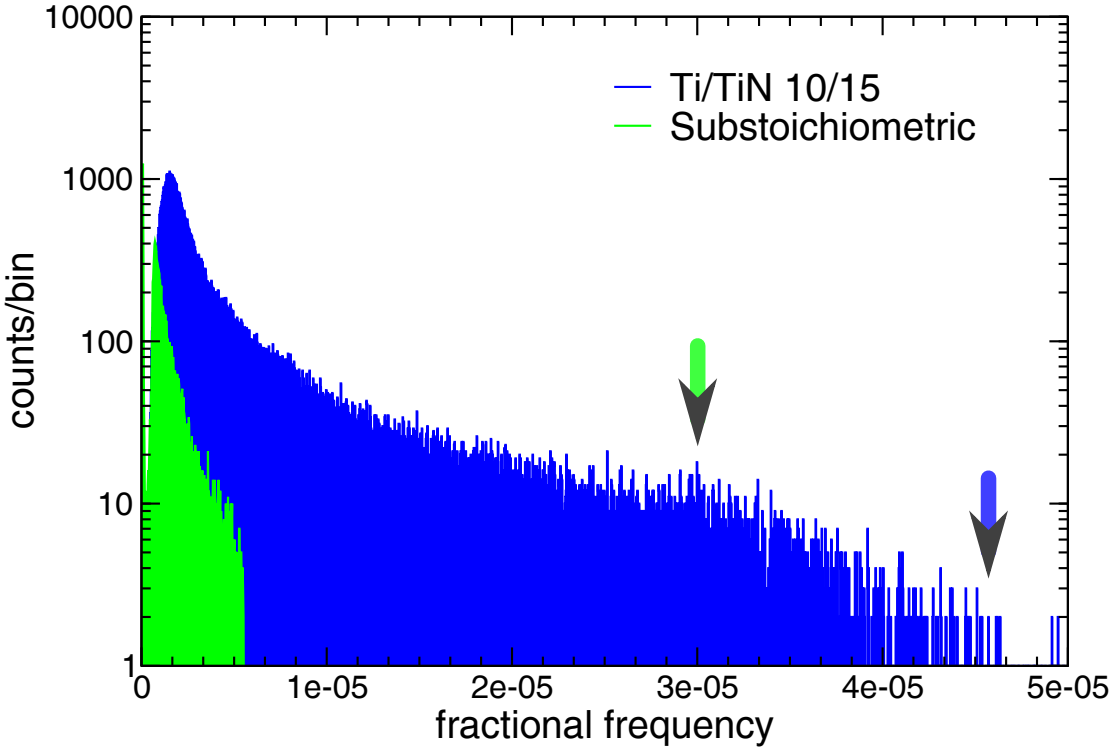

FIGURE 4.9

FIGURE 4.10: Energy spectrum acquired with an Al fluorescence source (1.5 keV) with a resonator made of Ti/TiN 10/15 multilayer (blue) and with a resonator made of substoichiometric TiN (green). The difference in the maximum fractional frequency shift observed by the two films is due to the different dynamics of the two resonators: the highest observed pulses made saturate the response of the detector made of substoichiometric TiN, pushing the resonance out of the available dynamics. Still, in the case of a resolving detector, a peak corresponding to the maximum detectable energy would have been expected. The expected fractional frequency shifts for the two films are $\sim 4.7 \cdot 10^{-5}$ and $\sim 3 \cdot 10^{-5}$, respectively[2]. The difference in the expected fractional frequency shifts is due to the difference in the gap parameters, which make the multilayer more sensitive respect to the substoichiometric film.

Three different families of pulses were observed with the multilayer and sub stoichiometric films: pulses with a single, slow, decay constant, pulses with a single, fast, decay constant and pulses with both the components (4.11). The pulses were fitted with a function characterized by a single exponential constant on the rise of the signal and two time constants on the fall. The rise time is limited by the down-ring time, set by the bandwidth of the resonator. The study of the behavior of the decay times as a

[2]The expected values of the fractional frequency shifts were obtained with the eq. 2.50 and assuming $N_0 = 4 \cdot 10^{10}$ $\mu\text{m}^{-3}\text{eV}^{-1}$ and $\eta = 0.4$. Nevertheless, this values suffer of great uncertainty.

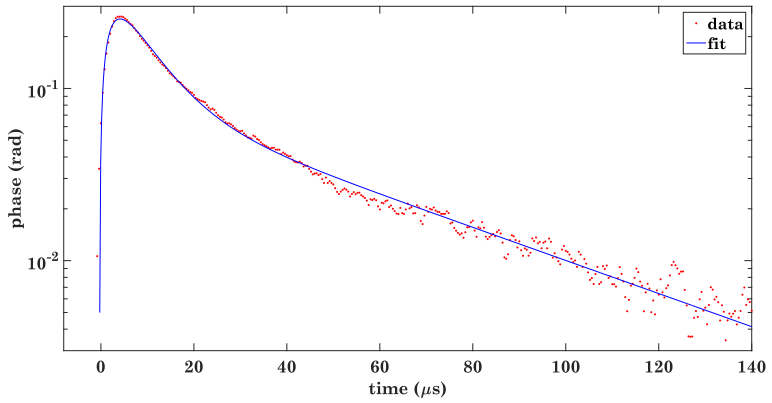

FIGURE 4.11: An example of a pulse with a double decay constant acquired with a 10/15 multilayer film caused by a 1.5 keV X-ray.

function of the temperature (figures 4.12, 4.13) has allowed to understand the reason of such a phenomenon: given the very small thickness of the films, the majority of the events takes place in the substrate, where phonons are produced giving rise to a position-dependent response in the detector. This explanation was confirmed by observing events in coincidence on two adjacent resonators.

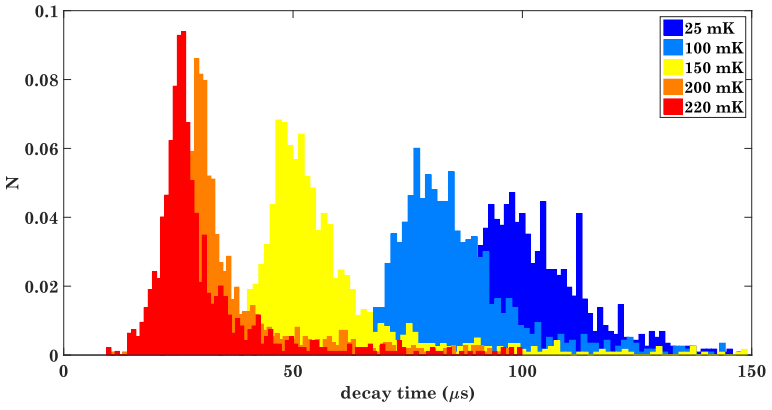

FIGURE 4.12: Measured quasi-particle recombination time in a Ti/TiN multilayer 10-15 nm film as a function of the temperature.

On the other hand, in the case the X-ray is absorbed in the superconductor, high energy phonons could leak into the substrate. In the latter case it is possible that due to the slow diffusivity characteristic of TiN the concentration of quasi-particles is locally increased, causing an effective volume over which the energy is converted into quasi-particles smaller than the entire volume of the detector. This would bring to increase the probability of one quasi-particle to find a partner to recombine with, decreasing in this way the fall time of the signals. In the extreme situation the superconductor could possibly become locally normal. This effect is not detectable in the case of the

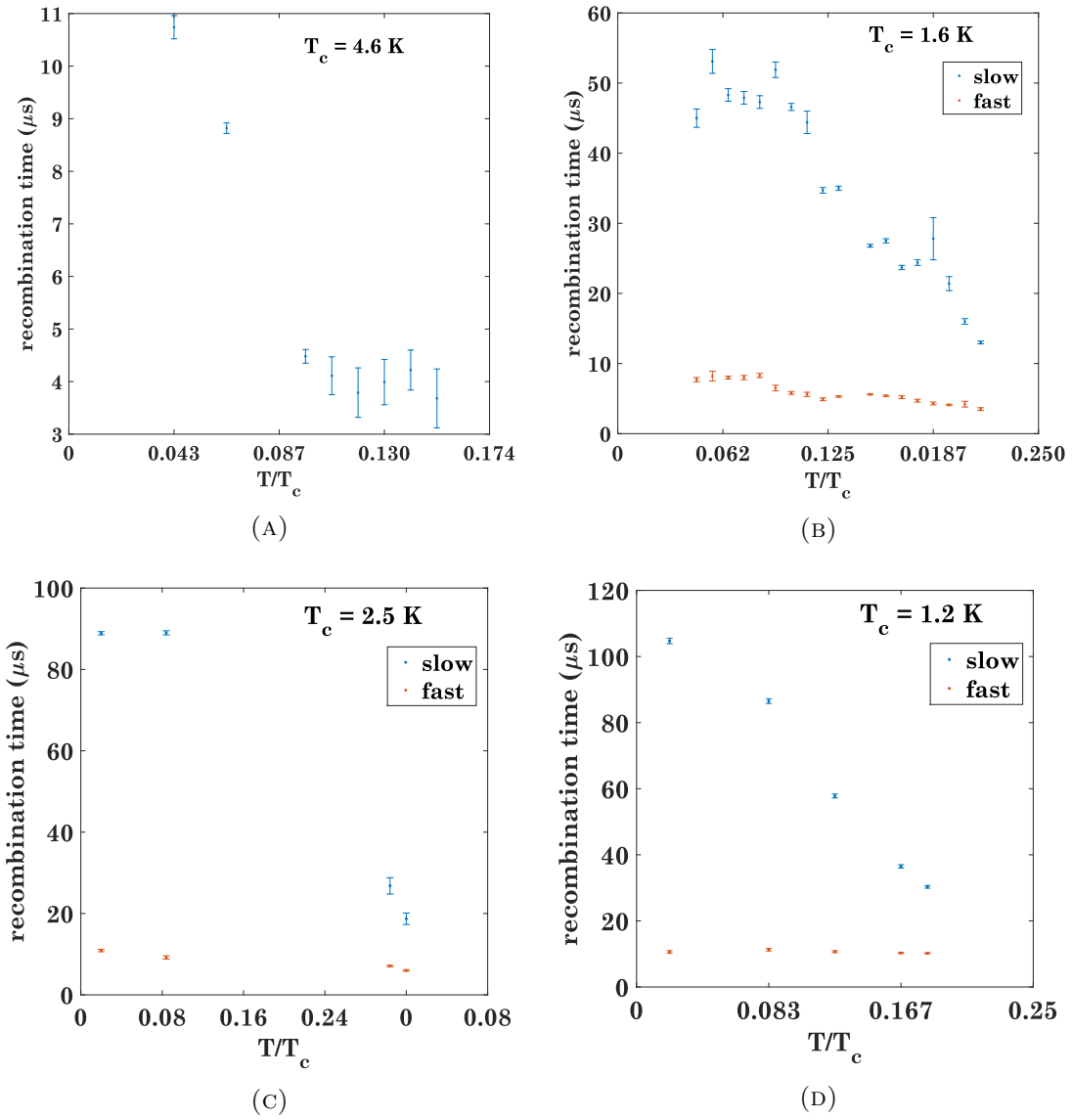

FIGURE 4.13: Comparison of the decay times for different films of TiN. The "fast" and "slow" components have been evaluated by fitting the pulses with a function characterized by a single exponential constant on the rise of the signal and two time constants on the fall. The rise time was verified to be limited by the down-ring time, set by the bandwidth of the resonator. (A) The stoichiometric TiN shows the faster recombination time of all, having the highest critical temperature of all the samples. Then in decreasing order of recombination time: (B) Ti/TiN 10/15, (C) substoichiometric film and (D) Ti/TiN 10/12. Despite the higher critical temperature of the substoichiometric film respect to the 10/15 multilayers, the former shows a longer recombination time, indicating a slight difference among the processes taking place in the two materials.

stoichiometric film as the recombination time is too similar to the fast component to distinguish the two behaviors.

The recombination times at low temperature are reported in the tab. 4.2

Film	τ_{slow} (μs)	τ_{fast} (μs)
Stoichiometric TiN	10.7 ± 0.2	//
Substoichiometric TiN	88.9 ± 0.4	10.9 ± 0.3
Ti (10 nm)/TiN (15 nm) × 8	48.2 ± 0.7	7.9 ± 0.2
Ti (10 nm)/TiN (12 nm) × 8	104.7 ± 0.8	10.4 ± 0.4

TABLE 4.2: Comparison between the decay times of the films produced within the first run evaluated at low temperature ($k_BT \ll \Delta$). The fast component of the stoichiometric TiN is not evaluated since the recombination time of this film is too short to distinguish such effect.

4.2.2 Run 2

The chips coming from the geometry produced within the second run were tested with the Al and ^{55}Fe X-ray sources, evaluating the decay time and building the energy spectrum. The spectrum of one resonator with the inductor suspended from the substrate was compared with the spectrum obtained with a resonator with the inductor in the "standard" configuration. Also in this case the energy spectrum did not show any feature of resolution (fig. 4.14).

The quasi-particle recombination time as a function of the temperature measured with the detectors with the suspended inductor is reported in the figure 4.15, obtaining a recombination time at low temperature of (78.7 ± 1.9) μs with a fast component equal to (9.2 ± 0.2) μs.

4.3 Noise

The noise was evaluated for the available devices, comparing the measured white noise with the expected noise caused by the HEMT amplifier. In all the cases the noise resulted to be limited by the HEMT, with an excess noise observed at low frequency. The level of the white noise obtained with the different materials are summarized in the table 4.3. The contribution of the low frequency noise does not change when varing

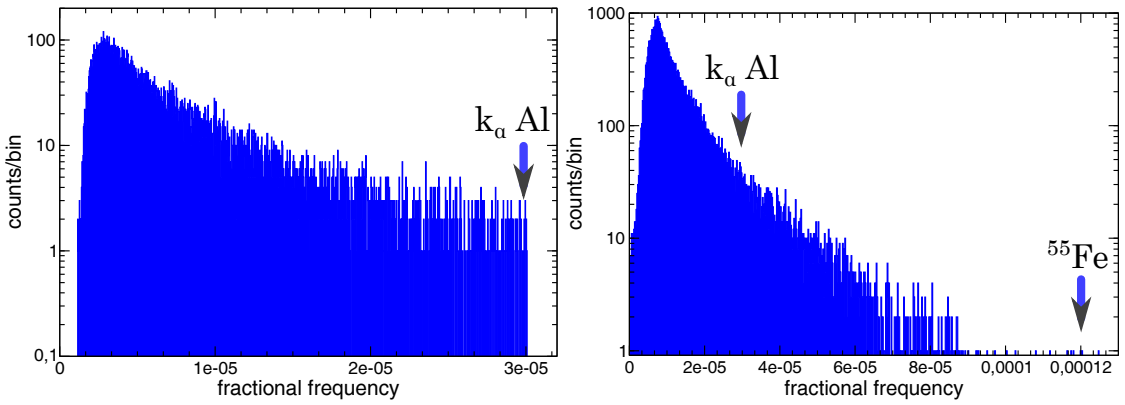

(A) (B)

FIGURE 4.14: (A) Energy spectrum acquired with a ^{55}Fe plus an Al fluorescence source (1.5 keV) with a resonator of the second production run with the inductor in contact with the substrate. (B) Energy spectrum acquired with the same sources detected by a resonator with the suspended inductor. The difference in the maximum fractional frequency shift observed by the two films is due also in this case to the different dynamics available to the two resonators. The expected fractional frequency shift due to the ^{55}Fe line for both films is $\sim 1.2 \cdot 10^{-4}$, while it is $\sim 3 \cdot 10^{-5}$ for the Al line.

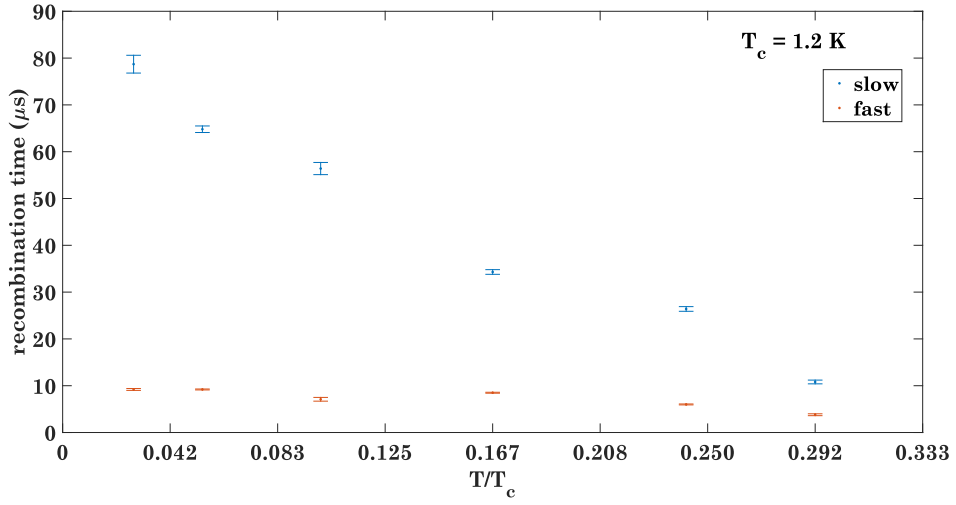

FIGURE 4.15: Recombination times as a function of the temperature obtained with the sensors produced within the second run with the inductor suspended from the substrate.

the temperature (fig. 4.17) and the driving power (fig. 4.16) of the detectors. For this reason the excess noise at low frequencies was not identified as the contribution of the TLSs, but as due to the presence of pulses below the threshold. The detectors with this noise have shown to achieve a maximum signal to noise ratio of the order of $\sim 10^3$ with the highest signals detected.

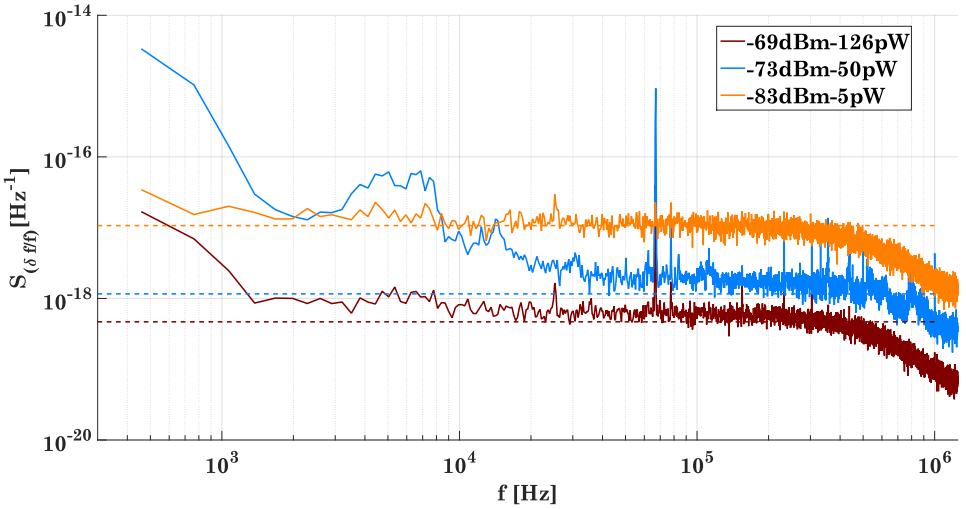

FIGURE 4.16: Noise power spectrum of a Ti/TiN 10/12 chip measured as a function of the driving power. The dashed lines are the expected noise level set by the HEMT amplifier. In the spectrum the roll-off due to the anti-aliasing filter at 500 kHz is visible.

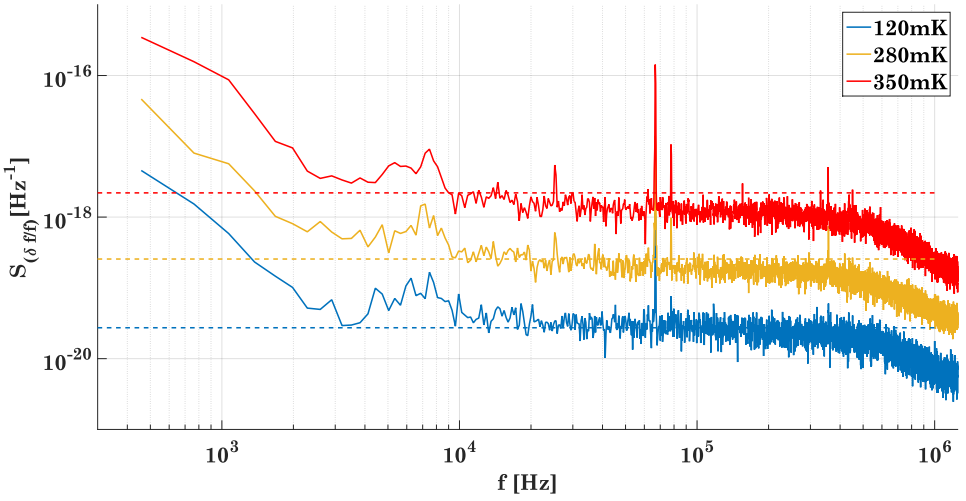

FIGURE 4.17: Noise power spectrum of a Ti/TiN 10/12 chip measured as a function of the temperature. The dashed lines are the expected noise level set by the HEMT amplifier.

Material	P_{drive} **(dBm)**	**HEMT noise (Hz)**
Substoichiometric TiN	-80	$6.7 \cdot 10^{-20}$
Ti/TiN 10/12 × 8	-90	$9.8 \cdot 10^{-19}$
Ti/TiN 10/15 × 8	-60	$3.7 \cdot 10^{-22}$
Ti/TiN 10/12 × 9	-58	$7.2 \cdot 10^{-22}$

TABLE 4.3: The noise level on the fractional frequency shift obtained with the various materials. The large difference between the noises obtained is strongly dependent on the resonator chosen for the analysis.

Chapter 5

Conclusions

The work described in this thesis is the starting point of a long term project. During my PhD it was possible to lay the groundwork of a broader plan that could lead the superconducting microwave microresonator to be a reliable and competitive technology to be used in the framework of the neutrino physics experiments. The measurements made constitute a starting point for further investigation and improvements.

One of the results obtained within my PhD work concerned the comprehension of the technology of superconducting microwave microresonator, which was introduced for the first time in the Milano-Bicocca University, and the acquisition of the capability necessary to deal with this kind of technology. A dilution unit previously used for other purposes was instrumented with the electronics required to read out the detectors. In particular a cold microwave amplifier was mounted on the 4 K stage of the cryostat and the semi-rigid coaxial cable were installed, choosing a superconducting Nb cable for the output line. The warm electronics, made of a microwave synthesizer, a warm amplifier, an IQ mixer and the DAQ system, was also installed and optimized. In order to acquire and convert the data coming from the homodyne apparatus used to readout the detectors into the quantities proportional to the energy released in the resonators - the resonant frequency shift and the variation of amplitude of the transmitted signal - a dedicated software package was developed. The obtained system was demonstrated to be able to readout two channels at the same time, providing the capability to perform coincidence measurements. The scalability to a higher number of multiplex should only be limited by the bandwidth of the available commercial fast digitizers.

In order to consider the effects of the critical temperature (i.e. the gap) on the sensitivity,

the devices measured were made of TiN with different stoichiometric ratios. The reduced T_c was obtained by superimposing thin layers of stoichiometric TiN to pure Ti layers, and the T_c was tuned by varying the ratio between the thickness of the layers, exploiting the *proximity effect*. The characterization of the devices on one hand concerned the measurement of the static parameters of the superconductor, namely the critical temperature, the gap parameter, the fraction of kinetic inductance and the quality factors. On the other hand the detectors were tested as single particle detectors, acquiring the pulses caused by the interaction of the X-rays emitted by two test sources with energies of $\sim$ 5.9 keV (^{55}Fe) and $\sim$ 1.5 keV (k_α fluorescence line of Al). These measurements allowed to establish the recombination time of the quasi-particles for each material as a function of the temperature, obtaining noise to signal ratios as high as $\sim 10^3/\sim 10^4$.
The devices were produced in two different "lumped-element" designs: from the energy spectrum acquired with devices coming from the first production run it was possible to identify the issues that prevent the detectors from manifesting a unique response to a monochromatic energy source. The energy spectrum, indeed, did not show any structure ascribable to a monochromatic energy source: the incapability to resolve monochromatic energies was attributed to an exchange of phonons between the superconductor and the substrate it leans on; given the small thickness of the superconductor ($\sim$ 200 nm at most), the majority of events takes place in the substrate, giving rise to a population of high energy phonons that could reach the detector in a quantity that depends on the position of the interaction, causing a position-dependent energy response. This explanation was confirmed by observing coincidence events on two adjacent resonators, symptom of the fact that the phonons from the substrate can excite the resonators.
In order to prevent this kind of problematics, a second production run with a revisited design was done, where the exchange of phonons between the superconductor and the substrate is avoided by etching away the substrate below the sensitive part of the detector, leaving an empty gap in its place. After testing this design, it was possible to argue that other problematics remain unsolved. For instance, the position dependent response of the detectors gives a sensible contribution, since from the measurements it is proved that the effects due to exchange of phonons are not entirely eliminated. Besides, stated the slow diffusivity of the quasi-particles in TiN, hot-spots of quasi-particles can be created in the superconductor consequently to an energetic interaction, leading to a faster recombination time that could negatively affect the energy collection process of the detector. Nevertheless other solutions have been proposed: by coupling a higher T_c

(and faster diffusing) superconducting absorber to the TiN of the resonator, it would be possible to allow the quasi-particle to diffuse and then they would be "trapped" in the TiN, decreasing also the fraction of events that would take place in the substrate and avoiding future issues related to the implantation of the Ho nuclei in the inductor. This design will be tested as soon as the complicated fabrication process will be completed.

Appendix A

Interaction of X-ray with Cooper pairs

For the purpose of this thesis, it can be useful to understand the processes that take place in a superconductor when an energetic photons is absorbed. Of course, in order to be able to break Cooper pairs and hence provoke a response of the detector, the incoming photon must possess an energy greater that $2\Delta \sim$ meV. The absorption of an X-ray with an energy E_X of few keV creates a photo-electron with energy $E_0 = E_X - E_b$, where E_b is the binding energy of the shell where the electron was extracted from. The energy conversion process occurs in three separate stages. During the first stage, which lasts for a time of the order of $\sim 10^{-15}$ s, the relaxation proceeds predominantly via electron-electron interaction[111]. From the moment the primary electron is emitted, it begins to scatter inelastically, ionizing and exciting the atoms that it encounters in its path. These scattering interactions produce secondary electrons and cause the path of the primary to straggle. The first stage is defined to be over when the primary electron has lost enough energy to be indistinguishable from the other electrons of the superconductor, meaning that it will possesses an energy of the order of few eV. The results of the interactions taking pace in the first stage cause the formation of a hot-spot of volume $\sim 0.1\ \mu\text{m}^3$ where the temperature of the electrons is elevated compared to the bath temperature, which results in a local decrease of the energy gap. For high density of energy, supercritical temperatures can be obtained, locally destroying the superconductivity[112].

Below the characteristic energy $E_c \cong (E_F E_D)^{1/2}$, where E_F and E_D are the Fermi and

Debye energies, the electron-phonon interaction becomes the main relaxation process[78]. In this phase the energy is stored in a distribution of very high energy phonons that are emitted by the electrons. An average quantity of $\sqrt{E_F/E_D} > 15$ phonons will be emitted before the electron reduces its energy below the Debye energy[113]. The second stage requires times of the order of $\sim 10^{-11}$ s, which make the first two stages too fast to be accessible by experiments.

During the third stage phonons and electrons form coupled systems, which can undergo multiple processes of relaxation, but only three are the dominant ones: the electron-phonon scattering, the recombination of two quasi-particles into a pair (with the emission of a phonon) and the pair breaking[78] (with the absorption of a phonon). The energy will be eventually dissipated in the substrate with the escape of low energy phonons, but the pair breaking mechanism results to be much faster than the phonon escape, allowing the phenomenon of the phonon trapping: the phonons coming from the recombination of the pairs break other couples, extending in this way the effective quasi-particle lifetime.

A.1 Diffusion

Before the recombination, the quasi-particles can diffuse inside the superconductor with a typical distance x_D that is related to the material and its temperature through the relation

$$x_D = \sqrt{D\tau_{qp}} \tag{A.1}$$

where τ_{qp} is the quasi-particles lifetime as given in eq. 2.63 and D is the diffusion constant. When the material is in its normal state, it has a diffusion constant equal to

$$D_n = \left(\rho_n e^2 N_0\right)^{-1} \tag{A.2}$$

here ρ_n is the normal state resistivity of the material and N_0 is the single-spin density of electron states at the Fermi energy. In the superconducting state, instead, the diffusion constant is related to the energy of the quasi-particles, and it is reduced respect to the normal state. In the case that the electron-impurities scattering is dominant, the ratio between the superconducting diffusion constant and its normal counterpart is given by[114]

$$\frac{D}{D_n} = \sqrt{\frac{2k_B T}{\pi\Delta}} \tag{A.3}$$

It was found experimentally that the actual value deviate from the predicted one for Ta[115] and Nb[116]; aluminum, on the other hand, seems to be less affected[117]. The observed low quasi-particle diffusion is probably explainable with the presence of traps.

Appendix B

Homodyne mixing

The information coming from the superconducting microwave microresonators is accessed with the homodyne mixing technique. Just like heterodyne technique, the signal that has to be demodulated is mixed with a reference signal. What distinguishes the homodyne is that only one signal is mixed with a copy of itself. The resonators are read by a circuit shown in fig. B.1 [118]. The probe signal is generated by a microwave

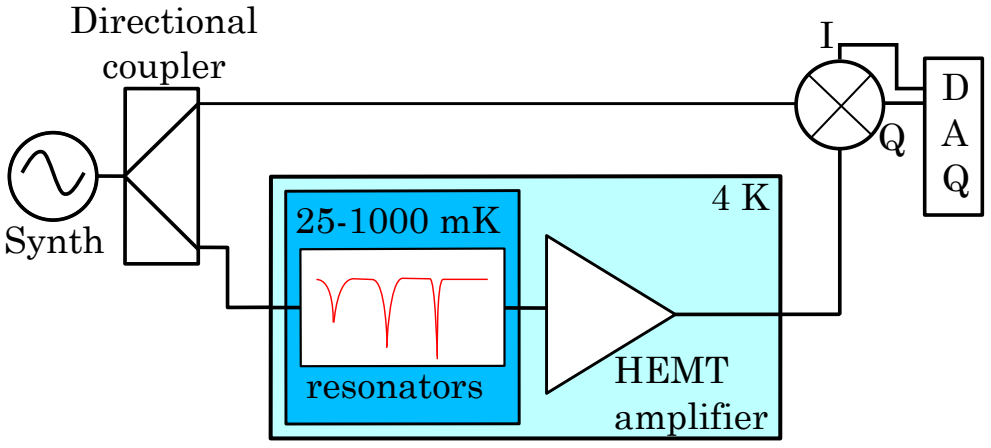

FIGURE B.1: The circuit diagram of a homodyne setup used to readout the superconducting microwave microresonators.

synthesizer, it is then split in two components by a directional coupler. One of the two signals is sent to the LO port of the IQ mixer, while the other enters into the refrigerator and passes through the feedline coupled to the resonators; after being amplified by a microwave amplifier it goes into the RF port of the IQ mixer. The two ports IQ mixer is actually composed by two mixers: one of the two inputs has included a 90 degrees shifter before its LO port. The ideal IQ mixer returns as output values the real component of

the transmission signal on the I channel and the imaginary component on the Q channel. In this way it is possible to retrieve the amplitude A and the phase ϕ of the original signal through the relations

$$A = \sqrt{I^2 + Q^2} \tag{B.1}$$

$$\phi = \tan^{-1}\left(\frac{Q}{I}\right) \tag{B.2}$$

B.1 IQ mixer

As already mentioned, the IQ mixer is actually composed of two mixers. The in-phase signal results by directly mixing the RF (Radio-Frequency) with the LO (Local Oscillator), while the quadrature signal Q is obtained from mixing the RF with the LO phase-shifted by 90° (fig. B.2). Considering that in a homodyne system the frequency

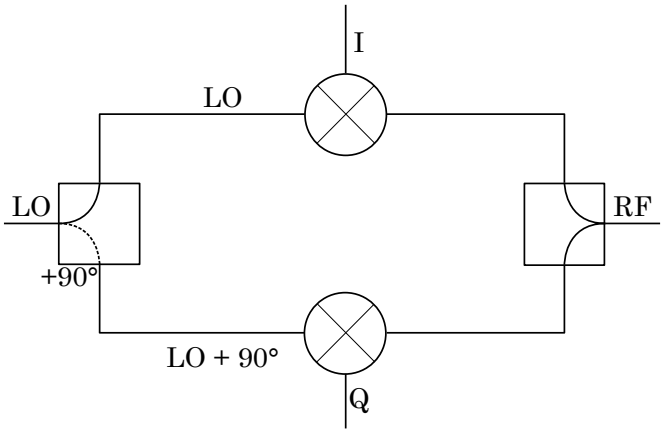

FIGURE B.2: An IQ mixer: the quadrature signal Q is obtained by shifting of 90° the phase of the LO, while the in phase signal I is obtained by mixing the LO signal with the RF signal.

of the RF and of the LO are the same, only the phase can distinguish the two input signals:

$$V^{\mathrm{LO}} = V_0^{\mathrm{LO}} \cos(\omega t) \tag{B.3}$$

$$V^{\mathrm{RF}} = V_0^{\mathrm{RF}} \cos(\omega t + \phi_0) \tag{B.4}$$

Analytically, the I signal is computed by the mixer as the product between the two input signals:

$$\begin{aligned} V_{\mathrm{I}} \propto V^{\mathrm{LO}} V^{\mathrm{RF}} &= V_0^{\mathrm{LO}} V_0^{\mathrm{RF}} \cos(\omega t) \cos(\omega t + \phi_0) \\ &= \frac{1}{2} V_0^{\mathrm{LO}} V_0^{\mathrm{RF}} \left[\cos(2\omega t + \phi_0) + \cos(\phi_0)\right] \end{aligned} \tag{B.5}$$

A low pass filter will cancel the radio-frequency term, making the I response to be the real component of the complex RF signal.

$$V_{\mathrm{I}} \propto \frac{1}{2} V_0^{\mathrm{LO}} V_0^{\mathrm{RF}} \cos(\phi_0) \tag{B.6}$$

On the other hand, the Q signal is computed in the same way, accounting in this case for a 90° shift on the LO signal:

$$V^{\mathrm{LO}} = V_0^{\mathrm{LO}} \cos\left(\omega t + \frac{\pi}{2}\right) \tag{B.7}$$

So the product between the RF and the LO signals in this case yields

$$\begin{aligned} V_{\mathrm{Q}} \propto V^{\mathrm{LO}} V^{\mathrm{RF}} &= V_0^{\mathrm{LO}} V_0^{\mathrm{RF}} \cos\left(\omega t + \frac{\pi}{2}\right) \cos(\omega t + \phi_0) \\ &= \frac{1}{2} V_0^{\mathrm{LO}} V_0^{\mathrm{RF}} \left[\cos\left(2\omega t + \phi_0 + \frac{\pi}{2}\right) + \cos\left(\phi_0 - \frac{\pi}{2}\right)\right] \\ &= \frac{1}{2} V_0^{\mathrm{LO}} V_0^{\mathrm{RF}} \left[-\sin(2\omega t + \phi_0) + \sin(\phi_0)\right] \end{aligned} \tag{B.8}$$

The low frequency Q signal will be then proportional to the imaginary component of the RF signal:

$$V_{\mathrm{Q}} \propto \frac{1}{2} V_0^{\mathrm{LO}} V_0^{\mathrm{RF}} \sin(\phi_0) \tag{B.9}$$

Appendix C

Quality factor and bandwidth

The quality factor of a resonant circuit can be defined in two different ways. The first one is related to ratio between the energy stored inside the resonator and the energy dissipated for each cycle

$$Q = 2\pi \frac{\text{energy stored}}{\text{energy dissipated per cycle}} = \omega_0 \frac{\text{energy stored}}{\text{dissipating power}} \tag{C.1}$$

while the second definition expresses the quality factor as the ratio between the resonant frequency and the bandwidth of the circuit $\Delta\omega$

$$Q = \frac{\omega_0}{\Delta\omega} \tag{C.2}$$

where the bandwidth is taken where the power dissipated from the circuit is one half of the maximum value. It can be shown that the two definitions are equivalent. In this appendix the equivalence of the two definitions will be proved for a parallel RLC resonant circuit (fig. C.1).

Considering a parallel RLC circuit, the impedance seen by a current generator is

$$Z_{TOT} = \frac{j\omega L}{1 - \omega^2 LC + j\omega L/R} \tag{C.3}$$

Being the resonant frequency $\omega_0 = \sqrt{LC}$, at the resonance $1 - \omega^2 LC = 0$, so the only active component in the impedance is the resistive one. The combined action of the capacitor and inductor act as an open circuit.

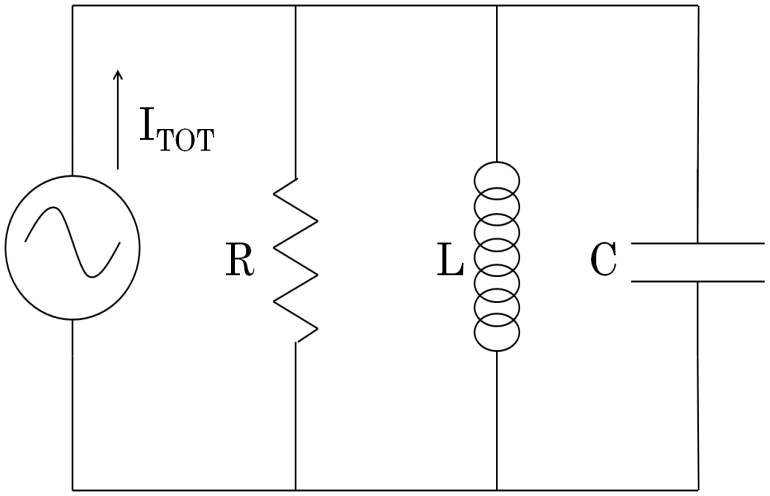

FIGURE C.1: RLC parallel circuit. In condition of resonance all the current flows through the resistor.

The current flowing in the resistance as a function of the frequency is

$$I_R = I_{TOT}\frac{Z_{TOT}}{Z_R} = I_{TOT}\frac{j\omega L}{R - \omega^2 RLC + j\omega L} \tag{C.4}$$

The transfer function is

$$|H(\omega)| \equiv \left|\frac{I_R}{I_{TOT}}\right| = \frac{\omega L}{\sqrt{(R - \omega^2 RLC)^2 + (\omega L)^2}} \tag{C.5}$$

The half power condition is achieved when $|H(\omega)| = 1/\sqrt{2}$ (fig. C.2):

$$\frac{1}{\sqrt{2}} = \frac{\omega L}{\sqrt{(R - \omega^2 RLC)^2 + (\omega L)^2}} \tag{C.6}$$

The previous equation leads to two solution for ω:

$$\omega_{1,2} = \mp\frac{1}{2RC} + \sqrt{(2RC)^{-2} + \omega_0^{-2}} \tag{C.7}$$

It is now possible to evaluate the bandwidth of the resonator:

$$\Delta\omega = \omega_2 - \omega_1 = \frac{1}{RC} \tag{C.8}$$

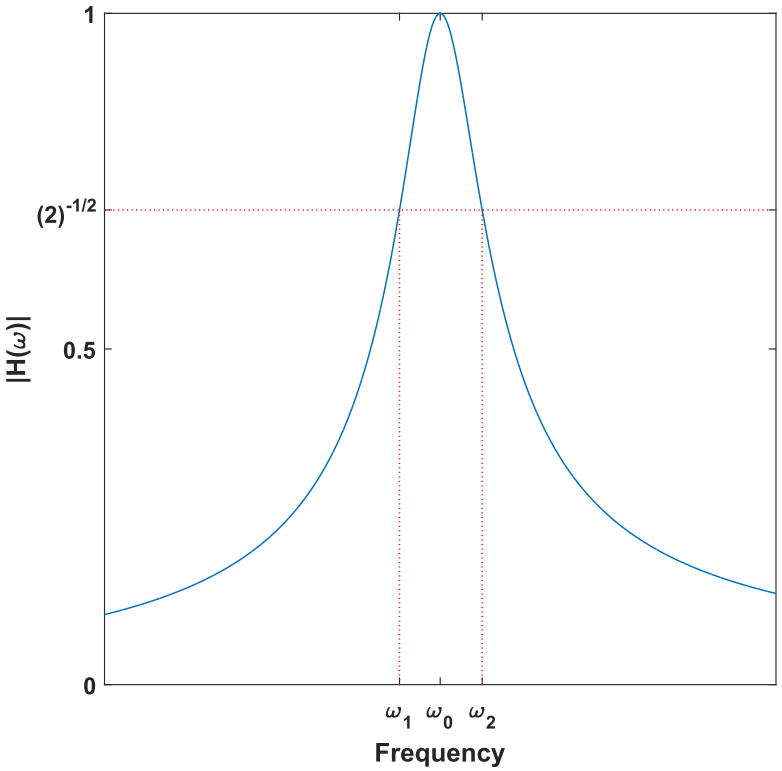

FIGURE C.2: RLC parallel circuit response function. The frequencies ω_1 and ω_2 correspond to the half power frequencies.

According to the eq. C.2, the quality factor is

$$Q = \frac{\omega_0}{\Delta\omega} = \frac{R}{\omega_0 L} \tag{C.9}$$

From the definition of eq. C.1, the quality factor is

$$Q = \omega_0 \frac{E_L + E_C}{RI^2} \tag{C.10}$$

where E_L and E_C are the energies stored in the inductor and in the capacitor, respectively. In the condition of resonance, $E_C = E_L$, so the quality factor becomes

$$Q = \omega_0 \frac{2E_C}{RI^2} = \omega_0 \frac{2 \cdot \frac{1}{2} C V_C^2}{R I_R^2} = \omega_0 \frac{C \cdot (R I_R)^2}{R I_R^2} = \omega_0 RC = \frac{R}{\omega_0 L} \tag{C.11}$$

It is then demonstrated that the results from both the definitions provide the same quality factor.

Bibliography

[1] S.L. Glashow. Partial Symmetries of Weak Interactions. *Nucl.Phys.*, 22:579–588, 1961. doi: 10.1016/0029-5582(61)90469-2. URL http://www.sciencedirect.com/science/article/pii/0029558261904692. pages 1

[2] Steven Weinberg. A Model of Leptons. *Phys.Rev.Lett.*, 19:1264–1266, 1967. doi: 10.1103/PhysRevLett.19.1264. URL http://journals.aps.org/prl/abstract/10.1103/PhysRevLett.19.1264. pages 1

[3] Abdus Salam. Weak and Electromagnetic Interactions. *Conf.Proc.*, C680519:367–377, 1968. pages 1

[4] ATLAS Collaboration. Observation of a new particle in the search for the Standard Model Higgs boson with the ATLAS detector at the LHC. *Phys.Lett.*, B716:1–29, 2012. doi: 10.1016/j.physletb.2012.08.020. URL http://www.sciencedirect.com/science/article/pii/S037026931200857X. pages 1

[5] CMS collaboration. Evidence for the direct decay of the 125 GeV Higgs boson to fermions. *Nature Phys.*, 10:557–560, 2014. doi: 10.1038/nphys3005. URL http://www.nature.com/nphys/journal/v10/n8/full/nphys3005.html. pages 1

[6] E. Fermi. *Zeitschrift fur Physik A Hadrons and Nuclei*, 88:161, 1935. pages 2

[7] C.L. Cowan, F. Reines, F.B. Harrison, H.W. Kruse, and A.D. McGuire. Detection of the free neutrino: A Confirmation. *Science*, 124:103–104, 1956. doi: 10.1126/science.124.3212.103. URL http://www.sciencemag.org/content/124/3212/103. pages 2

[8] Frederick Reines and Clyde L. Cowan. The neutrino. *Nature*, 178:446–449, 1956. doi: 10.1038/178446a0. URL http://www.nature.com/nature/journal/v178/n4531/abs/178446a0.html. pages 2

[9] Kai Zuber. *Neutrino Physics, Second Edition (Series in High Energy Physics, Cosmology and Gravitation)*. CRC Press, 2011. ISBN 1420064711. pages 2

[10] Ling-Lie Chau and Wai-Yee Keung. Comments on the Parametrization of the Kobayashi-Maskawa Matrix. *Phys.Rev.Lett.*, 53:1802–1805, 1984. doi: 10.1103/PhysRevLett.53.1802. URL http://journals.aps.org/prl/abstract/10.1103/PhysRevLett.53.1802. pages 3

[11] F. Capozzi, G.L. Fogli, E. Lisi, A. Marrone, D. Montanino, et al. Status of three-neutrino oscillation parameters, circa 2013. *Phys.Rev.*, D89(9):093018, 2014. doi: 10.1103/PhysRevD.89.093018. URL http://journals.aps.org/prd/abstract/10.1103/PhysRevD.89.093018. pages 4

[12] Yu-Feng Li, Jun Cao, Yifang Wang, and Liang Zhan. Unambiguous Determination of the Neutrino Mass Hierarchy Using Reactor Neutrinos. *Phys.Rev.*, D88:013008, 2013. doi: 10.1103/PhysRevD.88.013008. URL http://journals.aps.org/prd/abstract/10.1103/PhysRevD.88.013008. pages 5

[13] Soo-Bong Kim. Status and Prospects of Reactor Neutrino Experiments. 2015. pages 5

[14] G. Hinshaw et al. Nine-Year Wilkinson Microwave Anisotropy Probe (WMAP) Observations: Cosmological Parameter Results. *Astrophys.J.Suppl.*, 208:19, 2013. doi: 10.1088/0067-0049/208/2/19. URL http://iopscience.iop.org/0067-0049/208/2/19/. pages 7

[15] P.A.R. Ade et al. Planck 2015 results. XIII. Cosmological parameters. 2015. URL http://arxiv.org/abs/1502.01589. pages 7

[16] M. Goeppert-Mayer. Double beta-disintegration. *Phys.Rev.*, 48:512–516, 1935. doi: 10.1103/PhysRev.48.512. URL http://journals.aps.org/pr/abstract/10.1103/PhysRev.48.512. pages 7

[17] S.R. Elliott, A.A. Hahn, and M.K. Moe. Direct Evidence for Two Neutrino Double Beta Decay in ^{82}Se. *Phys.Rev.Lett.*, 59:2020–2023, 1987. doi:

10.1103/PhysRevLett.59.2020. URL http://journals.aps.org/prl/abstract/10.1103/PhysRevLett.59.2020. pages 7

[18] Yu.G. Zdesenko, Fedor A. Danevich, and V.I. Tretyak. Has neutrinoless double beta decay of Ge-76 been really observed? *Phys.Lett.*, B546:206–215, 2002. doi: 10.1016/S0370-2693(02)02705-3. URL http://www.sciencedirect.com/science/article/pii/S0370269302027053. pages 7

[19] H. Ejiri. Double beta decays and neutrino masses. *J.Phys.Conf.Ser.*, 49:104–109, 2006. doi: 10.1088/1742-6596/49/1/023. URL http://iopscience.iop.org/1742-6596/49/1/023/. pages 7

[20] Carla Macolino. Results on neutrinoless double beta decay from GERDA Phase I. *Mod.Phys.Lett.*, A29(1):1430001, 2014. doi: 10.1142/S0217732314300018. URL http://journals.aps.org/prl/abstract/10.1103/PhysRevLett.111.122503. pages 8, 9

[21] III Avignone, Frank T., Steven R. Elliott, and Jonathan Engel. Double Beta Decay, Majorana Neutrinos, and Neutrino Mass. *Rev.Mod.Phys.*, 80:481–516, 2008. doi: 10.1103/RevModPhys.80.481. URL http://journals.aps.org/rmp/abstract/10.1103/RevModPhys.80.481. pages 8

[22] Fedor Simkovic, Amand Faessler, Vadim Rodin, Petr Vogel, and Jonathan Engel. Anatomy of nuclear matrix elements for neutrinoless double-beta decay. *Phys.Rev.*, C77:045503, 2008. doi: 10.1103/PhysRevC.77.045503. URL http://journals.aps.org/prc/abstract/10.1103/PhysRevC.77.045503. pages

[23] Osvaldo Civitarese and Jouni Suhonen. Nuclear matrix elements for double beta decay in the QRPA approach: A critical review. *J.Phys.Conf.Ser.*, 173:012012, 2009. doi: 10.1088/1742-6596/173/1/012012. URL http://iopscience.iop.org/1742-6596/173/1/012012/. pages

[24] J. Menendez, A. Poves, E. Caurier, and F. Nowacki. Disassembling the Nuclear Matrix Elements of the Neutrinoless beta beta Decay. *Nucl.Phys.*, A818:139–151, 2009. doi: 10.1016/j.nuclphysa.2008.12.005. URL http://www.sciencedirect.com/science/article/pii/S0375947408008233. pages

[25] J. Barea and F. Iachello. Neutrinoless double-beta decay in the microscopic interacting boson model. *Phys.Rev.*, C79:044301, 2009. doi: 10.1103/PhysRevC.

79.044301. URL http://journals.aps.org/prc/abstract/10.1103/PhysRevC.79.044301. pages 8

[26] Stefano Dell'Oro, Simone Marcocci, and Francesco Vissani. New expectations and uncertainties on neutrinoless double beta decay. *Phys.Rev.*, D90(3):033005, 2014. doi: 10.1103/PhysRevD.90.033005. URL http://journals.aps.org/prd/abstract/10.1103/PhysRevD.90.033005. pages 9

[27] H.V. Klapdor-Kleingrothaus, A. Dietz, L. Baudis, G. Heusser, I.V. Krivosheina, et al. Latest results from the Heidelberg-Moscow double beta decay experiment. *Eur.Phys.J.*, A12:147–154, 2001. doi: 10.1007/s100500170022. URL http://link.springer.com/article/10.1007%2Fs100500170022. pages 9

[28] C.E. Aalseth et al. The IGEX Ge-76 neutrinoless double beta decay experiment: Prospects for next generation experiments. *Phys.Rev.*, D65:092007, 2002. doi: 10.1103/PhysRevD.65.092007. URL http://journals.aps.org/prd/abstract/10.1103/PhysRevD.65.092007. pages 9

[29] A.S. Barabash and V.B. Brudanin. Investigation of double beta decay with the NEMO-3 detector. *Phys.Atom.Nucl.*, 74:312–317, 2011. doi: 10.1134/S1063778811020062. URL http://link.springer.com/article/10.1134%2FS1063778811020062. pages 9

[30] R. Arnold et al. Search for neutrinoless double-beta decay of ^{100}Mo with the NEMO-3 detector. *Phys.Rev.*, D89(11):111101, 2014. doi: 10.1103/PhysRevD.89.111101. URL http://journals.aps.org/prd/abstract/10.1103/PhysRevD.89.111101. pages 9

[31] K. Alfonso et al. Search for Neutrinoless Double-Beta Decay of ^{130}Te with CUORE-0. 2015. pages 9

[32] K. Asakura et al. Results from KamLAND-Zen. 2014. pages 9

[33] J.B. Albert et al. Search for Majorana neutrinos with the first two years of EXO-200 data. *Nature*, 510:229–234, 2014. doi: 10.1038/nature13432. URL http://www.nature.com/nature/journal/v510/n7504/full/nature13432.html. pages 9

[34] R. Bernabei, P. Belli, F. Cappella, R. Cerulli, F. Montecchia, et al. Investigation of beta beta decay modes in Xe-134 and Xe-136. *Phys.Lett.*, B546:23–28, 2002. doi: 10.1016/S0370-2693(02)02671-0. URL http://www.sciencedirect.com/science/article/pii/S0370269302026710. pages 9

[35] M. Sisti, C. Arnaboldi, C. Brofferio, G. Ceruti, O. Cremonesi, et al. New limits from the Milano neutrino mass experiment with thermal microcalorimeters. *Nucl.Instrum.Meth.*, A520:125–131, 2004. doi: 10.1016/j.nima.2003.11.273. URL http://www.sciencedirect.com/science/article/pii/S0168900203031814. pages 10, 15

[36] V.M. Lobashev, V.N. Aseev, A.I. Belesev, A.I. Berlev, E.V. Geraskin, et al. Direct search for neutrino mass and anomaly in the tritium beta-spectrum: Status of 'Troitsk neutrino mass' experiment. *Nucl.Phys.Proc.Suppl.*, 91:280–286, 2001. doi: 10.1016/S0920-5632(00)00952-X. URL http://www.sciencedirect.com/science/article/pii/S092056320000952X. pages 10, 16

[37] Ch. Kraus, B. Bornschein, L. Bornschein, J. Bonn, B. Flatt, et al. Final results from phase II of the Mainz neutrino mass search in tritium beta decay. *Eur.Phys.J.*, C40:447–468, 2005. doi: 10.1140/epjc/s2005-02139-7. URL http://link.springer.com/article/10.1140%2Fepjc%2Fs2005-02139-7. pages 10, 16

[38] Alessandro Strumia and Francesco Vissani. Neutrino masses and mixings and... 2006. URL http://arxiv.org/abs/hep-ph/0606054. pages 11

[39] C.M. Cattadori, M. De Deo, M. Laubenstein, L. Pandola, and V.I. Tretyak. Observation of beta decay of In-115 to the first excited level of Sn-115. *Nucl.Phys.*, A748:333–347, 2005. doi: 10.1016/j.nuclphysa.2004.10.025. URL http://www.sciencedirect.com/science/article/pii/S0375947404011509. pages 15

[40] A. Picard, H. Backe, H. Barth, J. Bonn, B. Degen, Th. Edling, R. Haid, A. Hermanni, P. Leiderer, Th. Loeken, A. Molz, R.B. Moore, A. Osipowicz, E.W. Otten, M. Przyrembel, M. Schrader, M. Steininger, and Ch. Weinheimer. A solenoid retarding spectrometer with high resolution and transmission for keV electrons. *Nucl.Instrum.Meth.*, B63:345–358, 1992. doi: 10.

1016/0168-583X(92)95119-C. URL http://www.sciencedirect.com/science/article/pii/0168583X9295119C. pages 16

[41] A. Osipowicz et al. KATRIN: A Next generation tritium beta decay experiment with sub-eV sensitivity for the electron neutrino mass. Letter of intent. 2001. URL http://arxiv.org/abs/hep-ex/0109033. pages 16

[42] J.A. Formaggio. Project 8: Using Radio-Frequency Techniques to Measure Neutrino Mass. *Nucl.Phys.Proc.Supl.*, 229-232:371–375, 2012. doi: 10.1016/j.nuclphysbps.2012.09.058. URL http://www.sciencedirect.com/science/article/pii/S0920563212002757. pages 16

[43] D. M. Asner et al. Single electron detection and spectroscopy via relativistic cyclotron radiation. *Phys.Rev.Lett.*, 114(16):162501, 2015. doi: 10.1103/PhysRevLett.114.162501. URL http://journals.aps.org/prl/abstract/10.1103/PhysRevLett.114.162501. pages 17

[44] C.W. Reich and Balraj Singh. Nuclear Data Sheets for A = 163. *Nucl.Data Sheets*, 111:1211–1469, 2010. doi: 10.1016/j.nds.2010.04.001. URL http://www.sciencedirect.com/science/article/pii/S0090375210000451. pages 18

[45] G. Audi and A.H. Wapstra. The 1995 update to the atomic mass evaluation. *Nucl.Phys.*, A595:409–480, 1995. doi: 10.1016/0375-9474(95)00445-9. URL http://www.sciencedirect.com/science/article/pii/0375947495004459. pages 18

[46] C.L. Bennet, A.L. Hallin, R.A. Naumann, P.T. Springer, and M.S. Witherell. The X-ray spectrum following ^{163}Ho M electron capture. *Phys.Lett.*, B107:19–22, 1981. doi: 10.1016/0370-2693(81)91137-0. URL http://www.sciencedirect.com/science/article/pii/0370269381911370. pages 19

[47] A. De Rujula. A NEW WAY TO MEASURE NEUTRINO MASSES. *Nucl.Phys.*, B188:414, 1981. doi: 10.1016/0550-3213(81)90002-X. URL http://www.sciencedirect.com/science/article/pii/055032138190002X. pages 19

[48] A. De Rujula and Maurizio Lusignoli. Calorimetric Measurements of ^{163}Ho Decay as Tools to Determine the Electron Neutrino Mass. *Phys.Lett.*, B118:429, 1982. doi: 10.1016/0370-2693(82)90218-0. URL http://www.sciencedirect.com/science/article/pii/0370269382902180. pages 19

[49] W. Bambynek, H. Behrens, M.H. Chen, B. Crasemann, M.L. Fitzpatrick, et al. Orbital electron capture by the nucleus. *Rev.Mod.Phys.*, 49:77–221, 1977. doi: 10.1103/RevModPhys.49.77. URL http://journals.aps.org/rmp/abstract/10.1103/RevModPhys.49.77. pages 19

[50] P.T. Springer, C.L. Bennett, and P.A. Baisden. Measurement of the Neutrino Mass Using the Inner Bremsstrahlung Emitted in the Electron-Capture Decay og 163Ho. *Phys.Rev.*, A35:679–689, 1987. doi: 10.1103/PhysRevA.35.679. URL http://journals.aps.org/pra/abstract/10.1103/PhysRevA.35.679. pages 19

[51] Flavio Gatti, Massimiliano Galeazzi, Maurizio Lusignoli, Angelo Nucciotti, and Stefano Ragazzi. The Electron Capture Decay of 163-Ho to Measure the Electron Neutrino Mass with sub-eV Accuracy and Beyond. 2012. URL http://arxiv.org/abs/1202.4763. pages 21

[52] Frank J. Low. Low-Temperature Germanium Bolometer. *Journal of the Optical Society of America*, 51:1300–1304, 1961. doi: 10.1364/JOSA.51.001300. URL http://www.opticsinfobase.org/josa/abstract.cfm?uri=josa-51-11-1300. pages 23

[53] E. Fiorini and T.O. Niinikoski. Low Temperature Calorimetry for Rare Decays. *Nucl.Instrum.Meth.*, A224:83, 1984. doi: 10.1016/0167-5087(84)90449-6. URL http://www.sciencedirect.com/science/article/pii/0167508784904496. pages 23

[54] A. Alessandrello, J. W. Beeman, C. Brofferio, O. Cremonesi, E. Fiorini, A. Giuliani, E. E. Haller, A. Monfardini, A. Nucciotti, M. Pavan, G. Pessina, E. Previtali, and L. Zanotti. High Energy Resolution Bolometers for Nuclear Physics and X-Ray Spectroscopy. *Phys.Rev.Lett.*, 82:513, 1999. doi: 10.1103/PhysRevLett.82.513. URL http://journals.aps.org/prl/abstract/10.1103/PhysRevLett.82.513. pages 23

[55] Patrick Agnese, C. Cigna, Jean-Louis Pornin, R. Accomo, Claude Bonnin, N. Colombel, M. Delcourt, Eric Doumayrou, Jean Lepennec, Jerome Martignac, Vincent Reveret, Louis Rodriguez, and Laurent G. Vigroux. Filled Bolometer Arrays for Herschel/PACS. *Proc.SPIE Int.Soc.Opt.Eng.*, 4855:108, 2003.

doi: 10.1117/12.459191. URL http://proceedings.spiedigitallibrary.org/proceeding.aspx?articleid=1315207. pages 24

[56] K. D. Irwin. An application of electrothermal feedback for high resolution cryogenic particle detection. *Appl.Phys.Lett.*, 66:1998, 1995. doi: 10.1063/1.113674. URL http://scitation.aip.org/content/aip/journal/apl/66/15/10.1063/1.113674. pages 24

[57] Piet A. J. de Korte, Joern Beyer, Steve Deiker, Gene C. Hilton, Kent D. Irwin, Mike MacIntosh, Sae Woo Nam, Carl D. Reintsema, Leila R. Vale, and Martin E. Huber. Time-division superconducting quantum interference device multiplexer for transition-edge sensors. *Rev.Sci.Instrum.*, 74:3807, 2003. doi: 10.1063/1.1593809. URL http://scitation.aip.org/content/aip/journal/rsi/74/8/10.1063/1.1593809. pages 24

[58] T. M. Lanting, Hsiao-Mei Cho, John Clarke, W. L. Holzapfel, Adrian T. Lee, M. Lueker, P. L. Richards, Matt A. Dobbs, Helmuth Spieler, and A. Smith. Frequency-domain multiplexed readout of transition-edge sensor arrays with a superconducting quantum interference device. *Appl.Phys.Lett.*, 86:112511, 2005. doi: 10.1063/1.1884746. URL http://scitation.aip.org/content/aip/journal/apl/86/11/10.1063/1.1884746. pages 24

[59] K. D. Irwin, M. D. Niemack, J. Beyer, H. M. Cho, W. B. Doriese, G. C. Hilton, C. D. Reintsema, D. R. Schmidt, J N. Ullom, and L. R. Vale. Code-division multiplexing of superconducting transition-edge sensor arrays. *Supercond.Sci.Technol.*, 23:034004, 2010. doi: 10.1088/0953-2048/23/3/034004. URL http://iopscience.iop.org/0953-2048/23/3/034004/. pages 24

[60] K. D. Irwin and K. W. Lehnert. Microwave SQUID multiplexer . *Appl.Phys.Lett.*, 85:2107, 2004. doi: 10.1063/1.1791733. URL http://scitation.aip.org/content/aip/journal/apl/85/11/10.1063/1.1791733. pages 24

[61] J. A. B. Mates, G. C. Hilton, K. D. Irwin, L. R. Vale, and K. W. Lehnert. Demonstration of a multiplexer of dissipationless superconducting quantum interference devices. *Appl.Phys.Lett.*, 92:023514, 2008. doi: 10.1063/1.2803852. URL http://scitation.aip.org/content/aip/journal/apl/92/2/10.1063/1.2803852. pages 24

[62] B. Alpert, M. Balata, D. Bennett, M. Biasotti, C. Boragno, et al. HOLMES - The Electron Capture Decay of 163Ho to Measure the Electron Neutrino Mass with sub-eV sensitivity. 2014. doi: 10.1140/epjc/s10052-015-3329-5. URL http://link.springer.com/article/10.1140%2Fepjc%2Fs10052-015-3329-5. pages 24

[63] H. K. Onnes. The resistance of pure mercury at helium temperatures. *Commun. Phys. Lab. Univ. Leiden*, 12:120, 1911. pages 25

[64] W. Meissner and Ochsenfeld R. Ein neuer Effekt bei Eintritt der Supraleitfähigkeit. *Naturwissenschaften*, 21:787–788, 1933. doi: 10.1007/BF01504252. URL http://link.springer.com/article/10.1007%2FBF01504252. pages 25

[65] Leon N. Cooper. Bound electron pairs in a degenerate Fermi gas. *Phys.Rev.*, 104: 1189–1190, 1956. doi: 10.1103/PhysRev.104.1189. URL http://inspirehep.net/record/45266/export/hx. pages 26

[66] John Bardeen, L.N. Cooper, and J.R. Schrieffer. Microscopic theory of superconductivity. *Phys.Rev.*, 106:162, 1957. doi: 10.1103/PhysRev.106.162. URL http://journals.aps.org/pr/abstract/10.1103/PhysRev.106.162. pages 26

[67] Victor Moshchalkov, Mariela Menghini, T. Nishio, Q. H. Chen, A. V. Silhanek, V. H. Dao, L. F. Chibotaru, N. D. Zhigadlo, and J. Karpinski. Type-1.5 Superconductivity. *Phys.Rev.Lett.*, 102:117001, 2009. doi: 10.1103/PhysRevLett.102.117001. URL http://journals.aps.org/prl/abstract/10.1103/PhysRevLett.102.117001. pages 26

[68] N.W. Ashcroft and N.D. Mermin. *Solid State Physics*. Saunders College, Philadelphia, 1976. ISBN 0030839939. pages 26

[69] F. London and H. London. The Electromagnetic Equations of the Supraconductor. *Proc.Roy.Soc.*, A471:71, 1935. doi: 10.1098/rspa.1935.0048. URL http://rspa.royalsocietypublishing.org/content/149/866/71. pages 27

[70] F. London. *Superfluids. Vol.1, Macroscopic Theory of Superconductivity*. Wiley, New York, 1950. pages 27

[71] C.J. Gorter and H. Casimir. On supraconductivity I. *Physica*, 1:306, 1934. doi: 10.1016/S0031-8914(34)90037-9. URL http://www.sciencedirect.com/science/article/pii/S0031891434900379. pages 30

[72] Simon Doyle. *Lumped Element Kinetic Inductance Detectors*. PhD thesis, Cardiff University, April 2008. pages 31

[73] D. C. Mattis and J. Bardeen. Theory of the Anomalous Skin Effect in Normal and Superconducting Metals. *Phys.Rev.Lett.*, 111:412, 1958. doi: 10.1103/PhysRev.111.412. URL http://journals.aps.org/pr/abstract/10.1103/PhysRev.111.412. pages 32

[74] Jonas Zmuidzinas. Superconducting Microresonators: Physics and Applications. *Ann.Rev.Condensed Matter Phys.*, 3:169–214, 2012. doi: 10.1146/annurev-conmatphys-020911-125022. URL http://www.annualreviews.org/doi/abs/10.1146/annurev-conmatphys-020911-125022. pages 32, 41, 44

[75] Peter K. Day, Henry G. LeDuc, Benjamin A. Mazin, Anastasios Vayonakis, and Jonas Zmuidzinas. A broadband superconducting detector suitable for use in large arrays. *Nature*, 425:817, 2003. doi: 10.1038/nature02037. URL http://www.nature.com/nature/journal/v425/n6960/abs/nature02037.html. pages 34, 44, 64

[76] David M. Pozar. *Microwave Engineering, 4th Edition*. Wiley, 2011. ISBN 978-0-470-63155-3. pages 35

[77] Stephan Friedrich. *Superconducting Single Photon Imaging X-ray Spectrometers*. PhD thesis, Yale University, December 1997. pages 42

[78] S.B. Kaplan, C.C. Chi, D.N. Langenberg, J.J. Chang, S. Jafarey, et al. Quasiparticle and phonon lifetimes in superconductors. *Phys.Rev.*, B14:4854–4873, 1976. doi: 10.1103/PhysRevB.14.4854. URL http://journals.aps.org/prb/abstract/10.1103/PhysRevB.14.4854. pages 42, 89

[79] Quasiparticle number fluctuations in superconductors. Wilson, C. M. and Prober, D. E. *Phys.Rev.*, B69:094524, 2004. doi: 10.1103/PhysRevB.69.094524. URL http://journals.aps.org/prb/abstract/10.1103/PhysRevB.69.094524. pages 43

[80] Jiansong Gao, Jonas Zmuidzinas, Benjamin A. Mazin, Henry G. LeDuc, and Peter K. Day. Noise properties of superconducting coplanar waveguide microwave resonators. *Appl.Phys.Lett.*, 90:102507, 2007. doi: 10.1063/1.2711770. URL http://scitation.aip.org/content/aip/journal/apl/90/10/10.1063/1.2711770. pages 44

[81] J. Burnett, L. Faoro, I. Wisby, V. L. Gurtovoi, A. V. Chernykh, G. M. Mikhailov, V. A. Tulin, R. Shaikhaidarov, V. Antonov, P. J. Meeson, A. Ya. Tzalenchuk, and T. Lindstrom. Evidence for interacting two-level systems from the 1/f noise of a superconducting resonator. *Nature Commun.*, 5:4119, 2014. doi: 10.1038/ncomms5119. URL http://www.nature.com/ncomms/2014/140617/ncomms5119/full/ncomms5119.html. pages

[82] Jiansong Gao, Miguel Daal, John M. Martinis, Anastasios Vayonakis, Jonas Zmuidzinas, Bernard Sadoulet, Benjamin A. Mazin, Peter K. Day, and Henry G. Leduc. A semiempirical model for two-level system noise in superconducting microresonators. *Appl.Phys.Lett.*, 92:212504, 2008. doi: 10.1063/1.2937855. URL http://scitation.aip.org/content/aip/journal/apl/92/21/10.1063/1.2937855. pages 44

[83] Jiansong Gao, Miguel Daal, Anastasios Vayonakis, Shwetank Kumar, Jonas Zmuidzinas, Bernard Sadoulet, Benjamin A. Mazin, Peter K. Day, and Henry G. Leduc. Experimental evidence for a surface distribution of two-level systems in superconducting lithographed microwave resonators. *Appl.Phys.Lett.*, 92:152505, 2008. doi: 10.1063/1.2906373. URL http://scitation.aip.org/content/aip/journal/apl/92/15/10.1063/1.2906373. pages 44

[84] Omid Noroozian, Jiansong Gao, Jonas Zmuidzinas, Henry G. LeDuc, and Benjamin A. Mazin. Two-level system noise reduction for Microwave Kinetic Inductance Detectors. *AIP Conf.Proc.*, 1185:148–151, 2009. doi: 10.1063/1.3292302. URL http://scitation.aip.org/content/aip/proceeding/aipcp/10.1063/1.3292302. pages 44, 57

[85] A. B. Pippard. Field Variation of the Superconducting Penetration Depth. *Proc.Roy.Soc.*, A203:210, 1950. doi: 10.1098/rspa.1950.0135. URL http://rspa.royalsocietypublishing.org/content/203/1073/210. pages 45

[86] A. B. Pippard. An Experimental and Theoretical Study of the Relation between Magnetic Field and Current in a Superconductor. *Proc.Roy.Soc.*, 216:547, 1953. doi: 10.1098/rspa.1953.0040. URL http://rspa.royalsocietypublishing.org/content/216/1127/547. pages 45

[87] P. J. de Visser, S. Withington, and D. J. Goldie. Readout-power heating and hysteretic switching between thermal quasiparticle states in kinetic inductance detectors. *J.App.Phys.*, 108:114504, 2010. doi: 10.1063/1.3517152. URL http://scitation.aip.org/content/aip/journal/jap/108/11/10.1063/1.3517152. pages 45

[88] T. Dahm and D. J. Scalapino. Theory of intermodulation in a superconducting microstrip resonator. *J.App.Phys.*, 81:2002, 1997. doi: 10.1063/1.364056. URL http://scitation.aip.org/content/aip/journal/jap/81/4/10.1063/1.364056. pages 45

[89] L.J. Swenson, P.K. Day, B.H. Eom, H.G. Leduc, N. Llombart, et al. Operation of a titanium nitride superconducting microresonator detector in the nonlinear regime. *J.Appl.Phys.*, 113:104501, 2013. doi: 10.1063/1.4794808. URL http://scitation.aip.org/content/aip/journal/jap/113/10/10.1063/1.4794808. pages 46, 47

[90] M. A. Golosovsky, H. J. Snortland, and M. R. Beasley. Nonlinear microwave properties of superconducting Nb microstrip resonators. *Phys.Rev.*, 51:6462, 1995. doi: 10.1103/PhysRevB.51.6462. URL http://journals.aps.org/prb/abstract/10.1103/PhysRevB.51.6462. pages 47

[91] P. J. de Visser, S. Withington, and D. J. Goldie. Readout-power heating and hysteretic switching between thermal quasiparticle states in kinetic inductance detectors. *J.App.Phys.*, 108:114504, 2010. doi: 10.1063/1.3517152. URL http://scitation.aip.org/content/aip/journal/jap/108/11/10.1063/1.3517152. pages 47

[92] James A. Schlaerth. *Microwave Kinetic Inductance Detector Camera Development for Millimeter-Wave Astrophysics*. PhD thesis, University of Colorado, 2010. pages 49

[93] M. Faverzani, P. Day, A. Nucciotti, and E. Ferri. Developments of Microresonators Detectors for Neutrino Physics in Milan. *J.Low Temp.Phys.*, 167:1041–1047, 2012. doi: 10.1007/s10909-012-0538-2. URL http://link.springer.com/article/10.1007/s10909-012-0538-2. pages 52

[94] Henry G. Leduc, Bruce Bumble, Peter K. Day, Anthony D. Turner, Byeong Ho Eom, et al. Titanium Nitride Films for Ultrasensitive Microresonator Detectors. *Appl.Phys.Lett.*, 97:102509, 2010. doi: 10.1063/1.3480420. URL http://scitation.aip.org/content/aip/journal/apl/97/10/10.1063/1.3480420. pages 52, 53, 54

[95] J. Gao, M. R. Vissers, M. Sandberg, D. Li, H. M. Cho, C. Bockstiegel, B. A. Mazin, H. G. Leduc, S. Chaudhuri, D. P. Pappas, and K. D. Irwin. Properties of TiN for Detector and Amplifier Applications. *J.Low Temp.Phys.*, 176:136–141, 2014. doi: 10.1007/s10909-014-1089-5. URL http://link.springer.com/article/10.1007%2Fs10909-014-1089-5. pages 53

[96] J. Gao, M.R. Visser, M.O. Sandberg, F.C.S. da Silva, S.W. Nam, et al. A titanium-nitride near-infrared kinetic inductance photon-counting detector and its anomalous electrodynamics. *Appl.Phys.Lett.*, 101:142602, 2012. doi: 10.1063/1.4756916. URL http://scitation.aip.org/content/aip/journal/apl/101/14/10.1063/1.4756916. pages 55

[97] P. Diener, H.G. Leduc, S.J.C. Yates, Y.J.Y. Lankwarden, and J.J.A. Baselmans. Design and Testing of Kinetic Inductance Detectors Made of Titanium Nitride. *J.Low Temp.Phys.*, 167:305, 2013. doi: 10.1007/s10909-012-0484-z. URL http://link.springer.com/article/10.1007%2Fs10909-012-0484-z. pages 55

[98] William Silvert. Theory of the superconducting proximity effect. 1975. doi: 10.1007/BF00120864. URL http://link.springer.com/article/10.1007%2FBF00120864. pages 55

[99] Michael R. Vissers, Jiansong Gao, Martin Sandberg, Shannon M. Duff, David S. Wisbey, Kent D. Irwin, and David P. Pappas. Proximity-coupled Ti/TiN multilayers for use in kinetic inductance detectors. *Appl.Phys.Lett.*, 102:232603, 2013. doi: 10.1063/1.4804286. URL http://scitation.aip.org/content/aip/journal/apl/102/23/10.1063/1.4804286. pages 55, 56

[100] Leon N. Cooper. Superconductivity in the Neighborhood of Metallic Contacts. *Phys.Rev.Lett.*, 6:689, 1961. doi: 10.1103/PhysRevLett.6.689. URL http://journals.aps.org/prl/abstract/10.1103/PhysRevLett.6.689. pages 55

[101] Noboru Sato. Crystallographic structure and superconductive properties of Nb-Ti films with an artificially layered structure. *J.Appl.Phys.*, 67:7493, 1990. doi: 10.1063/1.345809. URL http://scitation.aip.org/content/aip/journal/jap/67/12/10.1063/1.345809. pages 55

[102] Arttu Luukanena, Heikki Sipilaa, Kimmo Kinnunenb, Antti Nuottajarvib, and Jukka Pekola. Transition-edge microcalorimeters for X-ray space applications. *Physica B*, 284-288:2133, 2000. doi: 10.1016/S0921-4526(99)03046-X. URL http://www.sciencedirect.com/science/article/pii/S092145269903046X. pages 55

[103] A. Giachero, P. Day, P. Falferi, M. Faverzani, E. Ferri, et al. Critical Temperature tuning of Ti/TiN multilayer films suitable for low temperature detectors. 2013. doi: 10.1007/s10909-013-1078-0. URL http://link.springer.com/article/10.1007%2Fs10909-013-1078-0. pages 55, 56

[104] N.E. Booth. QUASIPARTICLE TRAPPING AND THE QUASIPARTICLE MULTIPLIER. *Appl. Phys. Lett.*, 1986. URL http://scitation.aip.org/content/aip/journal/apl/50/5/10.1063/1.98229. pages 62

[105] Paul J. Petersan and Steven M. Anlage. Measurement of resonant frequency and quality factor of microwave resonators: Comparison of methods. *J.Appl.Phys.*, 84:3392, 1998. doi: 10.1063/1.368498. URL http://scitation.aip.org/content/aip/journal/jap/84/6/10.1063/1.368498. pages 70

[106] Jiansong Gao. *The physics of superconducting microwave resonators*. PhD thesis, California Institute of Technology, June 2008. pages 71

[107] Claudia Giordano. *MKID arrays: panoramic detectors for CMB experiments*. PhD thesis, Università degli Studi di Roma La Sapienza, October 2009. pages 71

[108] J. Gao, J. Zmuidzinas, B.A. Mazin, P.K. Day, and H.G. Leduc. Experimental study of the kinetic inductance fraction of superconducting coplanar waveguide. *Nucl.Instrum.Meth.*, A559:585–587, 2006. doi: 10.1016/j.

nima.2005.12.075. URL http://www.sciencedirect.com/science/article/pii/S0168900205025003. pages 72

[109] Michael Tinkham. *Introduction to Superconductivity: Second Edition.* Dover Books, 2004. ISBN 978-0486435039. pages 72

[110] M. S. Khalil, M. J. A. Stoutimore, F. C. Wellstood, and K. D. Osborn. An analysis method for asymmetric resonator transmission applied to superconducting devices. *J.App.Phys.*, 111:054510, 2012. doi: 10.1063/1.3692073. URL http://scitation.aip.org/content/aip/journal/jap/111/5/10.1063/1.3692073. pages 77

[111] P. Lerch and A. Zehnder. Quantum giaever detectors: Stj's. In Christian Enss, editor, *Cryogenic Particle Detection*, pages 217–266. Springer, 2005. doi: 10.1007/10933596_5. URL http://link.springer.com/chapter/10.1007/10933596_5. pages 88

[112] M.A. Scherschel, C.W. Hagen, A. Zehnder, S.P. Zhao, and H.R. Ott. Radiation induced hot spots in superconducting Sn strips. *Physica C*, 193:164, 1991. doi: 10.1016/0921-4534(92)90727-T. URL http://www.sciencedirect.com/science/article/pii/092145349290727T. pages 88

[113] Jhy-Jiun Chang and D. J. Scalapino. Kinetic-equation approach to nonequilibrium superconductivity. *Phys.Rev.*, B15:2651, 1977. doi: 10.1103/PhysRevB.15.2651. URL https://journals.aps.org/prb/abstract/10.1103/PhysRevB.15.2651. pages 89

[114] V. Narayanamurti, R. C. Dynes, P. Hu, H. Smith, and W. F. Brinkman. Quasiparticle and phonon propagation in bulk, superconducting lead. *Phys.Rev.*, B18: 6041, 1978. doi: 10.1103/PhysRevB.18.6041. URL http://journals.aps.org/prb/abstract/10.1103/PhysRevB.18.6041. pages 89

[115] S. Friedrich, K. Segall, M. C. Gaidis, C. M. Wilson, D. E. Prober, A. E. Szymkowiak, and S. H. Moseley. Experimental quasiparticle dynamics in a superconducting, imaging x-ray spectrometer. *Appl.Phys.Lett.*, 71:3901, 1997. doi: 10.1063/1.120538. URL http://scitation.aip.org/content/aip/journal/apl/71/26/10.1063/1.120538. pages 90

[116] M.L. van den Berg, F.B. Kiewlet, M.P. Bruijn, O.J. Luiten, P.A.J. de Korte, J. Martin, and R.P. Huebener. A Nb single crystal X-ray detector read

out by superconductive tunnel junctions. *IEEE Trans.Appl.Supercond.*, 9:2951–2954, 1999. doi: 10.1109/77.783649. URL http://ieeexplore.ieee.org/xpl/articleDetails.jsp?arnumber=783649. pages 90

[117] P. Hettl, G. Angloher, M. Bruckmayer, F.v. Feilitzsch, J. Jochum, H. Kraus, and R.L. Mossbauer. Progress in Fabrication and Development of Ta-Al/AlxOy/Al Superconducting Tunnel Junctions as Position and Energy Sensitive X-Ray Detectors. *Proceedings of LTD-7*, 1997. pages 90

[118] Benjamin A. Mazin. *Microwave Kinetic Inductance Detectors*. PhD thesis, California Institute of Technology, August 2004. pages 91